


44
AFRPL-TR-72-55



**CASE BOND STRESS CALCULATIONS
FOR FLAPPED CYLINDRICAL ANALOGS
OF SOLID PROPELLANT ROCKET MOTORS**

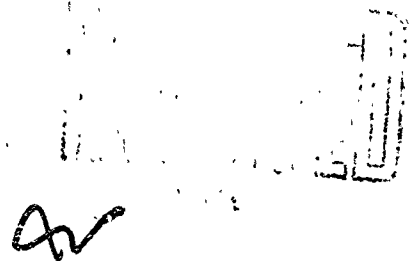
**BONDLINER PARAMETRIC STUDIES
TASK 1**

TECHNICAL (INTERIM) REPORT, AFRPL-TR-72-55

MAY 1972

**HERCULES INCORPORATED
SYSTEMS GROUP
Bacchus Works • Magna, Utah**

"Approved for public release;
distribution unlimited".



**AIR FORCE ROCKET PROPULSION LABORATORY
AIR FORCE SYSTEMS COMMAND
UNITED STATES AIR FORCE
EDWARDS, CALIFORNIA**

Reproduced by
**NATIONAL TECHNICAL
INFORMATION SERVICE**
U.S. Department of Commerce
Patent & A-22151

AD 744901

UNCLASSIFIED

Security Classification

DOCUMENT CONTROL DATA - P&D		
(Security classification of title, body of abstract and indexing annotation must be entered when the overall report is classified)		
1. ORIGINATING ACTIVITY (Corporate author)		2a. REPORT SECURITY CLASSIFICATION
Hercules Incorporated Bacchus Works, Magna, Utah		Unclassified
		2b. GROUP
3. REPORT TITLE		
Case Bond Stress Calculations for Flapped Cylindrical Analogs of Solid Propellant Rocket Motors		
4. DESCRIPTIVE NOTES (Type of report and inclusive dates)		
Bondline Parametric Studies		
5. AUTHOR(S) (Last name, first name, initial)		
Anderson, J. McKay		
6. REPORT DATE	7a. TOTAL NO. OF PAGES	7b. NO. OF REFS
May 1972	89	10
8a. CONTRACT OR GRANT NO.	9a. ORIGINATOR'S REPORT NUMBER(S)	
F04611-72-C-0009	AFRPL-TR-74-55	
b. PROJECT NO.	9b. OTHER REPORT NO(S) (Any other numbers that may be assigned this report)	
c.		
d.		
10. AVAILABILITY/LIMITATION NOTICES		
Approved for public release; distribution unlimited		
11. SUPPLEMENTARY NOTES		12. SPONSORING MILITARY ACTIVITY
		AFRPL, Edwards, California
13. ABSTRACT		
<p>Numerical stress solutions were obtained for finite-length cylinders bonded to a flexible case and subjected to thermal shrinkage, axial acceleration, and internal pressure loading. Finite-element models contained insulator, flap, case-bond liner, and propellant layers typical of solid propellant rocket motors. Grid structure in the region of the flap termination was highly refined to provide accurate estimates for the maximum case-bond stresses.</p> <p>The stress solutions indicated that the flap length, flap modulus and liner modulus do not significantly affect case-bond stresses. The most important parameter relative to maximum stresses is the thickness of material between the flap-insulator bondline and the liner-propellant bondline. Parametric studies were performed over a range of web-fractions and length-to-diameter ratios. These studies indicate that the stress distribution adjacent to the end termination is insensitive to the overall cylinder configuration, and sensitive only to the local end termination geometry. However, the maximum stresses at the end termination increase with web-fraction and length-to-diameter ratio for internal pressure and thermal shrinkage loading.</p>		

DD FORM 1473
1 JAN 64UNCLASSIFIED
Security Classification

I

Security Classification

1A	KEY WORDS	LINK A		LINK B		LINK C	
		ROLE	WT	ROLE	WT	ROLE	WT

INSTRUCTIONS

1. **ORIGINATING ACTIVITY:** Enter the name and address of the contractor, subcontractor, grantee, Department of Defense activity or other organization (*corporate author*) issuing the report.
- 2a. **REPORT SECURITY CLASSIFICATION:** Enter the overall security classification of the report. Indicate whether "Restricted Data" is included. Marking is to be in accordance with appropriate security regulations.
- 2b. **GROUP:** Automatic downgrading is specified in DoD Directive 5200.10 and Armed Forces Industrial Manual. Enter the group number. Also, when applicable, show that optional markings have been used for Group 3 and Group 4 as authorized.
3. **REPORT TITLE:** Enter the complete report title in all capital letters. Titles in all cases should be unclassified. If a meaningful title cannot be selected without classification, show title classification in all capitals in parenthesis immediately following the title.
4. **DESCRIPTIVE NOTES:** If appropriate, enter the type of report, e.g., interim, progress, summary, annual, or final. Give the inclusive dates when a specific reporting period is covered.
5. **AUTHOR(S):** Enter the name(s) of author(s) as shown on or in the report. Enter last name, first name, middle initial. If military, show rank and branch of service. The name of the principal author is an absolute minimum requirement.
6. **REPORT DATE:** Enter the date of the report as day, month, year, or month year. If more than one date appears on the report, use date of publication.
- 7a. **TOTAL NUMBER OF PAGES:** The total page count should follow normal pagination procedures, i.e., enter the number of pages containing information.
- 7b. **NUMBER OF REFERENCES:** Enter the total number of references cited in the report.
- 8a. **CONTRACT OR GRANT NUMBER:** If appropriate, enter the applicable number of the contract or grant under which the report was written.
- 8b, 8c, & 8d. **PROJECT NUMBER:** Enter the appropriate military department identification, such as project number, subproject number, system numbers, task number, etc.
- 9a. **ORIGINATOR'S REPORT NUMBER(S):** Enter the official report number by which the document will be identified and controlled by the originating activity. This number must be unique to this report.
- 9b. **OTHER REPORT NUMBER(S):** If the report has been assigned any other report numbers (*either by the originator or by the sponsor*), also enter this number(s).
10. **AVAILABILITY/LIMITATION NOTICES:** Enter any limitations on further dissemination of the report, other than those

imposed by security classification, using standard statements such as:

- (1) "Qualified requesters may obtain copies of this report from DDC."
- (2) "Foreign announcement and dissemination of this report by DDC is not authorized."
- (3) "U. S. Government agencies may obtain copies of this report directly from DDC. Other qualified DDC users shall request through _____."
- (4) "U. S. military agencies may obtain copies of this report directly from DDC. Other qualified users shall request through _____."
- (5) "All distribution of this report is controlled. Qualified DDC users shall request through _____"

If the report has been furnished to the Office of Technical Services, Department of Commerce, for sale to the public, indicate this fact and enter the price, if known.

11. SUPPLEMENTARY NOTES: Use for additional explanatory notes.

12. SPONSORING MILITARY ACTIVITY: Enter the name of the departmental project office or laboratory sponsoring (paying for) the research and development. Include address.

1.3. ABSTRACT: Enter an abstract giving a brief and factual summary of the document indicative of the report, even though it may also appear elsewhere in the body of the technical report. If additional space is required, a continuation sheet shall be attached.

It is highly desirable that the abstract of classified reports be unclassified. Each paragraph of the abstract shall end with an indication of the military security classification of the information in the paragraph, represented as (TS) (S) (C), or (U).

There is no limitation on the length of the abstract. However, the suggested length is from 150 to 225 words.

14. KEY WORDS: Key words are technically meaningful terms or short phrases that characterize a report and may be used as index entries for cataloging the report. Key words must be selected so that no security classification is required. Identifiers, such as equipment model designation, trade name, military product code name, geographic location, may be used as key words but will be followed by an indication of technical content. The assignment of links, rules, and weights is optional.

UNCLASSIFIED
Security Classification

CASE BOND STRESS CALCULATIONS
FOR FLAPPED CYLINDRICAL ANALOG
OF SOLID PROPELLANT ROCKET MOTORS

BONDLINE PARAMETRIC STUDIES

TASK I

TECHNICAL (INTERIM) REPORT, AFRPL-TR-72-55

May 1972

HERCULES INCORPORATED
SYSTEMS GROUP
Bacchus Works • Magna, Utah

"Approved for public release;
distribution unlimited".

AIR FORCE ROCKET PROPULSION LABORATORY
AIR FORCE SYSTEMS COMMAND
UNITED STATES AIR FORCE
EDWARDS, CALIFORNIA

TE

NOTICES

When U. S. Government drawings, specifications, or other data are used for any purpose other than a definitely related Government procurement operation, the Government thereby incurs no responsibility nor any obligation whatsoever, and the fact that the Government may have formulated, furnished, or in any way supplied the said drawings, specifications, or other data, is not to be regarded by implication or otherwise, or in any manner licensing the holder or any other person or corporation, or conveying any rights or permission to manufacture, use, or sell any patented invention that may in any way be related thereto.

FOREWORD

This report documents work performed under Task I of the Case-Liner-Bond Study, authorized by Contract F04611-72-C-0009. Task I involves the calculations of typical case-bond stress distributions in cylindrical motor analogs. The work was performed at Hercules Incorporated, Bacchus Works, Magna, Utah.

Preparation of this report is authorized under data item B003 of the data requirements list in the contract. Contract F04611-72-C-0009 was issued to Hercules by the Air Force Rocket Propulsion Laboratory, Director of Laboratories, Edwards, California, Air Force Systems Command, United States Air Force. The Air Force Project officer for this work is Mr. Norman D. Walker.

Publication of this report does not constitute Air Force approval of the reports findings or conclusions. It is published only for the exchange and stimulation of ideas.

Published by

The Publications Group
General Services Department
HERCULES INCORPORATED
Bacchus Works
Magna, Utah



ABSTRACT

Numerical stress solutions were obtained for finite-length cylinders bonded to a flexible case and subjected to thermal shrinkage, axial acceleration, and internal pressure loading. Finite-element models contained insulator, flap, case-bond liner, and propellant layers typical of solid propellant rocket motors. Grid structure in the region of the flap termination was highly refined to provide accurate estimates for the maximum case-bond stresses.

The stress solutions indicated that flap length, flap modulus, and liner modulus do not significantly affect the case-bond stresses. The most important parameter relative to the maximum stresses is the thickness of material between the flap-insulator bondline and the liner-propellant bondline. Parametric studies were performed over a range of web-fractions and length-to-diameter ratios. These studies indicate that the stress distribution adjacent to the end termination is insensitive to the overall cylinder configuration, and sensitive only to the local end termination geometry. However, the maximum stresses at the end termination increase with web-fraction and length-to-diameter ratio for internal pressure and thermal shrinkage loading.

An equivalence was established between the stress solutions for internal pressure loading and thermal shrinkage loading. This equivalence provided highly accurate estimates for internal pressure stresses using the results for restrained thermal shrinkage loading.

TABLE OF CONTENTS

<u>Section</u>		<u>Page</u>
	Foreword	
	Abstract	IV
	List of Figures	VII
	List of Tables	XIII
	Nomenclature	XIV
I	INTRODUCTION	1
II	MATHEMATICAL MODELING	3
III	RESULTS FOR THERMAL SHRINKAGE LOADING	6
	A. Material Property Effects	7
	B. Flap Length Effects	10
	C. Web Fraction and Length/Diameter (L/D) Studies	11
IV	THERMAL-PRESSURE LOADING EQUIVALENCE	15
V	LOAD SHARING OF CASE AND GRAIN	17
	A. Internal Pressure Loading	17
	B. Thermal Shrinkage Loading	19
VI	RESULTS FOR INTERNAL PRESSURE LOADING	21
	A. Direct Internal Pressure Loading Results . . .	21
	B. Case Hoop Expansion Component of Loading . . .	21
	C. Procedure for Predicting Pressure Solutions from Thermal Solutions	23
VII	RESULTS FOR AXIAL ACCELERATION LOADING	27
VIII	SUMMARY AND CONCLUSIONS	29
	References	30

LIST OF FIGURES

<u>Number</u>	<u>Title</u>	<u>Page</u>
1	Cylinder Model for Flap Termination Studies	31
2	Finite Element Model for Cylinder with L/D = 1.0 and W/b = 0.8	32
3	Finite Element Grid Detail Adjacent to Flap Termination	33
4	Case Bond Liner Stresses for a Cylinder with L/D = 1.0 and W/b = 0.8 Under Thermal Shrinkage Loading	34
5	Case Bond Liner Stresses Near the Flap Termination for a Cylinder with L/D = 1.0 and W/b = 0.8 Under Thermal Shrinkage Loading	35
6	Lines of Constant Maximum Principal Stress $\left(\frac{\sigma_{\max}}{E\delta}\right)$ in the Vicinity of the Flap Termination for a Cylinder with L/D = 1.0 and W/b = 0.8 Under Thermal Shrinkage Loading	36
7	Lines of Constant Maximum Principal Strain $\left(\frac{\epsilon_{\max}}{\delta}\right)$ in the Vicinity of the Flap Termination for a Cylinder with L/D = 1.0 and W/b = 0.8 Under Thermal Shrinkage Loading	37
8	Case Bond Liner Stresses Near the Flap Termination for a Cylinder with L/D = 1.0 and W/b = 0.8 ($E_{\text{flap}} =$ 200 psi) Under Thermal Shrinkage Loading	38
9	Case Bond Axial Stresses in the Liner Near the Flap Termination for a Cylinder with L/D = 1.0 and W/b = 0.8 Under Thermal Shrinkage Liner	39
10	Lines of Constant Maximum Principal Stress $\left(\frac{\sigma_{\max}}{E\delta}\right)$ in the Vicinity of the Flap Termination for a Cylinder with L/D = 1.0 and W/b = 0.8 ($E_{\text{flap}} = 200$ psi) Under Thermal Shrinkage Loading	40

LIST OF FIGURES (Cont)

<u>Number</u>	<u>Title</u>	<u>Page</u>
11	Lines of Constant Maximum Principal Strain $\left(\frac{\epsilon_{\max}}{\delta}\right)$ in the Vicinity of the Flap Termination for a Cylinder with $L/D = 1.0$ and $W/b = 0.8$ ($E_{\text{flap}} = 200$) Under Thermal Shrinkage Loading	41
12	Propellant Radial Stresses at the Propellant-to-Liner Bond Adjacent to the Flap Termination for a Cylinder with $L/D = 1.0$ and $W/b = 0.8$ Under Thermal Shrinkage Loading	42
13	Propellant Maximum Principal Stresses at the Propellant-to-Liner Bond Adjacent to the Flap Termination for a Cylinder with $L/D = 1.0$ and $W/b = 0.8$ Under Thermal Shrinkage Loading	43
14	Propellant Shear Stresses at the Propellant-to-Liner Bond Adjacent to the Flap Termination for a Cylinder with $L/D = 1.0$ and $W/b = 0.8$ Under Thermal Shrinkage Loading	44
15	Propellant Maximum Principal Strains at the Propellant-to-Liner Bond Adjacent to the Flap Termination for a Cylinder with $L/D = 1.0$ and $W/b = 0.8$ Under Thermal Shrinkage Loading	45
16	Lines of Constant Maximum Principal Stress $\left(\frac{\sigma_{\max}}{E\delta}\right)$ in the Vicinity of the Flap Termination for a Cylinder with $L/D = 1.0$ and $W/b = 0.8$ ($E_{\text{flap}} = 200$ psi, $E_{\text{liner}} = 100$ psi) Under Thermal Shrinkage Loading	46
17	Lines of Constant Maximum Principal Strain $\left(\frac{\epsilon_{\max}}{\delta}\right)$ in the Vicinity of the Flap Termination for a Cylinder with $L/D = 1.0$ and $W/b = 0.8$ ($E_{\text{flap}} = 200$ psi, $E_{\text{liner}} = 100$ psi) Under Thermal Shrinkage Loading	47
18	Lines of Constant Maximum Principal Stress $\left(\frac{\sigma_{\max}}{E\delta}\right)$ in the Vicinity of the Flap Termination for a Cylinder with $L/D = 1.0$ and $W/b = 0.8$ ($E_{\text{flap}} = E_{\text{insulator}} = E_{\text{liner}} = 200$ psi) Under Thermal Shrinkage Loading	48

LIST OF FIGURES (Cont)

<u>Number</u>	<u>Title</u>	<u>Page</u>
19	Lines of Constant Maximum Principal Strain $\left(\frac{\epsilon_{\max}}{\delta}\right)$ in the Vicinity of the Flap Termination for a Cylinder with $L/D = 1.0$ and $W/b = 0.8$ ($E_{\text{flap}} = E_{\text{insulator}} = E_{\text{liner}} = 200 \text{ psi}$) Under Thermal Shrinkage Loading . . .	49
20	Ratio of the Maximum Principal Stress in the Flap, Liner, and Propellant to that at the Flap-Liner Interface in the Vicinity of the Flap Termination for a Cylinder with $L/D = 1.0$ and $W/b = 0.8$ Under Thermal Shrinkage Loading	50
21	Radial Stress in the Case Bond Liner for a Cylinder with $L/D = 1.0$ and $W/b = 0.8$ and a Variable Flap Length Under Thermal Shrinkage Loading	51
22	Shear Stress in the Case Bond Liner for a Cylinder with $L/D = 1.0$ and $W/b = 0.8$ and a Variable Flap Length Under Thermal Shrinkage Loading	52
23	Maximum Principal Stress Adjacent to the Flap Termination for Flap Lengths of 0.1 and 0.5 In. Relative to that for a Flap Length of 1.0 In.	53
24	Strain Energy in Cylinder Under Thermal Shrinkage Loading, with $L/D = 1.0$ and $W/b = 0.8$, as a Function of Flap Length	54
25	Gradient in Maximum Principal Stress as a Function of Normalized Radial Distance from Flap-Insulator Bond Discontinuity for Cylinder with $L/D = 1.0$ and $W/b = 0.8$	55
26	Stress Gradient as a Function of Radial Distance from Flap-Insulator Bond Discontinuity	56
27	Peak Radial Stress Adjacent to Flap Termination for Cylinder Under Thermal Shrinkage Loading	57
28	Peak Maximum Principal Stress Adjacent to Flap Termination for Cylinder Under Thermal Shrinkage Loading	58
29	Peak Maximum Principal Strain in Propellant Adjacent to Flap Termination for Cylinder Under Thermal Shrinkage Loading	59

LIST OF FIGURES (Cont)

<u>Number</u>	<u>Title</u>	<u>Page</u>
30	Peak Center Port Hoop Stress for Cylinder Under Thermal Shrinkage Loading	60
31	Peak Center Port Hoop Strain for Cylinder Under Thermal Shrinkage Loading	61
32	Ratio of Peak Maximum Principal Propellant Stress Near Flap Termination to Maximum Center Port Hoop Stress for Cylinder Under Thermal Shrinkage Loading . .	62
33	Case Bond Liner Stress in Radial Direction for Cylinder with $L/D = 1.0$ and 3.0 , $w/b = 0.8$, Under Thermal Shrinkage Loading	63
34	Ratio of the Peak Radial Liner Stress Near Flap Termination to Mid-Cylinder Value for Cylinder Under Thermal Shrinkage Loading	64
35	Ratio of Radial Liner Stress in Saddle to Mid-Cylinder Value for Cylinder Under Thermal Shrinkage Loading	65
36	Ratio of Liner Hoop to Radial Stress at Mid-Axial Position in Cylinder Under Thermal Shrinkage Loading	66
37	Average Case Bond Radial Stress in Cylinder Under Thermal Shrinkage Loading	67
38	Correspondence of Stresses and Strains Resulting from Thermal Shrinkage and Internal Pressurization of Two-Layered Cylinders	68
39	Case Bond Liner Stresses Near the Flap Termination for a Cylinder with $L/D = 1.0$ and $W/b = 0.8$ Under 1.0 psi Internal Pressure Loading	69
40	Lines of Constant Maximum Principal Strain (ϵ_{max}) in the Vicinity of the Flap Termination for a Cylinder with $L/D = 1.0$ and $W/b = 0.8$ Subjected to 1000 psi Internal Pressure Loading	70



LIST OF FIGURES (Cont)

<u>Number</u>	<u>Title</u>	<u>Page</u>
41	Case Bond Liner Stresses for a 32-Inch Diameter Cylinder with $L/D = 3.0$ and $W/b = 0.8$ Under 1 g Axial Acceleration Loading ($\rho_W = 0.064 \text{ lb/in.}^3$)	71
42	Case Bond Liner Stresses Adjacent to Flap Termination in a 32-Inch Diameter Cylinder with $L/D = 3.0$ and $W/b = 0.8$ Under 1 g Axial Acceleration Loading ($\rho_W = 0.064 \text{ lb/in.}^3$)	72
43	Lines of Constant Maximum Principal Stress $\left(\frac{\sigma_{\max}}{\tau_{\text{avg}}}\right)$ in the Vicinity of the Flap Termination for a Cylinder with $L/D = 3.0$ and $W/b = 0.8$ Under Axial Acceleration Loading	73
44	Lines of Constant Maximum Principal Strain $\left(\frac{E \epsilon_{\max}}{\tau_{\text{avg}}}\right)$ in the Vicinity of the Flap Termination for a Cylinder with $L/D = 3.0$ and $W/b = 0.8$ Under Axial Acceleration Loading	74
45	Comparison of Gradient in Maximum Principal Stress as a Function of Normalized Radial Distance from Flap-Insulator Bond Discontinuity for Cylinders Under Thermal Shrinkage and Axial Acceleration	75
46	Normalized Case Bond Liner Stresses Adjacent to Flap Termination for Cylinder with $L/D = 3.0$ Subjected to Axial Acceleration Loading	76
47	Normalized Case Bond Liner Stresses Adjacent to Flap Termination for Cylinder with $W/b = 0.8$ Subjected to Axial Acceleration Loading	77

LIST OF TABLES

<u>Number</u>	<u>Title</u>	<u>Page</u>
I	Material Properties Used in Parameter Study	5
II	Comparison of Key Stress Parameters in Cylinders with $W/b = 0.8$ for Case Radial Expansion and Thermal Shrinkage Loadings	22

NOMENCLATURE

a	Radius to inside of grain
b	Radius to inside of case
L	Cylinder length
D	Cylinder diameter
H	Case-Grain stiffness ratio $\left(H = \frac{Eb}{E_{\theta} t_c} \right)$
H_{σ}	Bond stress gradient factor (See Figure 25)
P	Internal pressure
t_c	Case thickness
r	Radial coordinate
θ	Hoop coordinate
Z	Axial coordinate
E	Tensile modulus
K	Bulk modulus
E_{θ}	Hoop modulus of case
E_Z	Axial modulus of case
$C_{\theta\theta}, C_{\theta Z}, C_{Z\theta}, C_{ZZ}$	Orthotropic stress-strain coefficients
ν	Poisson's ratio
$\nu_{\theta Z}$	Poisson's ratio of case in r-Z direction
δ	Shrinkage coefficient ($\delta = a\Delta T$)
ϵ	Total normal strain
$\bar{\epsilon}$	Stress-producing normal strain
σ	Normal stress
τ	Shear stress
σ_{max}	Maximum principal stress
ϵ_{max}	Maximum principal strain

214

SECTION I

INTRODUCTION

Propellant grain survivability depends upon the structural integrity of the grain and all bonded interfaces. Probably more structural failures of motors have occurred at the case bond than in the propellant proper. This is true for at least two reasons: (1) The case bond is inherently weaker than the propellant, and (2) the stresses are highest at the bond lines, particularly at the bond terminations.

Case bonds impose challenges to the structural analyst which are somewhat greater than those imposed by the propellant. These challenges primarily result from geometrical considerations. Layers comprising typical case-bond systems, including insulator and flap components, are very thin compared with the propellant web. While these thin layers do not normally influence bond/propellant stresses over most of the motor, they are important at the critical bond termination locations.

Only limited information has been published which depicts typical case-bond stress distributions in rocket motors. Experimental studies have been accomplished using photoelasticity to evaluate stress distributions at bond terminations.¹ However, these studies did not consider case-bond detail and were restricted to configurations involving fillets and grooves in the propellant grain adjacent to the bond termination. Numerical stress analyses published to date have considered the case bond in varying degrees. Reference 2 contains case-bond stress distributions in cylinders with flat ends; no attempt was made to deal with the actual termination geometry or bond constituents. In later studies,³ however, some consideration was given to the case-bond liner and bond termination configurations. Fracture mechanics theory has been applied to the case-bond problem, with the bond termination considered as a singularity⁴; information derived from these studies has been used to establish the length of flaps. Finite-element stress analyses of motors often consider the case bond; however, stress values obtained at the terminations are often of questionable value because of the lack of adequate grid refinement.

Hercules Incorporated and United Technology Center (UTC) are currently working on RPL-funded programs to develop improved methods for predicting initiation and propagation of failures in case-liner-bond systems. The Hercules program involves initiation of case-bond failure; whereas, the UTC program primarily involves propagation of case-bond failures. The Hercules program consists of four tasks involving: (1) Bondline Parametric Studies, (2) Test Sample Development for Simple States of Stress, (3) Failure Criteria for Bond Terminations, and (4) Subscale Motor Testing. This report documents studies performed under Task 1.

The objective of Task 1, Bondline Parametric Studies, is to establish case-bond stress distributions in basic motor configurations, with emphasis on bond terminations. The study involved simple cylinders containing flapped ends. Finite-element models were developed with highly refined grids in the vicinity of the flap terminations so that variations in case-bond constituents could be evaluated. Loading conditions considered were thermal shrinkage, internal pressurization, and axial acceleration. Information obtained under Task 1 will be used to develop meaningful case-bond failure criteria and associated test sample configurations, as outlined in the remaining three tasks. However, because of its applicability to propellant grain stress analysis in general, information gained under Task 1 is being published as an interim report.

This report first describes the modeling procedure. Results are then presented for thermal shrinkage loading. An equivalence is developed for thermal and pressure loading conditions such that thermal solutions can be used for internal pressure loading conditions as well. Results are subsequently presented for internal pressure loading and compared with predictions based on the thermal loading solutions. Finally, results are presented for axial acceleration loading.

SECTION II

MATHEMATICAL MODELING

The parameter study was restricted to flat-ended cylinders, which are symmetric about the axial mid-plane, as shown in Figure 1. The cylindrical propellant grains were bonded to the case, with flaps at the end terminations. Emphasis was placed on modeling local detail in the case-bond system, including the insulator, flap, and case-bond liner. Stress solutions were obtained for the three basic loading conditions: Thermal shrinkage, internal pressurization, and axial acceleration.

Stress solutions were obtained using a finite-element computer program based on the quadrilateral ring element, composed of four adjacent triangular elements. The program developed by Hercules is similar to the well-known Rohm & Haas program.⁵ The Hercules program is reformulated for solution of problems with Poisson's ratio near 0.5. Since the reformulation variable is eliminated through partitioning at the element stiffness matrix level, solutions cannot be obtained for $\nu \approx 0.5$. The program capacity allows grid networks with up to 3,000 nodes. Double-precision is used in the program to obtain accurate stress solutions using the IBM System 360-370 series computers. Normal stress oscillations inherent in finite-element solutions using quadrilateral elements were minimized through grid refinement in areas of high stress gradient and through averaging of stresses in adjacent elements.

The parameter study considered nine cylindrical configurations consisting of three values of length-to-diameter ratio (L/D) and three values of web fraction (W/b). The grid network for $L/D = 1$, and $W/b = 0.3$ is shown in Figure 2. The basic cylinder diameter is 32 in. to the inside of the case. Symmetry conditions were imposed at the axial mid-plane such that only one half of the cylinder length was included in the model.

Local detail in the region of the flap termination is indicated in Figure 3. To facilitate modeling it was necessary to specify dimensions of the cylinders. The insulator is 0.2-in. thick, and the flap is 0.1-in. thick. The flap length (length of unbondedness between insulator and flap at the end termination) is 1.0 in., and the liner thickness is 0.06 in. Elements in the insulator are 0.5-in. thick (four elements to total 0.2 in.), elements in the flap are 0.025-in. thick, and elements in the liner graduated from a minimum of 0.01-in. to a maximum of 0.02-in. thick. Elements in the propellant adjacent to the liner are graduated in thickness away from the liner, with a minimum element thickness of 0.02 in. The element structure in the radial direction is carried through in a uniform manner along the total cylinder length. Element sizes in the axial direction are graduated to provide minimum element lengths of 0.02-in. in the region of the flap termination. The grid contains 2,420 total nodes.

Grid networks for web fractions and lengths different from $W/b = 0.8$ and $L/D = 1.0$ are similar to that shown in Figure 2. In all grids, the basic cylinder diameter and insulator and flap thicknesses were kept the same. The web fraction was changed by altering the port diameter, and the length-to-diameter ratio was changed by altering the length. The grid structure within 4-in. radially and 5-in. axially of the flap termination was kept the same in all grids for the various web fractions and length-to-diameter ratios. The grids for $L/D = 3.0$ were derived from the grids for $L/D = 1.0$ using the same number of nodes and increasing the lengths of the elements closest to the axial mid-plane, where stress gradients are minimum in the axial direction. The grids for $L/D = 5.0$ were derived from the grids for $L/D = 3.0$ by adding additional elements near the axial mid-plane, to provide a total of 2,640 nodes. Variations in the web fraction were obtained by decreasing radial spacing between nodes inboard of the 12-in. radial line in the grids for $W/b = 0.8$, without changing the total number of nodes. The thickest row of elements near the center port, 0.2-in. thick, occurred in the grid for $W/b = 0.8$.

Material property variations considered in the parameter study (Table I) were kept to a minimum. The propellant tensile modulus was selected as $E = 200$ psi, which is approximately the longterm (rubbery) tensile relaxation modulus of many solid propellants. The propellant bulk modulus was selected as $K = 333,000$ psi, which is the lower bound of published data for most propellants. The tensile/bulk modulus combination provides a value for Poisson's ratio of $\nu = 0.4999$ for propellant.

The case-bond liner was assumed to have a tensile modulus equal to one half that of propellant for some stress solutions, but equal to that of the propellant in most solutions. The bulk modulus of the liner, flap, and insulator was considered to be the same as for propellant. (This choice for the flap and insulator is consistent with data for NBR/SBR rubber.⁶) The tensile modulus of the insulator and flap was considered to be equal to that of propellant in some solutions and equal to the approximate long-term tensile relaxation modulus of silica-filled NBR/SBR rubber (1000 psi) in most solutions. The shrinkage coefficient of the insulator, flap, and liner was considered to be the same as for propellant. For thermal shrinkage and axial acceleration loading, the motor case was assumed to be rigid. For internal pressure loading, approximate fiberglass-reinforced epoxy properties were used.

TABLE I
MATERIAL PROPERTIES USED IN PARAMETER STUDY

	Propellant	Case-Bond Liner	Flap	Insulator	Case
E (psi)	<u>200</u>	100, <u>200</u>	200, <u>1000</u>	200, <u>1000</u>	4,000,000 (t = 0.1 in.), <u>rigid</u>
K (psi)	<u>333,000</u>	<u>333,000</u>	<u>333,000</u>	<u>333,000</u>	
ν	<u>0.4999</u>	0.49995, <u>0.4999</u>	0.4999, <u>0.4995</u>	0.4999, <u>0.4995</u>	<u>0.1</u>
ξ (in./in.)	<u>1</u>	<u>1</u>	<u>1</u>	<u>1</u>	0

NOTE: Values underlined were used in parameter study considering variable web fraction and length-to-diameter ratio for thermal loading conditions

SECTION III

RESULTS FOR THERMAL SHRINKAGE LOADING

Stress solutions for thermal shrinkage loading were obtained with the case (i.e., the outer diameter of the insulator) considered to be thermally and mechanically rigid. The propellant, liner, flap, and insulator were then assumed to shrink by the amount, δ .

Results will be first discussed for a typical set of motor parameters, with case-bond stresses shown as a function of axial position, and contour plots for the region of the bond termination. Effects of changes in the flap, liner, and insulator moduli on the case-bond stresses will then be described. Results will be subsequently discussed for variations in the flap length. Case-bond and centerport stresses and strains will then be outlined for parametric variations in the grain web fraction and length-to-diameter ratio.

Cylinder parameters selected for the "typical" motor analysis are: $L/D = 1$, $W/b = 0.8$, $E_{\text{insulator}} = 1000$ psi, $E_{\text{flap}} = 1000$ psi, and $E_{\text{liner}} = 200$ psi (i.e., same as propellant). Stresses in the cylindrical coordinate directions for these properties are shown in Figure 4 for the row of elements in the case-bond liner next to the flap. As shown in Figure 3, the center of this element row is located 0.105 in. inboard of the insulator (0.005 in. into the liner). The stresses were made dimensionless by dividing by $E\delta$. These dimensionless stresses are strictly valid only for conditions wherein the insulator/flap modulus is five times as high as the propellant modulus, and for the given values of Poisson's ratio.

The stresses at the flap termination are shown in Figure 4; they are shown to be much higher than at the axial mid-plane of the cylinder ($Z = 16$ in., considering a 32.0-in. cylinder diameter). Radial stress values averaged between adjacent elements are shown by the circles to indicate grid spacing and stress gradient versus element size; point values are not indicated for the other stresses. The dimensionless radial stress near the bond termination reaches a value of 17.5, while it is only 3.8 at the axial mid-plane. The dimensionless hoop stress peaks at 12.3 near the bond termination, while the dimensionless axial stress peaks at 8.3. The hoop and axial stresses are 60 percent greater than the radial stress at the axial mid-plane. The dimensionless shear stress peaks at 6.3 near the flap termination and goes through zero at mid-cylinder, as specified in the boundary conditions for symmetry.

Stress values in the immediate vicinity of the flap termination are shown in Figure 5. Gradients are well defined by the finite-element model. The radial stress peaks 0.05 in. aft of the flap termination (i.e., a distance approximately equal to one-half the flap thickness). The hoop stress is not shown, but it peaks at the same point as the radial stress. The axial stress is still increasing along the length after the

radial and hoop stresses have peaked. The shear stress changes direction at the flap termination, and peaks approximately 0.15 in. aft. The maximum principal stress peaks slightly to the right of the radial stress (as a result of the increasing shear stress) at a value of 18.7; the radial stress, as compared with the shear stress, is by far the largest contributor to the maximum principal stress. The maximum principal strain, ϵ_{\max}/δ , is also shown in Figure 5; this quantity follows very closely the characteristics of the maximum principal stress.

Lines of constant maximum principal stress in the vicinity of the flap termination are shown in Figure 6. The discontinuity at the bond termination between the flap and insulator is well defined by the sharp stress gradient. Since the solution is linear, infinite stresses should be predicted at the discontinuity; however, the finite-element model provides stress values consistent with the grid detail utilized. The stress values at the flap-liner interface are accurately estimated with the chosen grid density, even though values become more in error as the discontinuity is approached. The principal stress is not necessarily continuous across material boundaries. However, since the radial and shear stresses, which must be continuous, are the major contributor to the maximum principal stress, the lines almost cross material boundaries.

Lines of constant maximum principal strain are shown in Figure 7. Unlike the stress values, the strain values are quite discontinuous across the flap-liner boundary. In the flap, there is the expected concentration at the flap-insulator bond termination discontinuity; however, there is also an unexpected concentration at the flap-liner interface. This results from a reduction in the triaxiality of the stresses, rather than by any stress concentration.

A. MATERIAL PROPERTY EFFECTS

The first variation from the basic solution involved softening of the flap material from $E = 1000$ psi to $E = 200$ psi, making it the same as propellant. Overall effects of this change were very small. Local effects at the flap termination, as shown in Figure 8, were most significant, but still relatively small. Radial and maximum principal stresses showed almost no change from the stiffer flap solution. The shear stress maximum increased approximately 6.3 percent over the stiffer flap solution. The largest effects were felt in the maximum principal strain and the axial stress. With the softer flap material, the axial stress decreased significantly at the flap termination, as shown in Figure 9, although it built up to the same level as for the stiff flap solution 0.5 in. further aft. This local reduction in axial stress caused a more uniaxial stress condition to occur near the location of the maximum strain, thus increasing its value from a maximum of 10.8 to 13.1. There was an insignificant change in the local hoop stress.

Lines of constant maximum principal stress and strain for the soft-flap solution are shown in Figures 10 and 11, respectively. The maximum principal stress values in the liner/propellant are almost identical for stiff and soft flap solutions. However, the stress concentration in both the flap and the insulator is significantly reduced near the bond termination by softening the flap. Thus, softening of the flap has a significant bearing on the stresses in the rubber goods even though the effect on the bond stresses is minimal. Lines of constant strain do not indicate the concentration effect in the flap adjacent to the liner evident in the stiff-flap solution. The strain contour lines tend to curve back toward the concentration more than the stress lines, indicating the increased triaxiality of the stresses further aft of the termination.

The next variation in material properties involved a decrease in the tensile modulus of the liner, reducing it from 200 to 100 psi. For this solution, the tensile modulus of the flap was kept at 200 psi, as opposed to the standard value of 1000 psi. Case-bond stresses and strains adjacent to the flap termination for the soft liner solution are shown in Figures 12 through 15; values are plotted for the row of elements in the propellant nearest the liner (i.e., 0.01 in. inboard of the liner-propellant interface, and 0.17 in. inboard of the flap-insulator interface). (See Figure 3.) Lines of constant maximum principal stress and strain for the soft-liner solution are shown in Figures 16 and 17, respectively. In general, the soft liner (in addition to the soft flap) had little effect on the stresses and strains in the propellant or at the liner-propellant interface. The maximum radial stress was reduced near the liner-propellant interface by 2 percent, the shear stress by 5 percent, the maximum principal stress by 2 percent, and the maximum principal strain by 7 percent, as compared with the soft flap solution.

The contour lines of maximum principal stress shown in Figure 16 for the soft liner solution indicate little change in the stresses in the liner itself, compared with the soft-flap solution. However, the contours for the maximum principal strain in Figure 17 indicate that the liner is shearing significantly, several flap thicknesses to the right of the flap termination. The larger liner shear strain, however, has little effect on the stresses and strain in the propellant or at the liner-propellant interface.

The final variation in material properties considered the insulator to have the same tensile modulus as the propellant, liner, and flap ($E = 200$ psi). Stresses and strains in the row of propellant elements immediately inboard of the liner are shown in Figures 12 through 15 for this solution. The soft-insulator solution provided the largest overall decrease in bond stresses and strains, i.e. a uniform 11-percent decrease in all the stresses and strains, as compared with the soft-flap solution.

Contour lines of maximum principal stress and strain for the soft insulator solution are shown in Figures 18 and 19, respectively. The stress contours indicate a significant reduction in the stress levels near the insulator-flap bond discontinuity, as compared with the other solutions. Both stress and strain contour lines are continuous across material interfaces since the material layers are assumed to have the same moduli.

In summary, none of the material property variations provided a significant change in the stresses at the case-bond interface adjacent to the flap termination, except perhaps softening of the insulator. Softening of the flap (and probably softening of the liner considering a stiffer flap) reduced the axial stress locally at the flap termination such that the maximum propellant strain increased significantly, without measurably affecting the radial/shear/maximum principal stresses. Softening of the liner increased the shear strain (and hence the maximum principal strain) in the liner for a distance to the right of the bond termination, but affected the liner/bond stresses very little.

Perhaps the most significant feature of the variable-modulus solutions is the large stress gradients, both radially and axially, with distance from the discontinuity at the insulator-flap bond termination. The maximum principal stresses in each row of elements are shown in Figure 20 as a function of the radial position, normalized to unity at the flap-liner interface, for the soft flap solution. The stress varies according to the ratio $\frac{K}{\sqrt{S}}$, where K is a constant and S is the distance from the discontinuity. This variation is consistent with the fracture mechanics theory. By doubling the flap thickness, the stress is reduced to 72 percent of that for the standard 0.1-in. flap thickness, and by tripling the flap thickness, the stress factor goes to 60 percent. Also shown in Figure 20 are stiff-flap stresses which have been normalized with respect to the stress at the flap-liner interface for the soft flap. Only two points are plotted for the stiff flap solution since these are sufficient to show that stiffening of the flap had no effect on the stresses inside the propellant. Corresponding normalized stresses for the soft liner solution indicate a similarly insignificant effect on the stress level inside the propellant. Thus, the propellant stresses are essentially a function of the radial distance from the flap-insulator bond discontinuity only, regardless of the material layers (within the range considered) between the propellant and the discontinuity. Case-bond stresses can be reduced by either thickening the flap or the liner. A similar conclusion cannot be reached for the maximum principal strain since it was shown to be sensitive to the flap modulus. The stress behavior, however, provides a valuable procedure for estimating the effects of flap/liner thickness on the bond stresses using stress solutions for a single flap thickness.

R. FLAP LENGTH EFFECTS

Adjustment of the flap length is a common technique for minimizing propellant/case-bond stresses. Information relating to flap length effects is available from several sources. A simple procedure for sizing flaps was outlined by Lockheed Propulsion Company⁷, wherein grain end unbonding was observed in motors without release flaps. An empirical curve has been derived from motors with web fractions near 50 percent and length-to-diameter ratios between 1.0 and 3.0. Based on these data, a flap with an approximate length of 1.0 in. is desirable for a 32-in. diameter cylinder.

Information concerning flap length effects has been derived using fracture mechanics principles.⁴ In fracture mechanics solutions, a singularity is assumed at the point of initial unbonding. The unbond is assumed to propagate when the strain energy in the loaded motor, released by a small increase in the unbond, exceeds the energy required to create a new bond surface of the same area. In general, as the amount of unbonding increases under thermal loading, the overall stresses and strains in the motor decrease, and hence, the strain energy decreases. However, as shown in Reference 4, the motor energy release rate is a complex function of the motor web fraction, length-to-diameter ratio, and length of unbond.

The primary objective of the study of flap length reported here is to evaluate the effect of varying flap length on the local case-bond stress distribution at the flap termination. The study is somewhat limited, with flap lengths of 0.1, 0.5, and 1.0 in. considered for a cylinder L/D of 1.0 and W/b of 0.8. Finite-element models for the two shorter flap conditions were very similar to that for the 1.0-in. flap model; special attention was given to keeping the grid sizes near the flap termination identical in all three models.

Case-bond radial and shear stresses adjacent to the flap termination are shown in Figures 21 and 22, respectively, for the three different flap lengths. Stresses are reported for the row of elements in the liner, closest to the flap. The radial stresses for the 0.1- and 0.5-in. flaps peak at the same level; whereas, the peak for the 1.0-in. flap is 3 percent lower. The shear stresses for the 0.5- and 1.0-in. flaps peak (negative peak) at values significantly less (13 percent) than for the 0.1-in. flap. Overall, however, it is surprising that the stresses for a flap only as long as its thickness are as close as they are to those for the longer flaps.

The largest value of the maximum principal stress in the row of elements in the liner closest to the flap is plotted in Figure 23 as a function of the normalized flap length. For the 0.1-in. flap, the largest stress value is only 6 percent greater than for the 1.0-in. flap. Thus, changes in the bond stresses are relatively insensitive to changes in flap length over the limited range studied and flap thickness has a much greater effect on the case-bond stresses at the flap termination than does flap length.

The strain energy in the finite-element model is shown in Figure 24 as a function of the normalized flap length. The three values calculated provide a straight line, indicating that the energy release rate is constant. This is consistent with local stresses being almost independent of flap length; differences between energy and local stress criteria can probably be explained by the limited number of solutions used to define the energy-versus-flap-length curve. Considering $S \leq 1.0$ in., flap length effects on the local case-bond stresses for cylinders with smaller web fractions and larger L/D ratios are expected to be less than those for the stubby cylinder which was studied, based on energy release rate curves contained in References 2 and 4.

C. WEB FRACTION AND LENGTH/DIAMETER (L/D) STUDIES

Overall case-bond stress distributions in cylinders have been shown to be sensitive to web fraction and length-to-diameter ratio. (See Reference 2 for example.) It is important, therefore, that the current study consider as an objective the evaluation of case bond stress distributions for variations in W/b and L/D . A secondary objective is to provide design charts which can be used to estimate maximum values of case-bond stresses at flap terminations.

The study considered nine cylinder configurations: $L/D = 1, 3$, and 5 , for $W/b = 0.5, 0.67$, and 0.8 . The cylinder diameter was held constant at 32 in. for these studies; thus, L/D was varied by changing L and W/b was varied by changing propellant bore diameter. The thickness and modulus of the flap and insulator, the length of the flap, and the modulus of the propellant were kept the same in all nine solutions. Modulus values used in the study are indicated in Table I. The insulator thickness of 0.2 in. is the same as for all previous solutions, and the flap thickness of 0.1 in. and the length of 1.0 in. is also the same as that used in previous solutions.

Data shown in Figure 20 indicate that the propellant stress adjacent to the flap termination is not strongly affected by the modulus of the flap or liner. Thus, the stresses obtained in a computer solution for a given flap/liner thickness can be made to apply to conditions in which the flap and liner thickness vary. Bond normal stresses are presented parametrically as $\frac{\sigma}{H_\sigma}$, where H_σ is a function of the radial distance, \bar{r} , of the propellant-to-liner bondline from the flap-to-insulator bondline; for a liner-bond system, $\bar{r} = t_{\text{flap}} + t_{\text{liner}}$ when the critical failure location is between the propellant and liner. The value for H_σ is presented in Figure 25 as a function of the normalized thickness, \bar{t}/b . The value H_σ was normalized such that it would be unity at a distance of 0.1 in. from the flap-insulator bondline, where stresses are obtained conveniently from the finite-element solutions. The value for H_σ may be a function of W/b and L/D ; the value shown in Figure 25 is for $L/D = 1.0$ and $W/b = 0.8$. Figure 26 contains a comparison of H_σ for the extreme values of cylinder parameters studied (i.e., $L/D = 1$, $W/b = 0.8$, and $L/D = 5$, $W/b = 0.5$).

There is a negligible difference in H_0 for these extreme conditions, indicating that the stress distribution adjacent to the flap termination is a function of the local flap-insulator geometry and not the overall cylinder geometry. Furthermore, the radial stress gradient near the flap termination, as shown in Figure 26, is so close to that for the maximum principal stress that H_σ in Figure 25 applies to both stress components, although it was obtained from the maximum principal stress. As shown in Figure 26, H_σ for normal stresses does not apply to the τ_{rz} shear stress. The peak value of the shear stress does not decrease as rapidly with distance from the discontinuity as do the normal stresses.

A relationship for the strain components as a function of flap thickness cannot be obtained with confidence from a solution for one flap thickness since the flap modulus significantly affects the strain magnitude, as shown in Figures 5 and 8. Results are provided, however, for the basic flap thickness to indicate variations with cylinder web fraction and length.

The dimensionless radial stress adjacent to the flap termination is shown in Figure 27 as a function of L/D for the three web fractions. Values change significantly between $L/D = 1.0$ and 3.0 , and little thereafter; the greatest effect occurs for the largest web fraction. Also indicated in Figure 27 is the ratio of the shear stress τ_{rz} to the radial stress at the location of the maximum radial stress for the standard flap/liner thickness, $\bar{t} = 0.105$ in. The stress ratio changes very little with web fraction and length, indicating that the local stress distribution (shown in detail earlier) for $L/D = 1.0$ and $W/b = 0.8$ is characteristic of other cylinder configurations as well.

To illustrate the use of parametric information in Figure 27 for design purposes, consider a motor with the following dimensions:

<u>Item</u>	<u>Value</u>
Case Diameter, D	12 in.
Flap Thickness, t_f	0.08 in.
Liner Thickness, t_l	0.05 in.
L/D	2
W/b	0.75
$t_{\text{insulator}}/b$	$0.2/16 = 0.0125$
$E_{\text{insulator}}/E_{\text{propellant}}$	5
$\nu_{\text{insulator}}$	0.4999
ν_{flap}	0.4995
ν_{liner}	0.4999

The interpolated value of $\left(\frac{\sigma_r}{H_{\sigma} E \delta}\right)_{\text{bond}}$ from Figure 27 is approximately 24.0. The normalized sum of the liner and flap thickness is,

$$\bar{t}/b = (0.08 + 0.05)/12 = 0.0108 ;$$

thus, H_{σ} from Figure 25 is 0.79. (The critical case-bond stress location is assumed to be between the liner and propellant, not between the flap and liner.) Assuming,

$$E = 500 \text{ psi}$$

$$\delta = \alpha \Delta T = 0.004 \text{ in./in.},$$

then

$$\sigma_r = (0.19) (500) (0.004) (24) = 37.9 \text{ psi}$$

The case-bond shear stress at this location is approximately

$$\tau_{rz} = (0.19) (37.9) = 7.2 \text{ psi}$$

The dimensionless maximum principal stress adjacent to the flap termination is shown in Figure 28 and the maximum principal strain is shown in Figure 29. The strain is located at $\bar{t}/b = 0.0066$ only, and varies with web fraction and length similar to the stresses. Also shown in Figure 29 are the ratios of the other two principal stresses to the maximum principal stress at the location of the maximum principal strain (same location as the maximum principal stress for $\bar{t}/b = 0.0066$). The hoop stress is approximately 65 percent of the maximum principal stress, and the smallest principal stress is approximately 20 percent of the maximum principal stress. There is only a small variation in the stress ratios with L/D and W/b .

For completeness, the centerport hoop stress and strain at the mid-cylinder is presented in Figures 30 and 31, respectively. These curves are almost identical to those presented in Reference 8, wherein finite difference methods were used for the calculations. The strain values are for the stress-producing strain, $\bar{\epsilon} = \epsilon + \delta$, as opposed to the total strain, $\epsilon = u_r/r$. The centerport stress and strain do not level off as quickly with increasing L/D as do the bond termination stresses and strains. The ratio of the axial stress (a principal stress) to the hoop stress at the mid-cylinder is indicated in Figure 31. This stress ratio changes dramatically with L/D and W/b , and is approximately 0.5 (i.e., 2:1 biaxial) for L/D , greater than 3.0, and approaches zero (uniaxial) for L/D equal to 1.0.

The ratio of the maximum principal stress at the flap termination to the maximum centerport hoop stress is shown in Figure 32. As the web fraction and length-to-diameter ratio decrease, the bond termination stress becomes much larger than the centerport hoop stress. For high L/D cylinders with large web fractions, the centerport hoop stress becomes larger than the bond termination stress, although the bond termination stress can be adjusted appreciably by the flap/liner thickness ($H\sigma$).

The case-bond radial stress distribution as a function of motor length varies greatly with L/D, as indicated in Figure 33. For L/D = 1.0 and W/b = 0.08, the radial stress at the mid-cylinder is much less than at the flap termination. However, for L/D = 3.0, the radial stress increases significantly near the mid-cylinder, and a distinct saddle region of minimum stress occurs to the right of the flap termination. The ratio of the maximum case-bond radial stress at the flap termination to the case-bond radial stress at the mid-cylinder is shown in Figure 34 as a function of L/D and W/b. The trend for this ratio is similar to that for the flap-centerport hoop stress ratio; however, the radial bond stress is less than the centerport hoop stress at the mid-cylinder location. The ratio of the case-bond radial stress at the saddle to that at the mid-cylinder is shown in Figure 35. The saddle deepens with increasing L/D and W/b.

It was shown in Figure 4 that the hoop and axial stresses along the case-bond line are greater than the radial stress, except near the flap termination. This may be somewhat surprising at first glance. However, the plane strain cylinder solution for thermal loading predicts that

$$\left(\frac{\sigma_{\theta}}{r_r}\right)_{r=b} = \frac{b^2 + a^2}{b^2 - a^2}$$

for $\nu = 0.5$ and a rigid case. Thus, as the web fraction decreases, the hoop stress at the bond becomes larger than the radial stress. The finite-element results for the ratio of the hoop stress to the radial stress at the mid-cylinder bond location are given in Figure 36. The dependence upon web fraction for large values of L/D (approaching plane strain) follows the plane strain predictions. In addition, the hoop stress increases in magnitude over the radial stress as L/D decreases. The axial stress at the mid-cylinder is equal (within 1-percent error) to the hoop stress.

The average case-bond radial stress is shown in Figure 37 for the various cylinder parameters. The distribution indicates an increasing average load on the case with increasing L/D and W/b.

SECTION IV

THERMAL-PRESSURE LOADING EQUIVALENCE

Much similarity exists between the stress solutions for continuaums subjected to restrained thermal shrinkage and pressure loadings. (See Reference 9, for example.) This similarity can be used to advantage in both stress and strength analysis of solid propellant rocket motors. In particular, the number of stress solutions required to depict typical case-bond stress distributions in two-layered, finite-length cylinders can be reduced in the current parameter study by taking advantage of this equivalence.

A pictorial presentation of propellant (and case bond) stresses and strains in cylindrical rocket motors with free ends, subjected to thermal shrinkage and internal pressure loading, is given in Figure 38. During thermal shrinkage loading, propellant normal stresses (σ), shear stresses (τ), and stress-producing strains ($\bar{\epsilon}$) occur because the propellant has a higher coefficient of thermal expansion than the case.

The stresses, strains, and deformations for thermal loading can be separated into those resulting from two situations, free shrinkage and case expansion, as indicated in Figure 38-a. Assuming that the propellant is disconnected from the case and allowed to uniformly shrink, zero normal and shear stresses will result. By definition, the stress-producing strains ($\bar{\epsilon}$) will also be zero; the total strains (ϵ) will then be equal to the negative of the linear shrinkage coefficient (δ_p). The case will also shrink, but normally much less than the propellant. When the case and propellant are bonded together, interface stresses will occur at the case-bond line. The case deformation resulting from these stresses is usually small, but is dependent upon the relative grain-to-case stiffness ratio in the coupled system, as are the interface stresses. For convenience of presentation, consider that the case deformation due to the interface stresses is known and included in the free shrinkage solution. The propellant stresses for restrained shrinkage loading can then be viewed as those which occur when the outer boundary of the shrunk propellant cylinder is pulled out to make contact with the deformed case (i.e., case expansion loading), as indicated in the right side of Figure 38-a. Since the propellant grain under free shrinkage loading was assumed to uniformly shrink such that all total normal strains are equal to " $-\delta_p$ ", and the case deformation is usually small due to the interface stresses, the hoop strain (ϵ_θ) will be approximately equal to the axial strain (ϵ_z) all along the case-bond line for case expansion loading. Strength analysis is most logically carried out in terms of stress producing strains, $\bar{\epsilon}$, as opposed to total strains, ϵ .

During uniform internal pressure loading, propellant stresses (other than hydrostatic pressure stresses) and strains occur because the case expands and the grain follows to take up the increased volume inside the deformed chamber. The stresses, strains, and deformations for uniform internal pressure loading can be separated into those resulting from two situations, hydrostatic pressure and case expansion, as indicated in Figure 38-b. Assuming that the propellant is disconnected from the case and subjected to uniform hydrostatic pressure, all normal stresses will be equal to $-P$ and all shear stresses will be zero; the normal strains will be equal to $\frac{P}{3K}$. Consider now a strain definition corresponding to that for the stress-producing strain, $\bar{\epsilon}$, under thermal loading. In the pressure loading situation, this "stress-producing strain," $\bar{\epsilon}$, corresponds to that required to produce normal stresses different from $-P$; thus, $\bar{\epsilon}$ by definition is zero for hydrostatic pressure loading.

For convenience of presentation, consider that the case deformation due to interface stresses and end forces is known for internal pressure loading, even though it is a function of the coupled grain/case system. The propellant stresses considering the propellant and case are bonded together can then be viewed as those for hydrostatic pressure loading, plus those which occur when the outer boundary of the compressed propellant cylinder is pulled out to make contact with the deformed case. The case strains for an empty metal chamber will be such that $\epsilon_z \approx \frac{1}{2} \epsilon_\theta$; considering a filament-wound glass, ϵ_z will be typically as large as ϵ_θ . Considering a case designed to produce a hoop strain of 0.01 in./in. at 1000 psi internal pressure, and a propellant with a bulk modulus of 333,000 psi, the propellant strain due to uniform hydrostatic compression will be $\epsilon = \frac{-1000}{1 \times 10^6} = -0.001$ in./in., which is 10 percent of the empty case hoop strain. The empty case expansion component of loading can usually be expected to dominate the propellant compressibility component of loading.

SECTION V

LOAD SHARING OF CASE AND GRAIN

The interface stresses between the case and grain are a function of the relative grain-to-case stiffness. A procedure for estimating the case deformation which results from the interface stresses is derived in the following paragraphs. Pressure loading, which produces the most complex case-grain coupling, is discussed in detail; then, case-grain coupling is summarized for thermal loading.

A. INTERNAL PRESSURE LOADING

Consider a two-layered cylinder subjected to internal pressure loading. The case hoop and axial stresses can be approximately expressed as:

$$\sigma_{\theta} = (P - \sigma_{\text{bond}}) \frac{b}{t_c}$$

$$\sigma_z = \frac{Pb}{2t_c} - \tau_{\text{bond}}$$

The term " σ_{bond} " represents the average internal pressure load carried by the grain, and τ_{bond} relates to the shear stress at the interface. The pressure load carried by the grain is highest near the end terminations, where there is a sharp stress concentration, and near the axial mid-plane where gross end relief effects diminish. The shear stress is highest near the end terminations and changes sign at the axial mid-plane such that the integral of the shear is zero over the total length. Shear is secondary compared with the radial stress effect, and will be ignored in further considerations.

For a membrane case, the orthotropic stress-strain relationships are:

$$\epsilon_{\theta} = C_{\theta\theta} \sigma_{\theta} + C_{\theta z} \sigma_z$$

$$\epsilon_z = C_{z\theta} \sigma_{\theta} + C_{zz} \sigma_z$$

Substitution of the above stress-load relationships (minus the shear) into the stress-strain relations provides:

$$\epsilon_{\theta} = C_{\theta\theta} (P - \sigma_{\text{bond}}) \frac{b}{t_c} + C_{\theta z} \left(\frac{Pb}{2t_c} \right)$$

$$\epsilon_z = C_{z\theta} (P - \sigma_{\text{bond}}) \frac{b}{t_c} + C_{zz} \left(\frac{Pb}{2t_c} \right)$$

Upon regrouping these expressions, the following are obtained:

$$\epsilon_{\theta} = \bar{\epsilon}_{\theta} - C_{\theta\theta} \frac{b}{t_c} \sigma_{\text{bond}}$$

$$\epsilon_z = \bar{\epsilon}_z - C_{\theta z} \frac{b}{t_c} \sigma_{\text{bond}}$$

where $\bar{\epsilon}_{\theta}$ and $\bar{\epsilon}_z$ are the case strains in the absence of the grain.

The average interface radial stress carried by the grain, σ_{bond} , is a function of both the radial and axial case strains. Consider functions

$$\left(\frac{\sigma_r}{E \epsilon_{\theta}} \right)_{\text{avg}} \quad \text{and} \quad \left(\frac{\sigma_r}{E \epsilon_z} \right)_{\text{avg}},$$

which are the average dimensionless bond radial stresses for arbitrary (case expansion loading) hoop and axial case strains. Further, recognize $C_{\theta\theta} = \frac{1}{E_{\theta}}$ and $C_{\theta z} = -\frac{\nu_{\theta z}}{E_{\theta}}$. Then the hoop and axial case strains are related as:

$$\epsilon_{\theta} = \bar{\epsilon}_{\theta} - \frac{Eb}{E_{\theta} t_c} \left[\left(\frac{\sigma_r}{E \epsilon_{\theta}} \right)_{\text{avg}} \epsilon_{\theta} + \left(\frac{\sigma_r}{E \epsilon_z} \right)_{\text{avg}} \epsilon_z \right]$$

$$\epsilon_z = \bar{\epsilon}_z + \nu_{\theta z} \frac{Eb}{E_{\theta} t_c} \left[\left(\frac{\sigma_r}{E \epsilon_{\theta}} \right)_{\text{avg}} \epsilon_{\theta} + \left(\frac{\sigma_r}{E \epsilon_z} \right)_{\text{avg}} \epsilon_z \right]$$

These equations can be solved for ϵ_{θ} and ϵ_z , as:

$$\epsilon_{\theta} = \frac{(1 - \nu_{\theta z} H \sigma_{rz}) \bar{\epsilon}_{\theta} - (H \sigma_{rz}) \bar{\epsilon}_z}{(1 - \nu_{\theta z} H \sigma_{rz}) (1 + H \sigma_{r\theta}) + \nu_{\theta z} H^2 \sigma_{rz} \sigma_{r\theta}}$$

and

$$\epsilon_z = \frac{\bar{\epsilon}_z + (\nu_{\theta z} H \sigma_{r\theta}) \epsilon_{\theta}}{1 - \nu_{\theta z} H \sigma_{rz}}$$

where:

$$H = \frac{Eb}{E_{\theta} t_c}, \quad \sigma_{r\theta} = \left(\frac{\sigma_r}{E \epsilon_{\theta \text{ case}}} \right)_{\text{avg}}, \quad \text{and} \quad \sigma_{rZ} = \left(\frac{\sigma_r}{E \epsilon_{Z \text{ case}}} \right)_{\text{avg}}$$

B. THERMAL SHRINKAGE LOADING

Case axial and hoop stresses for thermal shrinkage loading can be approximately expressed as:

$$\sigma_{\theta} = (-\sigma_{\text{bond}}) \frac{b}{t_c}$$

$$\sigma_Z = 0$$

The stress producing case strains are related to the average bond radial stress as:

$$\bar{\epsilon}_{\theta} = \frac{1}{E_{\theta}} (-\sigma_{\text{bond}}) \frac{b}{t_c}$$

$$\bar{\epsilon}_Z = \frac{-\nu_{\theta Z}}{E_{\theta}} (-\sigma_{\text{bond}}) \frac{b}{t_c} = -\nu_{\theta Z} \bar{\epsilon}_{\theta}$$

The average bond radial stress, $\left(\frac{\sigma_r}{E\delta} \right)_{\text{avg}}$, is presented in Figure 37 for variations in L/D, W/b, E, and δ of a cylinder with a rigid case. Thus,

$$\sigma_{\text{bond}} \approx \left(\frac{\sigma_r}{E\delta} \right)_{\text{avg}} E\delta,$$

and:

$$\bar{\epsilon}_{\theta} \approx -H \left(\frac{\sigma_r}{E\delta} \right)_{\text{avg}} \delta; \quad \bar{\epsilon}_Z \approx -\nu_{\theta Z} \bar{\epsilon}_{\theta}$$

The stresses for thermal shrinkage loading, considering a flexible case, are then approximately equal to those for a rigid case plus those for case expansion loading of the amount estimated above. Since the case strains are negative, however, the flexible case solution will provide lower stresses than the rigid case solution.

SECTION VI

RESULTS FOR INTERNAL PRESSURE LOADING

A. DIRECT INTERNAL PRESSURE LOADING RESULTS

The case-bond stress distribution for a typical set of cylinder parameters was obtained for internal pressure loading applied to the finite-element model. The propellant, liner, and insulator properties used are those underlined in Table I. However, the flap modulus was 200 psi and the motor case was not assumed to be rigid; a case with thickness, $t_c = 0.1$ in. ($t_c/b = 0.00625$), a tensile modulus, $E_c = 4 \times 10^6$ psi, and Poisson's ratio, $\nu_c = 0.1$ were used. These case properties provide a mid-cylinder case hoop strain of 1.85 percent at 500 psi internal pressure, which is typical of fiberglass-reinforced epoxy cases.

Case-bond stresses in the row of elements in the case-bond liner next to the flap in the immediate vicinity of the flap termination are shown in Figure 39 for $P = 1.0$ psi. This stress distribution is virtually identical with the companion solution for thermal shrinkage loading shown in Figure 5. Lines of constant maximum principal strain are shown in Figure 40 for the immediate vicinity of the flap termination; gradients are almost identical with those for the corresponding shrinkage solution in Figure 11. Thus, there is little value in presenting more of the stress distributions for internal pressure loading since they are similar to those already presented for thermal shrinkage loading.

B. CASE HOOP EXPANSION COMPONENT OF LOADING

Stress/strain values already presented for thermal shrinkage loading can be interpreted as case expansion solutions for $\epsilon_\theta = \epsilon_z = \delta$ at the case-insulator interface. By obtaining additional stress solutions for a unit value of ϵ_θ of the case and a zero ϵ_z , the stresses for arbitrary combinations of ϵ_θ and ϵ_z can be derived. Key stresses for ϵ_θ case expansion loading of the cylinder with an 80-percent web fraction are presented in Table II. They are compared with the corresponding stresses for thermal shrinkage loads; however, the shrinkage stresses were reduced through division by a factor of 1.5. The 1.5 factor is based on the assumption that the cylinder stresses for a unit axial strain are equal to Poisson's ratio (~ 0.5) times those for a unit hoop strain. For thermal shrinkage loading, the axial and hoop strains were assumed to be equal at the case, considering shrinkage to be case expansion loading. Thus, stresses for hoop case expansion loading only should be two-thirds those for shrinkage loading. The comparison between the (reduced) shrinkage values and the hoop case expansion values is surprisingly good, with deviations generally less than 10 percent. The largest deviations occur for the centerport hoop stress and strain for $L/D = 1$ (14 percent), and

for ratios of the flap and saddle stresses to the mid-cylinder radial stress at the bond for $L/D = 5.0$ (16 percent). The critical propellant and bond stresses for case hoop expansion loading can be predicted with good accuracy from the thermal shrinkage solutions. Therefore, case hoop expansion solutions were not obtained for the other two web fractions.

C. PROCEDURE FOR PREDICTING PRESSURE SOLUTIONS FROM THERMAL SOLUTIONS

Stresses and strains for internal pressure loading can be predicted completely from corresponding values for thermal shrinkage loading. The procedure for predicting stress solutions for internal pressure loading is as follows:

- (1) Calculate axial and hoop strains for the case, without the grain:

$$\bar{\epsilon}_{\theta \text{ case}} = \frac{1}{E_{\theta}} \sigma_{\theta} - \frac{\nu_{\theta Z}}{E_{\theta}} \sigma_Z$$

$$\bar{\epsilon}_{Z \text{ case}} = \frac{\nu_{\theta Z}}{E_{\theta}} \sigma_{\theta} + \frac{1}{E_Z} \sigma_Z$$

$$\text{where } \sigma_{\theta} = \frac{Pb}{t_c} \text{ and } \sigma_Z = \frac{Pb}{2t_c}$$

- (2) Determine average case strains for coupled case and grain:

$$\begin{aligned} \bar{\epsilon}_{\theta \text{ case}} &= \frac{\left[1 - \nu_{\theta Z} \frac{H}{3} \left(\frac{\sigma_r}{E\delta} \right)_{\text{avg}} \right] \bar{\epsilon}_{\theta \text{ case}} - \left[\frac{H}{3} \left(\frac{\sigma_r}{E\delta} \right)_{\text{avg}} \right] \bar{\epsilon}_{Z \text{ case}}}{\left[1 - \nu_{\theta Z} \frac{H}{3} \left(\frac{\sigma_r}{E\delta} \right)_{\text{avg}} \right] \left[1 + \frac{2}{3} H \left(\frac{\sigma_r}{E\delta} \right)_{\text{avg}} \right] + \frac{2}{9} \nu_{\theta Z} H^2 \left(\frac{\sigma_r}{E\delta} \right)_{\text{avg}}^2} \\ \bar{\epsilon}_{Z \text{ case}} &= \frac{\bar{\epsilon}_Z + \left[\frac{2}{3} \nu_{\theta Z} H \left(\frac{\sigma_r}{E\delta} \right)_{\text{avg}} \right] \bar{\epsilon}_{\theta \text{ case}}}{1 - \frac{1}{3} \nu_{\theta Z} H \left(\frac{\sigma_r}{E\delta} \right)_{\text{avg}}} \end{aligned}$$

$$\text{where } H = \frac{Eb}{E_{\theta} t_c}, \text{ and } \left(\frac{\sigma_r}{E\delta} \right)_{\text{avg}} \text{ is obtained from Figure 37.}$$

(3) Calculate critical stresses and strains for pressure loading:

$$\sigma_{\text{pressure}} + P = E \left(\frac{2}{3} \epsilon_{\theta \text{ case}} + \frac{1}{3} \epsilon_{z \text{ case}} + \frac{P}{3K} \right) \left(\frac{\sigma}{E\delta} \right)_{\text{shrinkage}}$$

$$\epsilon_{\text{pressure}} = \left(\frac{2}{3} \epsilon_{\theta \text{ case}} + \frac{1}{3} \epsilon_{z \text{ case}} + \frac{P}{3K} \right) \left(\frac{\epsilon}{\delta} \right)_{\text{shrinkage}}$$

Note: Case strains for the empty case must apply for pressure, P.

This procedure will now be demonstrated for the cylinder with W/b = 0.8 and L/D = 3.0, considering an isotropic case.

(1) Empty case strains:

$$\sigma_{\theta} = \frac{Pb}{t_c} = \frac{(1.0)(16.05)}{0.1} = 160.5$$

$$\sigma_z = \frac{Pb}{2t_c} = 80.25$$

$$\bar{\epsilon}_{\theta} = \frac{1}{E_{\theta}} \sigma_{\theta} - \frac{\nu_{\theta z}}{E_0} \sigma_z = \frac{160.5}{4 \times 10^6} - \frac{0.1}{4 \times 10^6} (80.25) = 38.1 \times 10^{-6}$$

$$\bar{\epsilon}_z = -\frac{\nu_{\theta z}}{E_{\theta}} \sigma_{\theta} + \frac{1}{E_z} \sigma_z = -\frac{0.1}{4 \times 10^6} (160.5) + \frac{80.25}{4 \times 10^6} = 16.04 \times 10^{-6}$$

(2) Case strains considering grain reinforcement:

$$H = \frac{Eb}{E_{\theta} t_c} = \frac{(200)(16)}{(4 \times 10^6)(0.1)} = 0.0080$$

$$\left(\frac{\sigma_r}{E\delta} \right)_{\text{average}} = 11.2$$

$$\frac{H}{3} \left(\frac{\sigma_r}{F\delta} \right)_{\text{average}} = 0.0298$$

$$\epsilon_{\theta \text{ case}} = \frac{\left[1 - (0.1)(0.0298) \right] (38.1 \times 10^{-6}) - (0.0298)(16.04 \times 10^{-6})}{\left[1 - (0.1)(0.0298) \right] (1 + 0.0596) + (2) (0.1) (0.0298)^2}$$

$$= 35.6 \times 10^{-6}$$

$$\epsilon_{z \text{ case}} = \frac{16.04 \times 10^{-6} + (2) (0.0298) (35.6 \times 10^{-6})}{1 - 0.1 (0.0298)} = 18.2 \times 10^{-6}$$

(3) Calculate critical stresses and strains:

$$(\sigma_{\theta} + P)_{\text{bore}} = 200 \left[(0.667)(35.6 \times 10^{-6}) + (0.333)(18.2 \times 10^{-6}) + 1 \times 10^{-6} \right] (32.6) = 0.201$$

$$(\sigma_{\text{max}} + P)_{\text{flap}} = 200 (30.8 \times 10^{-6}) (33.0) = 0.203$$

$$(\epsilon_{\theta})_{\text{bore}} = (30.8 \times 10^{-6}) (24.9) = 0.00077$$

A finite-element solution, obtained directly for internal pressure loading, correlated with the above prediction as follows:

<u>Stress Parameter</u>	<u>Pressure Loading Result</u>	<u>Predicted Value from Thermal Solution</u>	<u>Error (percent)</u>
$(\sigma_{\theta} + P)_{\text{bore}}$	0.191	0.201	+5.2
$(\sigma_{\text{max}} + P)_{\text{flap}}$	0.200	0.203	+1.5
$(\epsilon_{\theta})_{\text{bore}}$	0.0074	0.00077	+3.5

The maximum error of 5.2 percent occurs in the centerport hoop stress. In all cases, the thermal prediction is high. The predicted case hoop strain of 35.6×10^{-6} compares with pressure loading results of 35.7×10^{-6} at the flap termination, 36.6×10^{-6} at the saddle (maximum case hoop strain), and 34.5×10^{-6} at the mid-cylinder; the predicted case axial strain of 18.2×10^{-6} compares with pressure loading results of 16.6×10^{-6} at the flap termination, 16.1 at the saddle, and 15.0×10^{-6} at the mid-cylinder. Thus, the average hoop strain in the case compares quite well with the prediction, while the predicted axial strain is too high. Omission of the bond shear stress in the grain-case coupling equations is probably to blame for the high axial strain prediction. Overall, the directly calculated pressure solution compares very favorably with the prediction based on thermal shrinkage loading.

SECTION VII

RESULTS FOR AXIAL ACCELERATION LOADING

Stress solutions for axial acceleration loading were obtained with the case considered to be rigid. The propellant, liner, flap, and insulator were given the same weight density, $\rho_w = 0.064 \text{ lb/in.}^3$ and subjected to a 1.0 g axial acceleration. Stress solutions were obtained only for $E_{\text{insulator}} = E_{\text{flap}} = 1000 \text{ psi}$ and $E_{\text{liner}} = E_{\text{propellant}} = 200 \text{ psi}$. The flap length was 1.0 in.

Calculated radial and shear stresses for the cylinder with $L/D = 3.0$ and $W/b = 0.8$ are shown in Figure 41 for the row of elements in the case-bond liner next to the flap. The center of this element row is located 0.105 in. inboard of the insulator (0.005 in. into the liner). The shear stress reaches an average value of -0.50 psi at the mid-axial location ($Z = 48 \text{ in.}$). Near the flap termination the shear stress has a negative peak of -0.68 psi and a positive peak of 0.23 psi. The peak radial stress at the flap termination, 3.4 psi, is much higher than the shear stress. Both the low value of the peak shear stress and the high value of the peak radial stress, are somewhat surprising. Currently-used handbook methods for approximating stresses at the bond termination assume that the peak shear stress is 3.0 times the average shear stress.¹⁰ In the sample given here, the calculated concentration factor for the peak shear stress is only 1.4. However, the peak radial stress is 4.3 times the average shear stress.

Stress values in the immediate vicinity of the flap termination are shown in Figure 42. The shear stress and maximum principal strain approach their average values to the right of the flap termination rather than approaching zero, as in the thermal solution.

Lines of constant maximum principal stress and strain in the vicinity of the flap termination are shown in Figures 43 and 44, respectively. The stress values are normalized in terms of $(\tau_{rz})_{\text{avg}}$ and the strain values are shown in terms of $\frac{E \epsilon_{\text{max}}}{(\tau_{rz})_{\text{avg}}}$ (a bond length of 94.0 in. and a radial distance of 15.895 in. were used in calculating the average shear stress). The stress values indicate a high stress concentration at the flap-insulator bond termination as expected. The overall gradient is similar to that for thermal shrinkage loading. This similarity holds quantitatively, as shown in Figure 45, wherein the ratio of the maximum principal stress inside of the liner/propellant to that at the liner-flap bondline (H_p) decreases almost identical to that for shrinkage loading. Lines of constant maximum principal strain are essentially the same for axial acceleration and thermal shrinkage loading, as shown in Figures 7 and 44.

Finite-element stress solutions were obtained for $W/b = 0.5, 0.67,$ and 0.8 for the cylinder with $L/D = 3.0$. Computed results for the critical stresses at the flap termination are shown in Figure 46. The peak stresses, when normalized with respect to the average case-bond shear stress, are essentially independent of web fraction. The peak value of the maximum principal stress (for a unit value of H_G) is approximately equal to 4.6 times the average bond shear stress; whereas, peak value for the radial stress is approximately 4.4 times the average bond shear stress. The peak value of the bond shear stress is approximately 1.4 times the average bond shear stress. The shear stress at the location of the peak radial stress is only 0.17 times as large as the peak radial stress.

Finite-element stress solutions for $W/b = 0.8$ were obtained for $L/D = 1.0, 3.0,$ and 5.0 . The key stresses at the flap termination are shown in Figure 47 as a function of L/D . These critical (normalized) stress parameters are essentially independent of length-to-diameter ratio, as well as web fraction. Values for $L/D = 1.0$ are only 7 percent higher than those for $L/D = 3.0$ and 5.0 . One would anticipate higher stresses relative to the average for shorter cylinders; however, dependence upon L/D is very moderate for values 1.0 and greater.

It appears that the normalized bond termination stresses for axial acceleration loading are basically dependent upon the local flap termination geometry and are independent of L/D and W/b . In this regard, the cylinder behavior is much different than for thermal shrinkage and internal pressure loadings. The peak bond stresses for axial acceleration are sensitive to flap-liner thickness in the same quantitative manner as for thermal shrinkage and internal pressure loadings. No study was performed for variations in flap length or liner-flap-insulator modulus. However, since the same stress-strain patterns exist near the flap termination for all three loading conditions, it is expected that variations for thermal shrinkage loading are representative of axial acceleration loading as well.

SECTION VIII

SUMMARY AND CONCLUSIONS

The important results and conclusions obtained from the parameter study are as follows:

- (1) Case-bond stresses for thermal shrinkage and internal pressure loading become larger as web fraction and length-to-diameter ratio increase. However, as L/D and W/b increase, the end termination stresses decrease relative to the centerport hoop stress and the radial bond stress at the mid-cylinder location.
- (2) Case-bond stress distributions at flap terminations are a function of the local geometry only and are relatively insensitive to changes in W/b and L/D for the loadings studied.
- (3) Modest changes in flap and case-bond liner stiffness have little effect on local case-bond stress levels.
- (4) Flap length is a less significant factor than flap thickness in determining stresses at the flap terminations.
- (5) Case-bond and propellant stresses can be predicted quite accurately for internal pressure loading using thermal shrinkage solutions.
- (6) The case-bond radial stress at flap terminations is much larger than the shear stress under axial acceleration loading, as well as under thermal shrinkage and internal pressure loading.
- (7) Flap termination stresses relative to the average case-bond shear stress are insensitive to L/D and W/b for axial acceleration loading.

REFERENCES

1. Durelli, A. J., et al., "Study of Stress Concentrations at the Ends of Solid Propellant Grains Subjected to Restrained Shrinkage," Catholic University Final Report, Contract No. AF-04(611)-10378, May 1966.
2. Messner, A. M., and Schiessmann, D., "Parameter Calculation of Simple Propellant Grains for Temperature Cycling, Pressurization, and Acceleration," Appendix D, Study of Mechanical Properties of Solid Propellants, Aerojet-General Report No. 0411-10F, March 1962, and Lockheed Propulsion Company Structures Manual, December 1969.
3. Shearly, R. N., and Messner, A. M., "Stresses in Propellant Grain Bond Systems," Bulletin of the 3rd Meeting ICRPG Working Group on Mechanical Behavior, CPIA Publication No. 61V, Vol. I, October 1964.
4. Noel, J. S., and Webb, L. D., "The Role of Fracture Mechanics in the Design of Optimum Grain-Case Terminations," Bulletin of the 5th Meeting ICRPG Working Group on Mechanical Behavior, CPIA Publication No. 119, Vol. I, October 1966.
5. Becker, E. B., and Brisbane, J. J., "Application of the Finite Element Method to Stress Analysis of Solid Propellant Rocket Grains," Rohm & Haas Report No. S-76, November 1965.
6. Bridgeman, P. W., "The Compression of 46 Substances to 50,000 kg/cm³," 8 November 1930.
7. Jones, J. W., "Engineering Methods for Grain Structural Integrity Analysis," LPC Report No. 578/556-F-3, Lockheed Propulsion Company, Redlands, California, May 1963.
8. Parr, C. H., "Deformations and Stresses in a Case-Bonded Solid Propellant Grain of Finite Length by Numerical Methods," Rohm & Haas Quarterly Progress Report on Engineering Research, Report No. P-61-17, 25 June 1962.
9. Holsapple, K. A., Schmidt, W. F., and Fourny, M. E., "Some Pressure-Temperature Equivalences in Elasticity, with Applications to Case-Bonded Solid Propellant Rocket Grains," Journal of Applied Mechanics, Vol. 37, No. 4, December 1970.
10. Fitzgerald, J. E., and Hufferd, W. L., "Handbook for the Engineering Structural Analysis of Solid Propellants," CPIA Publications 214, May 1971.

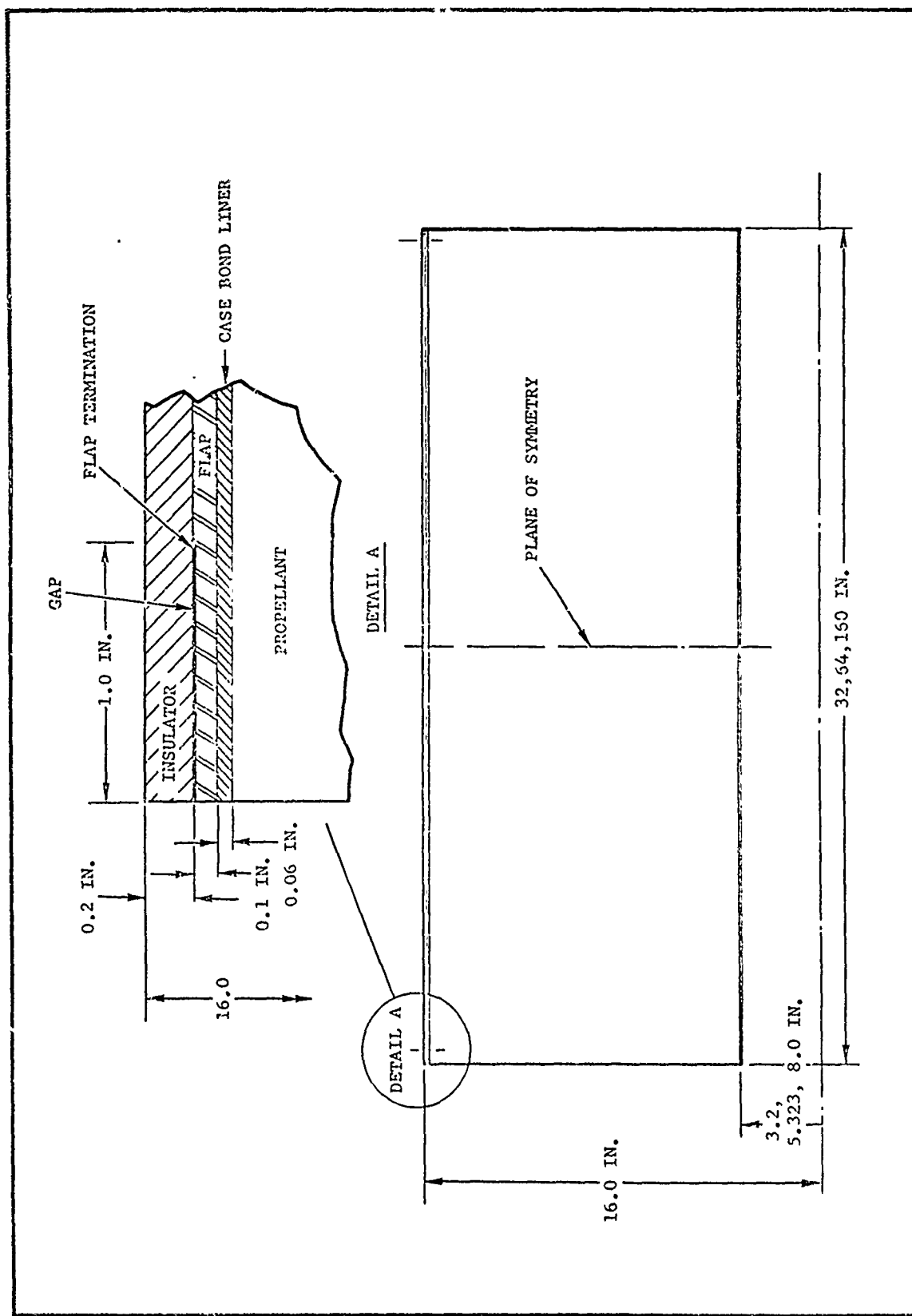


Figure 1. Cylinder Model for Flap Termination Studies

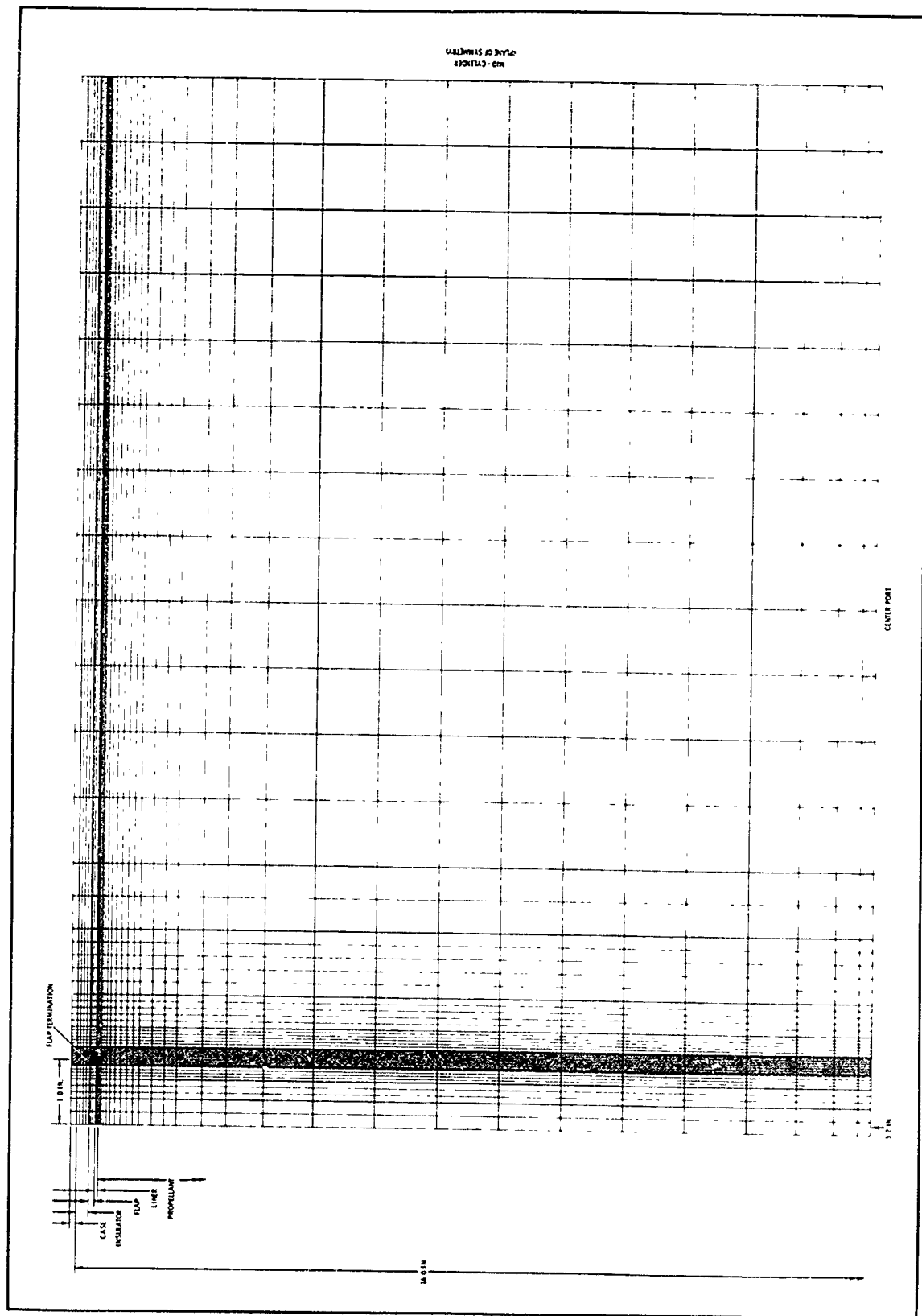


Figure 2. Finite Element Model for Cylinder with $L/D = 1.0$ and $W/b = 0.8$

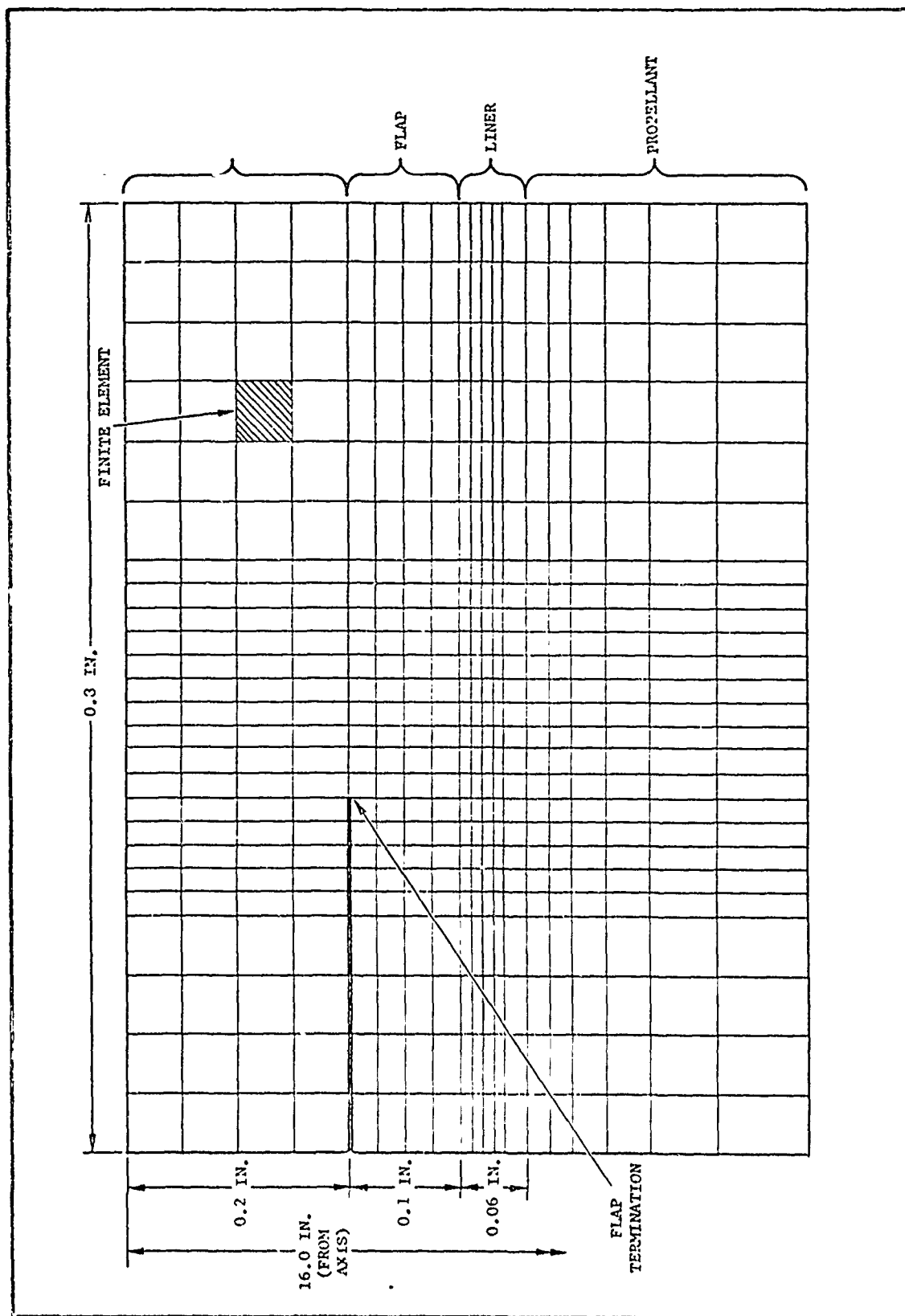


Figure 3. Finite Element Grid Detail Adjacent to Flap Termination

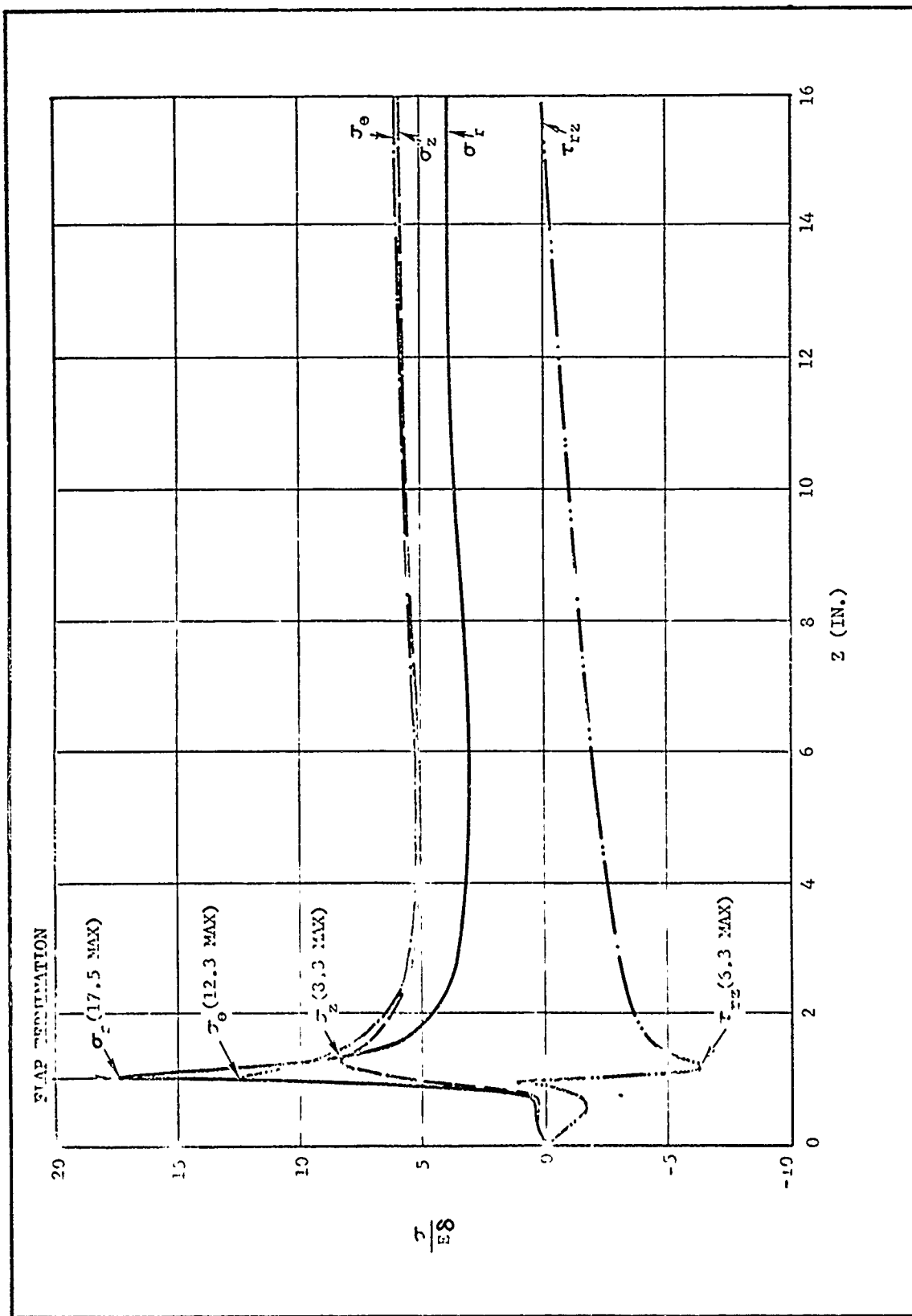


Figure 4. Case Bond Liner Stresses for a Cylinder with $L/D = 1.0$ and $W/b = 0.8$ Under Thermal Shrinkage Loading

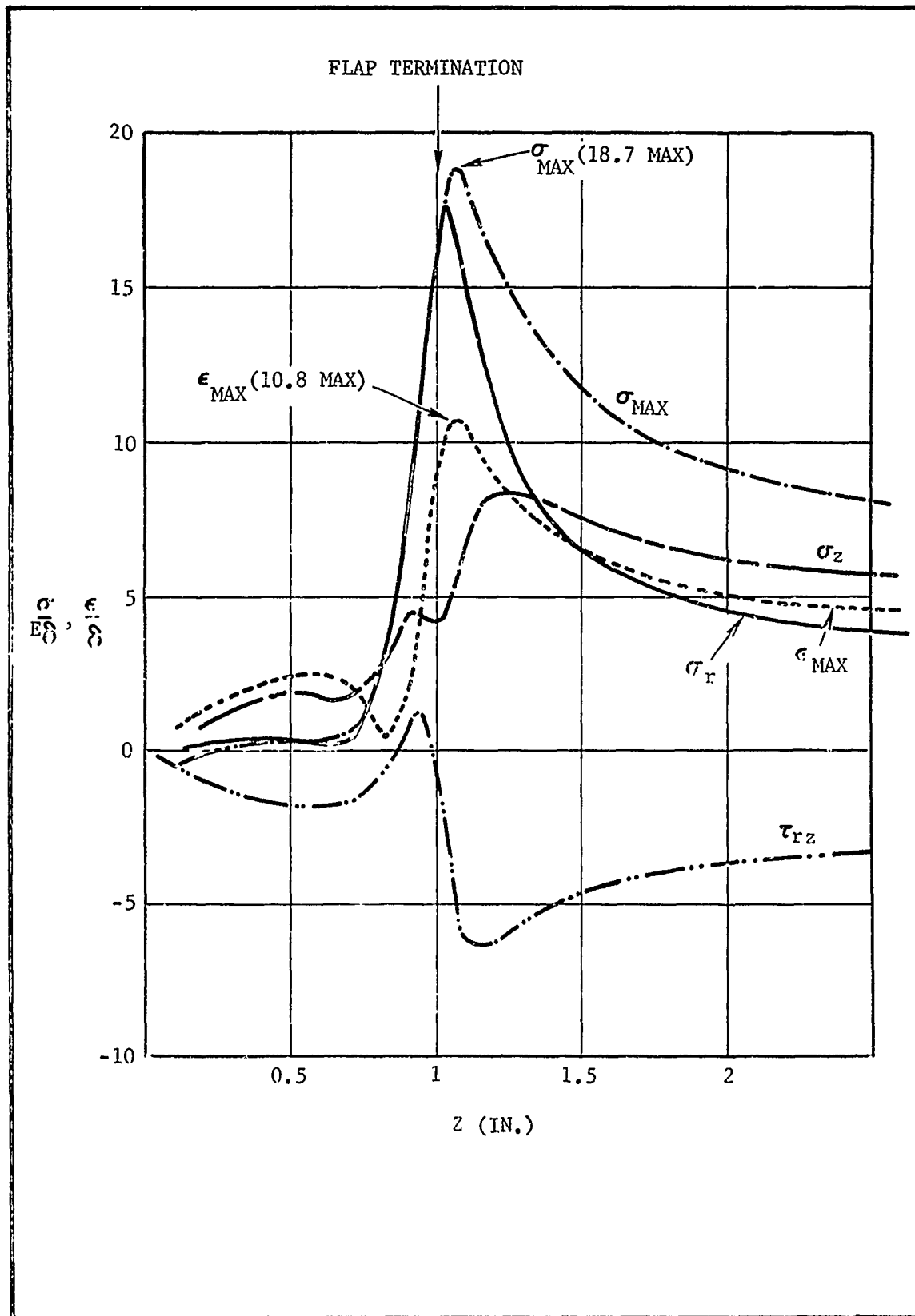


Figure 5. Case Bond Liner Stresses Near the Flap Termination for a Cylinder with $L/D = 1.0$ and $W/b = 0.8$ Under Thermal Shrinkage Loading

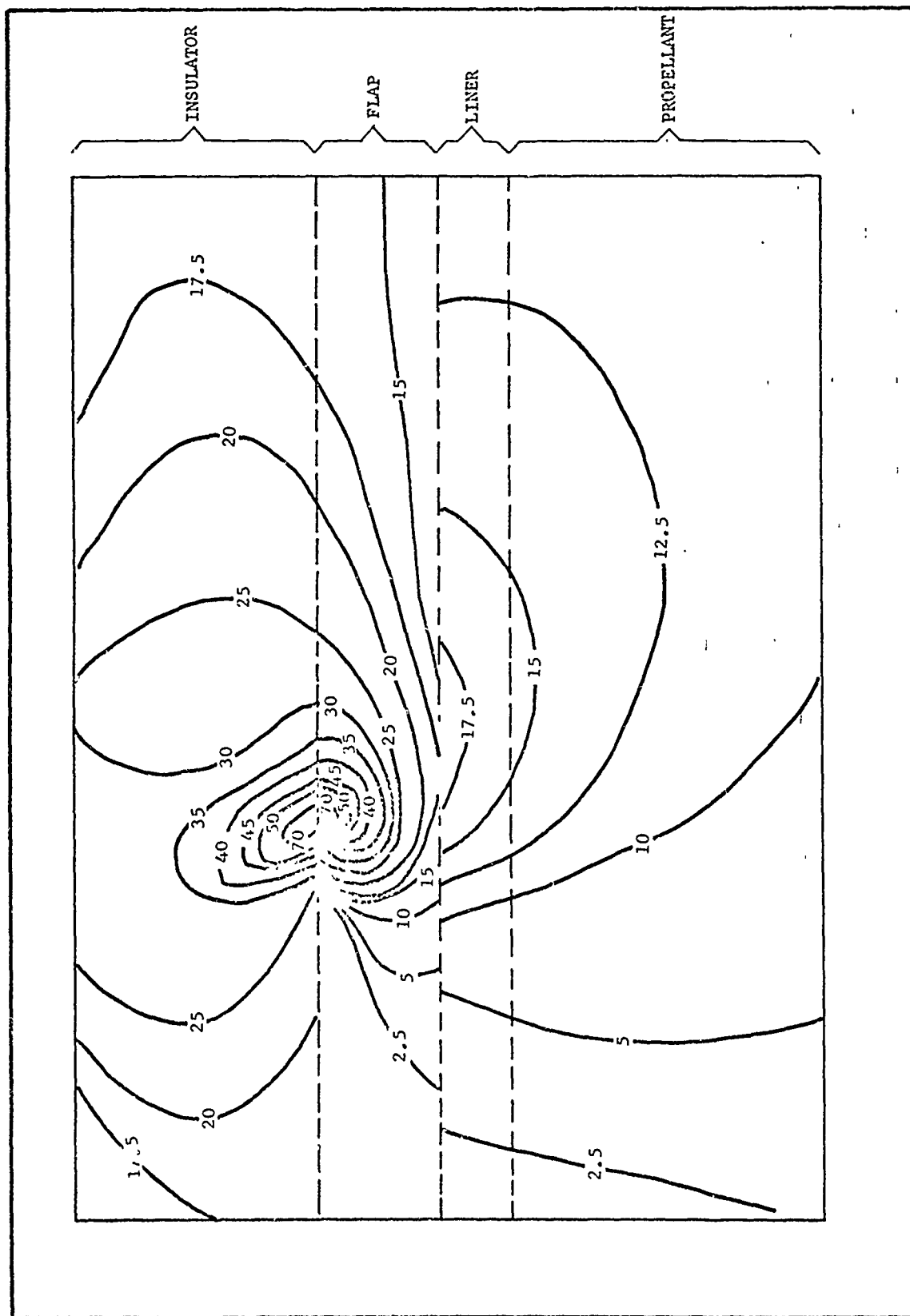


Figure 6. Lines of Constant Maximum Principal Stress $\left(\frac{\sigma_{\max}}{E\delta}\right)$ in the Vicinity of the Flap Termination for a Cylinder with $L/D = 1.0$ and $W/b = 0.8$ Under Thermal Shrinkage Loading

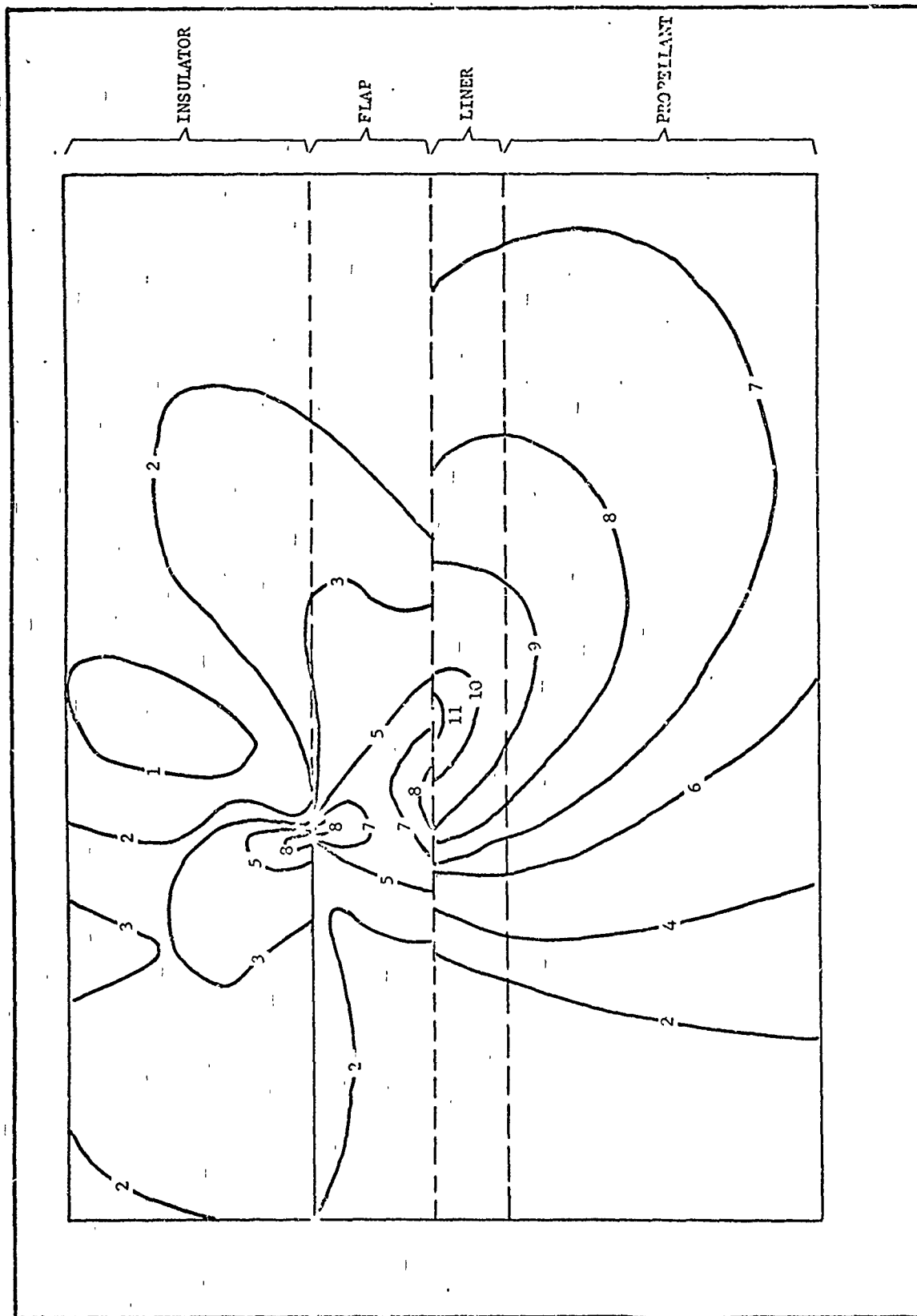


Figure 7. Lines of Constant Maximum Principal Strain $\left(\frac{\epsilon_{\max}}{2}\right)$ in the Vicinity of the Flap Termination for a Cylinder with $L/D = 1.0$ and $t/b = 0.8$ Under Thermal Shrinkage Loading

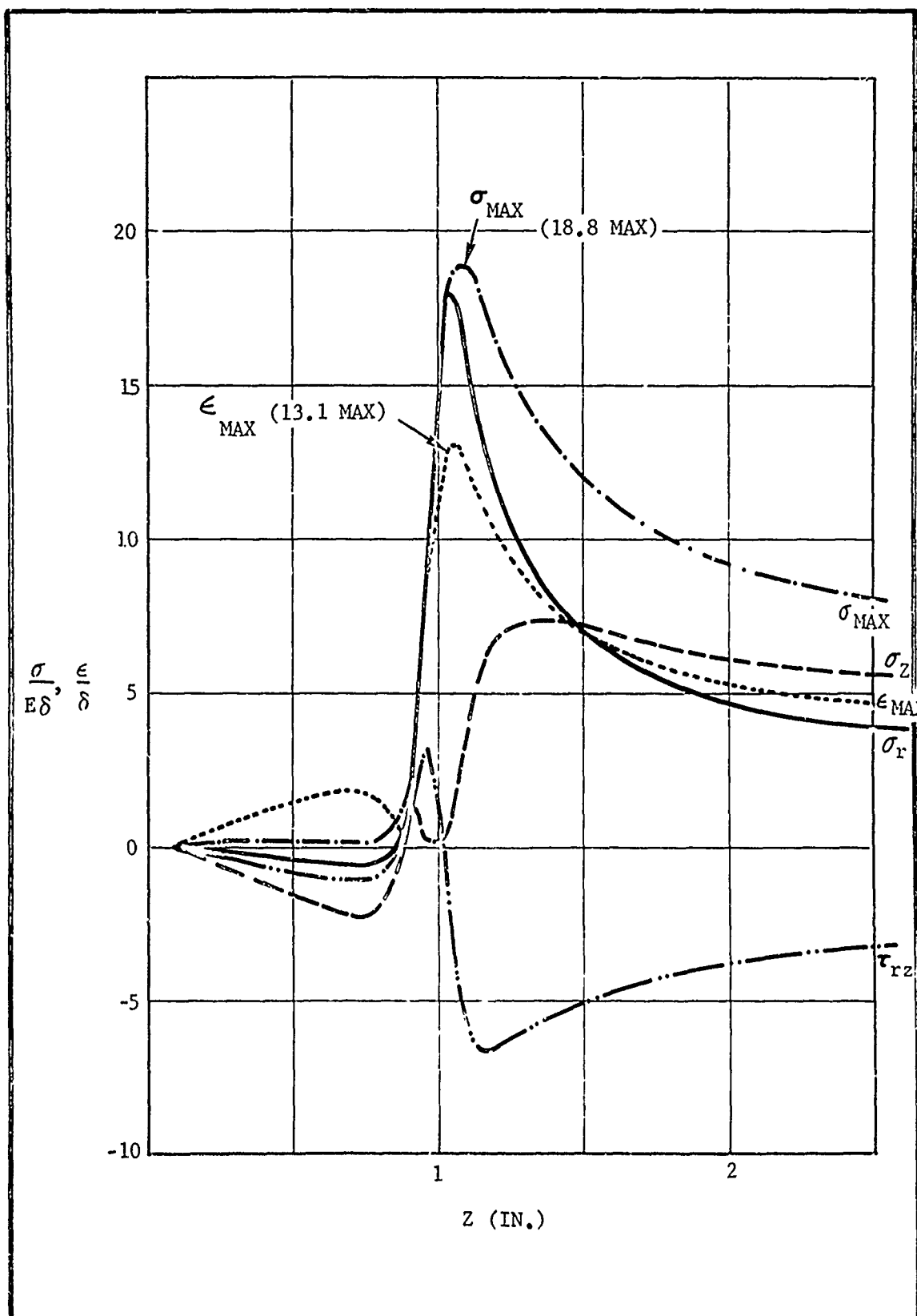


Figure 8. Case Bond Liner Stresses Near the Flap Termination for a Cylinder with $L/D = 1.0$ and $W/b = 0.8$ ($E_{flap} = 200$ psi) Under Thermal Shrinkage Loading

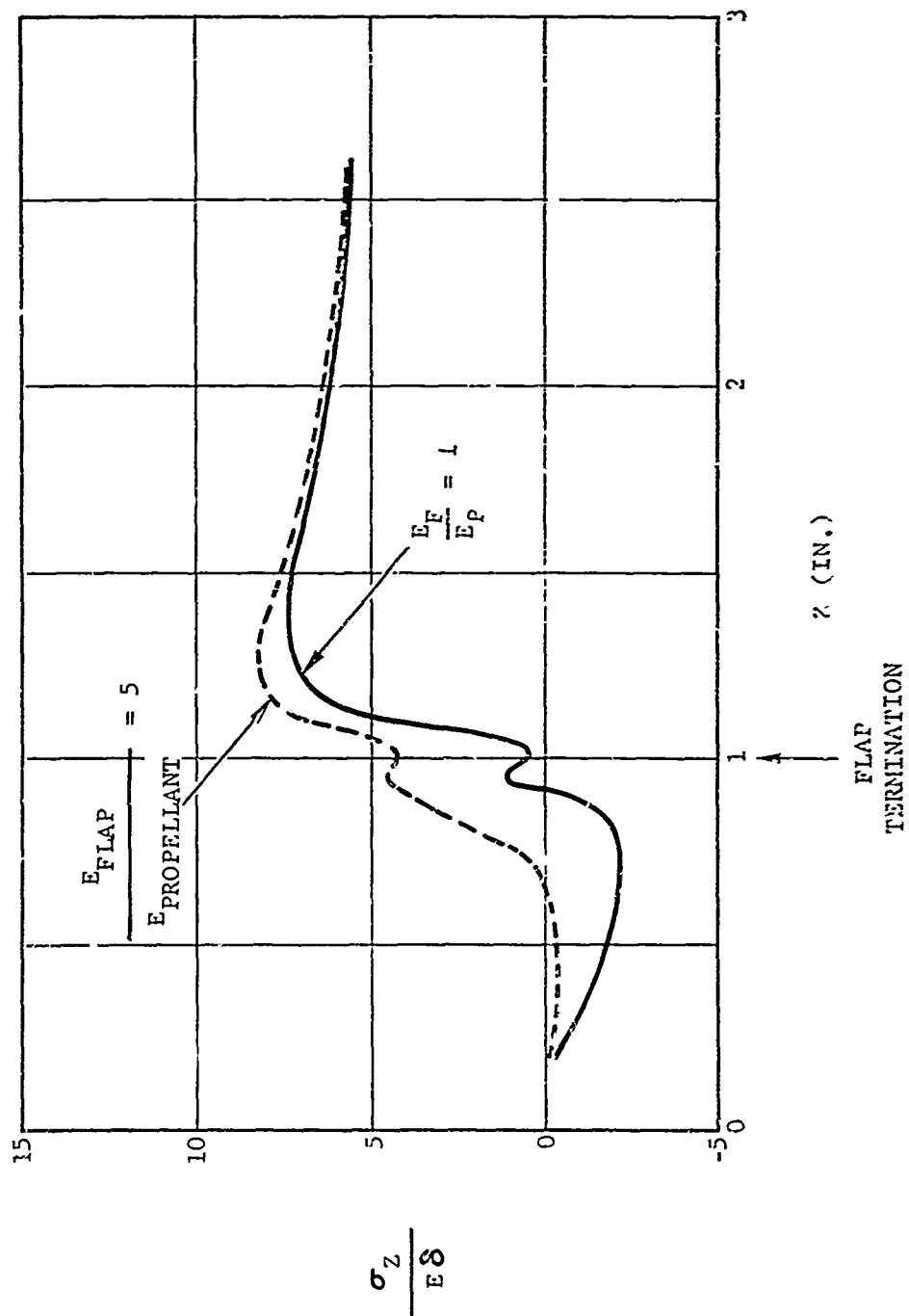


Figure 9. Case Bond Axial Stresses in the Liner Near the Flap Termination for a Cylinder with $L/D = 1.0$ and $v/b = 0.8$ Under Thermal Shrinkage Loading

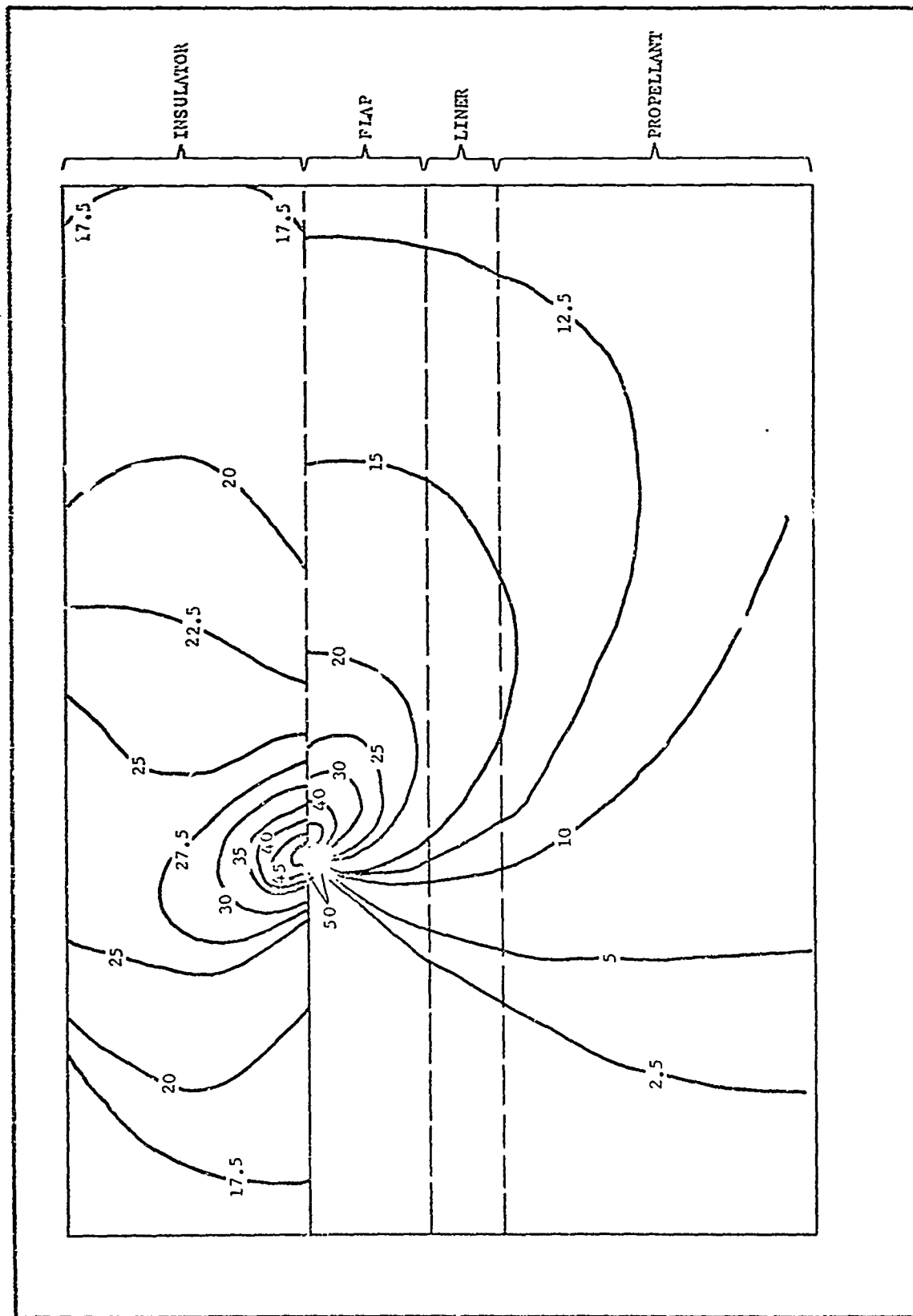


Figure 10. Lines of Constant Maximum Principal Stress $\left(\frac{\sigma_{\max}}{E\delta}\right)$ in the Vicinity of the Flap Termination for a Cylinder with $L/D = 1.0$ and $W/b = 0.8$ ($E_{\text{flap}} = 200$ psi) Under Thermal Shrinkage Loading

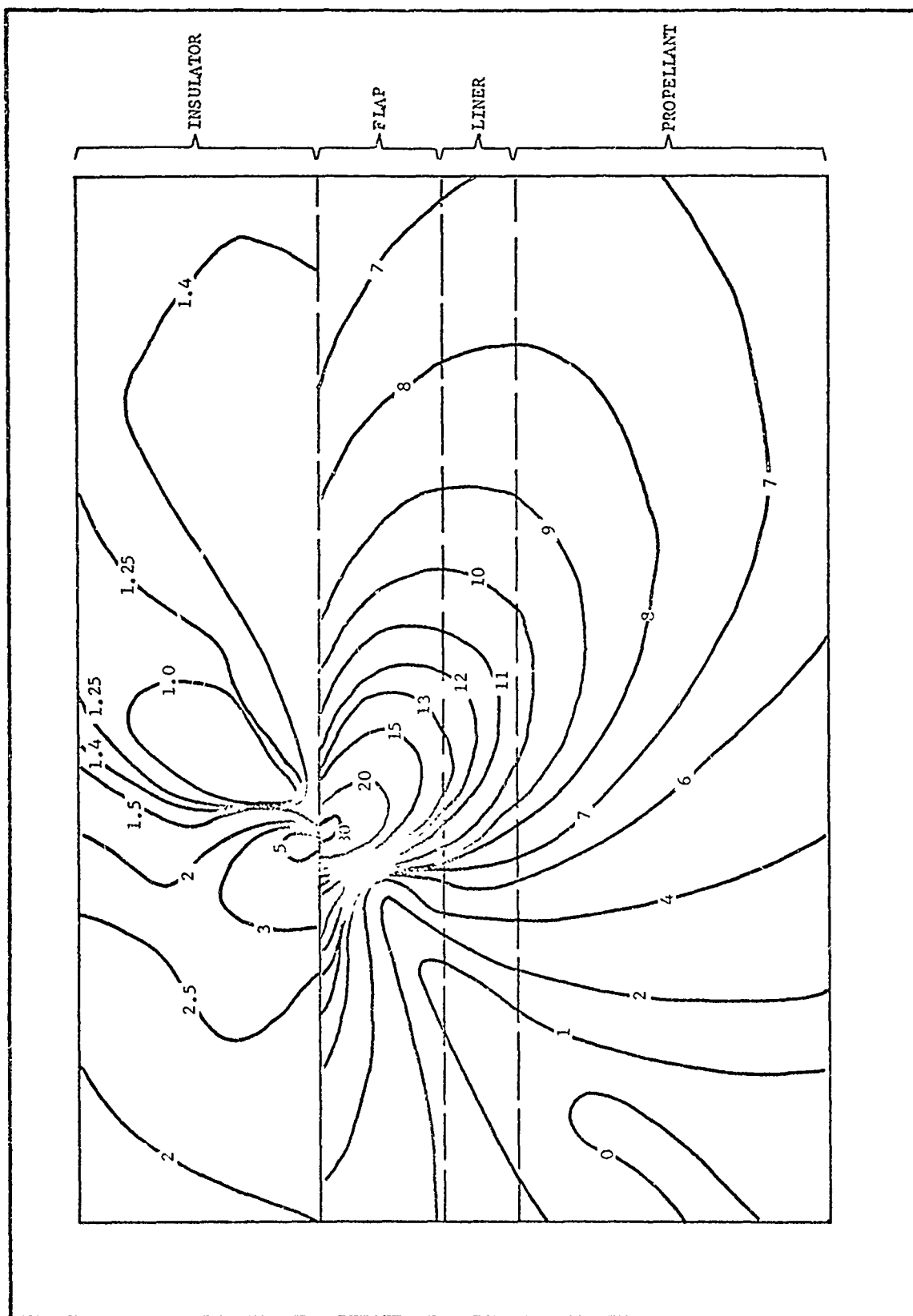


Figure 11. Lines of Constant Maximum Principal Strain $\left(\frac{\epsilon_{\max}}{\delta}\right)$ in the vicinity of the Flap Termination for a Cylinder with $L/D = 1.0$ and $W/b = 0.8$ ($E_{\text{flap}} = 200$) Under Thermal Shrinkage Loading

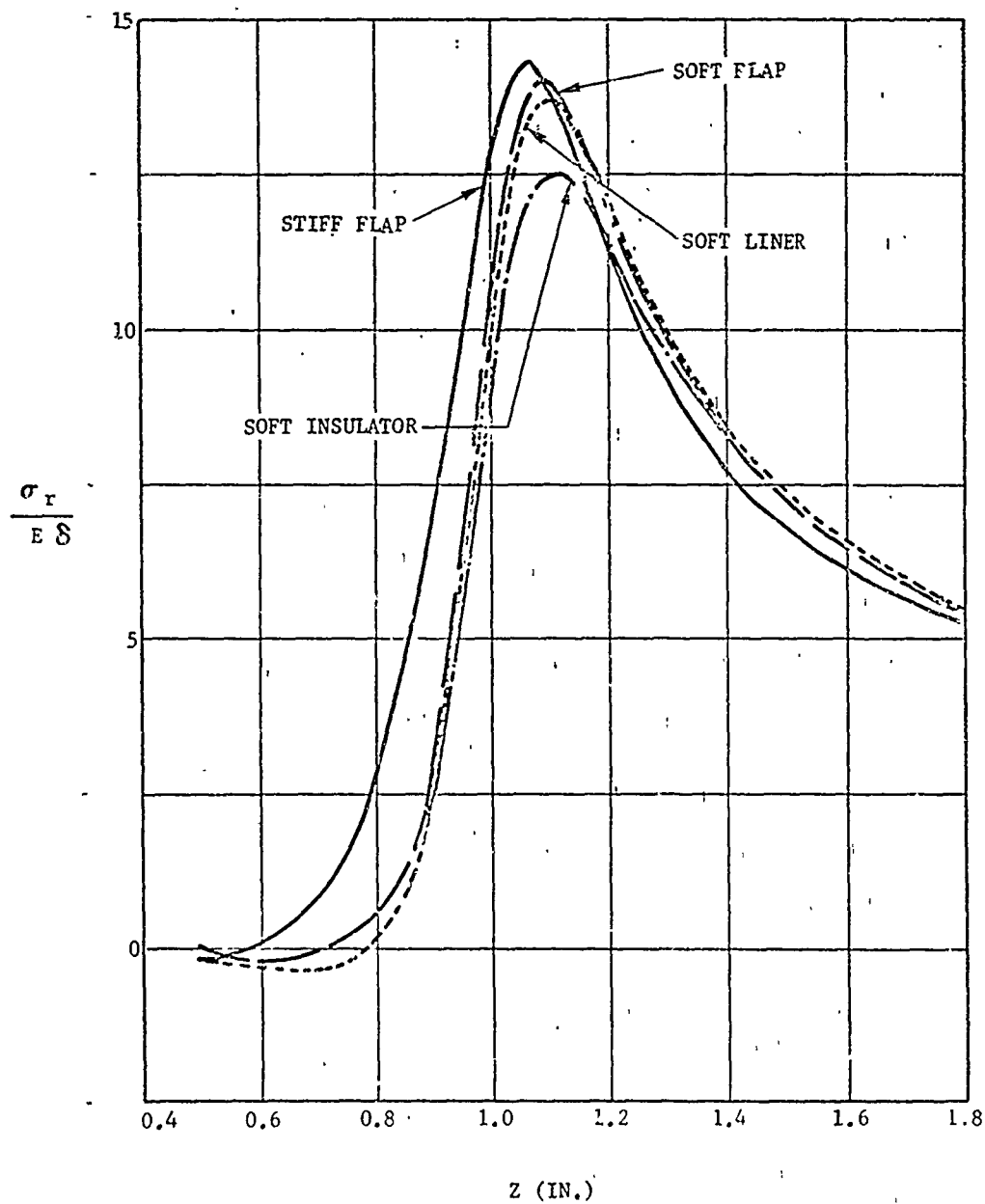


Figure 12. Propellant Radial Stresses at the Propellant-to-Liner Bond Adjacent to the Flap Termination for a Cylinder with $L/D = 1.0$ and $W/b = 0.8$ Under Thermal Shrinkage Loading

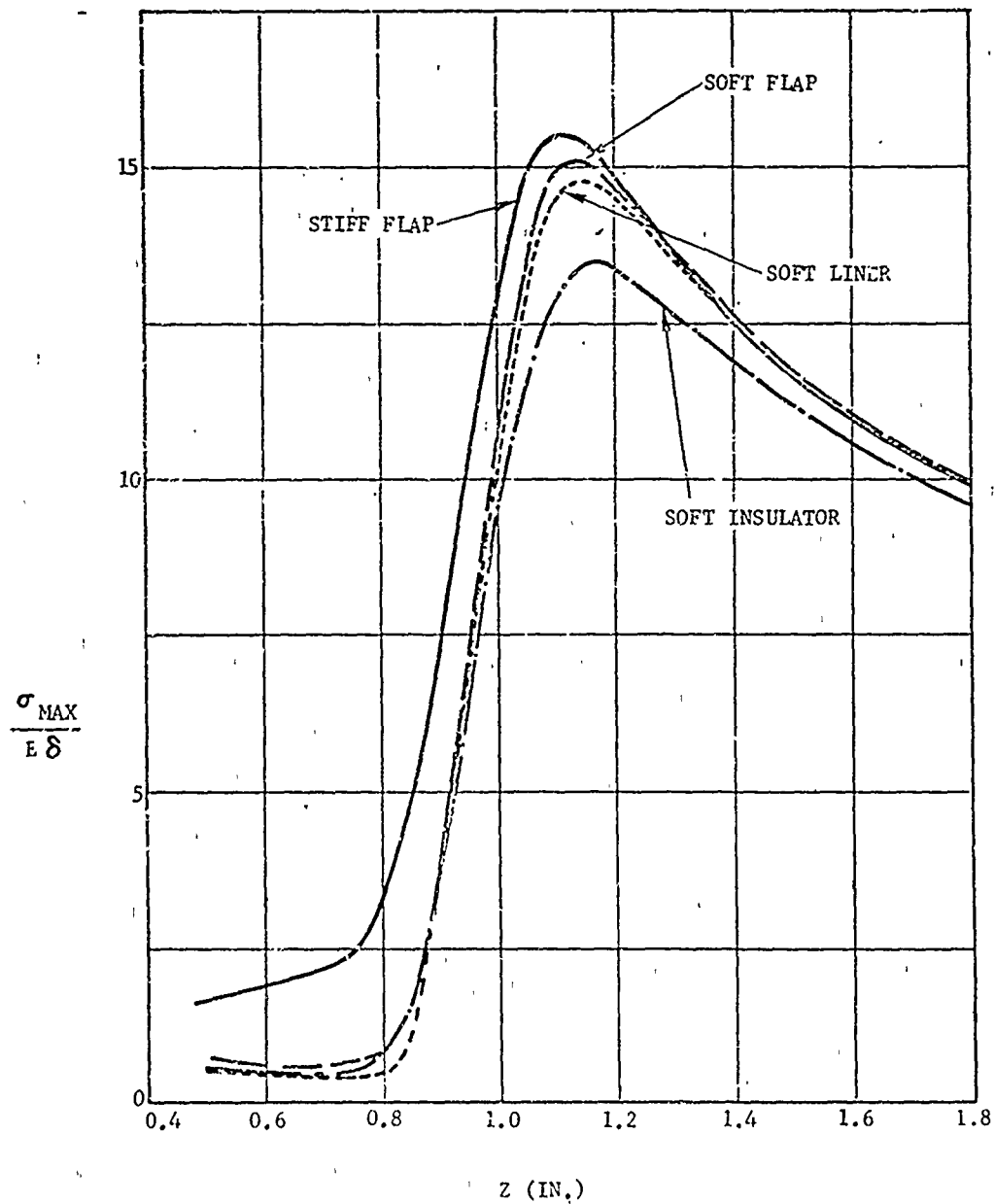


Figure 13. Propellant Maximum Principal Stresses at the Propellant-to-Liner Bond Adjacent to the Flap Termination for a Cylinder with $L/D = 1.0$ and $W/b = 0.8$ Under Thermal Shrinkage Loading

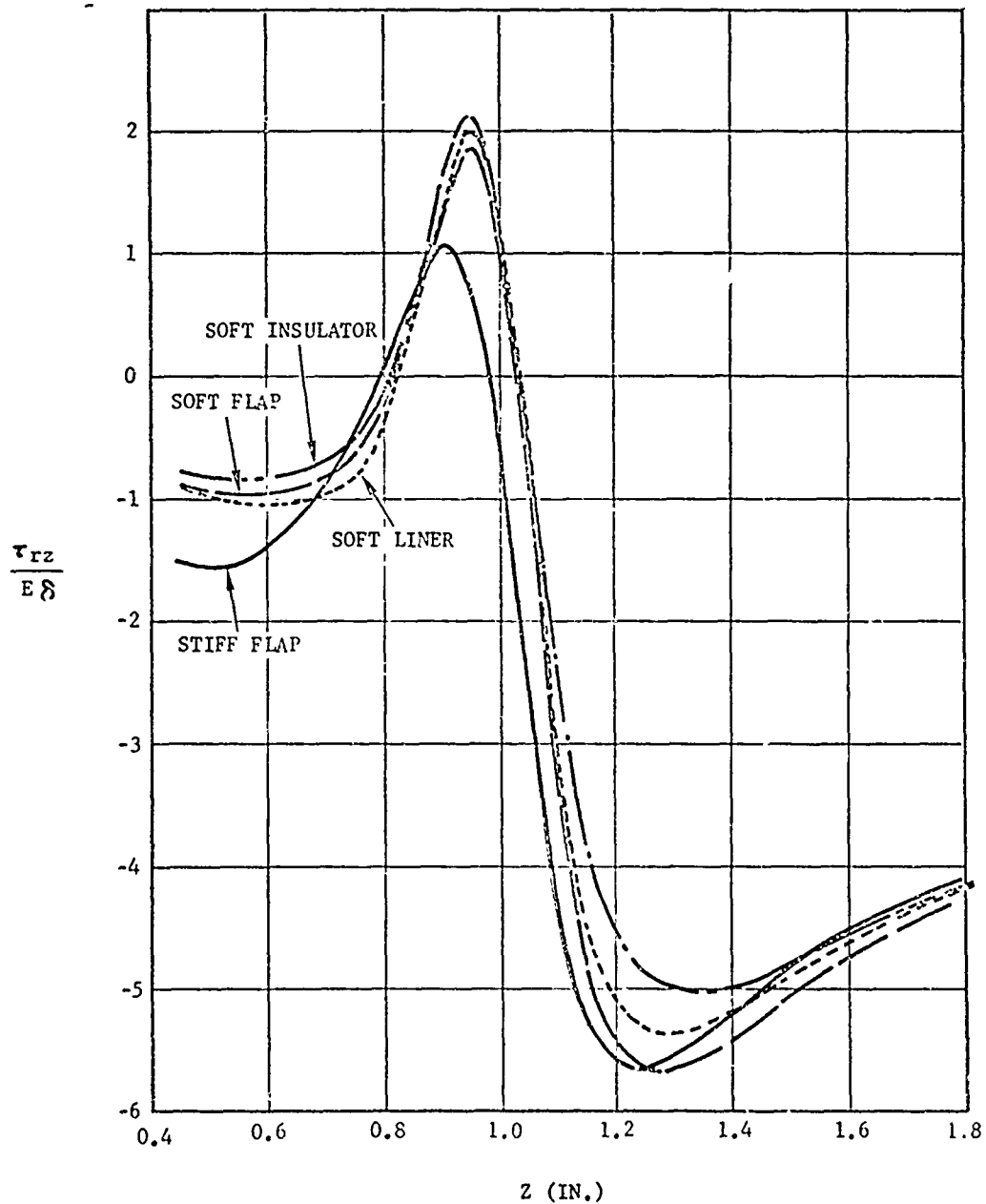


Figure 14. Propellant Shear Stresses at the Propellant-to-Liner Bond Adjacent to the Flap Termination for a Cylinder with $L/D = 1.0$ and $W/b = 0.8$ Under Thermal Shrinkage Loading

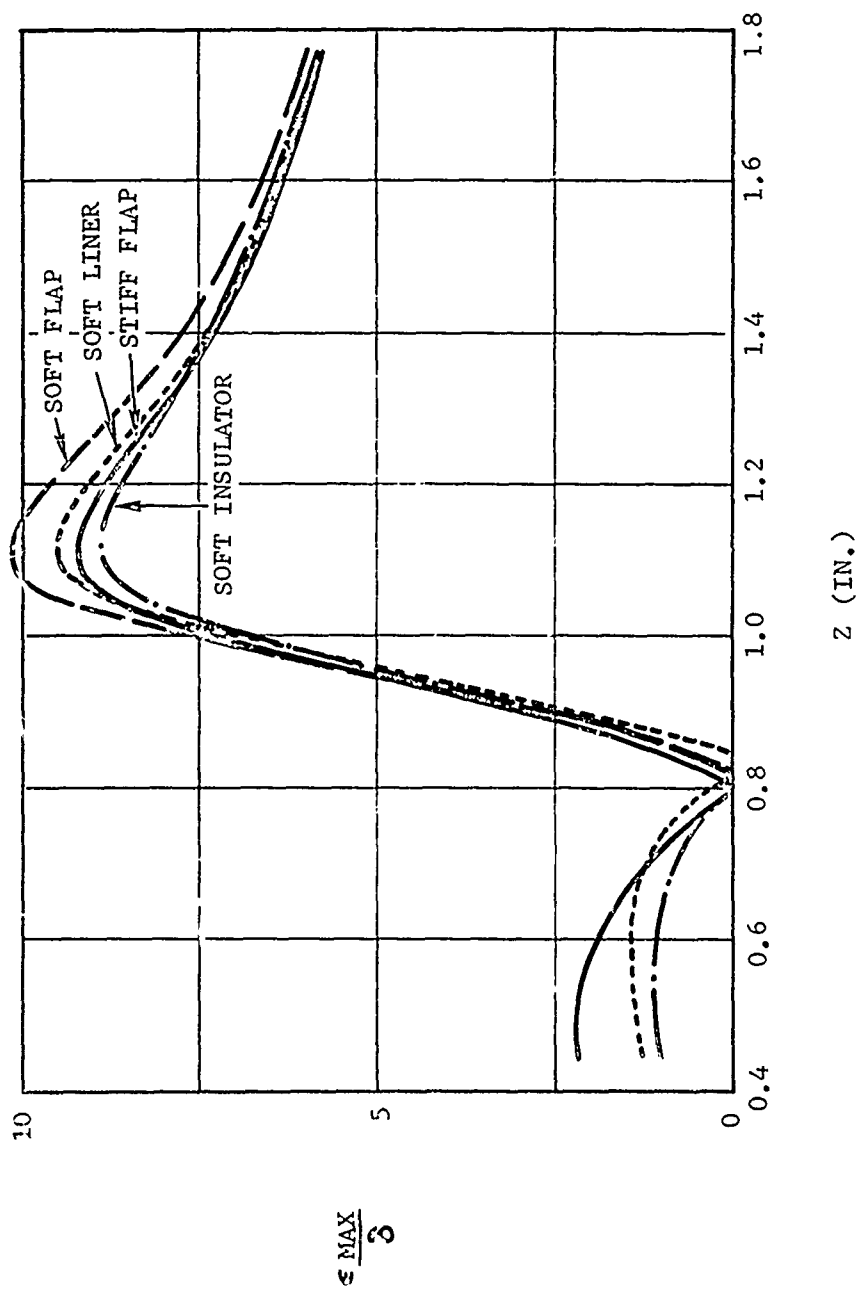


Figure 15. Propellant Maximum Principal Strains at the Propellant-to-Liner Bond Adjacent to the Flap Termination for a Cylinder with $L/D = 1.0$ and $w/b = 0.8$ Under Thermal Shrinkage Loading

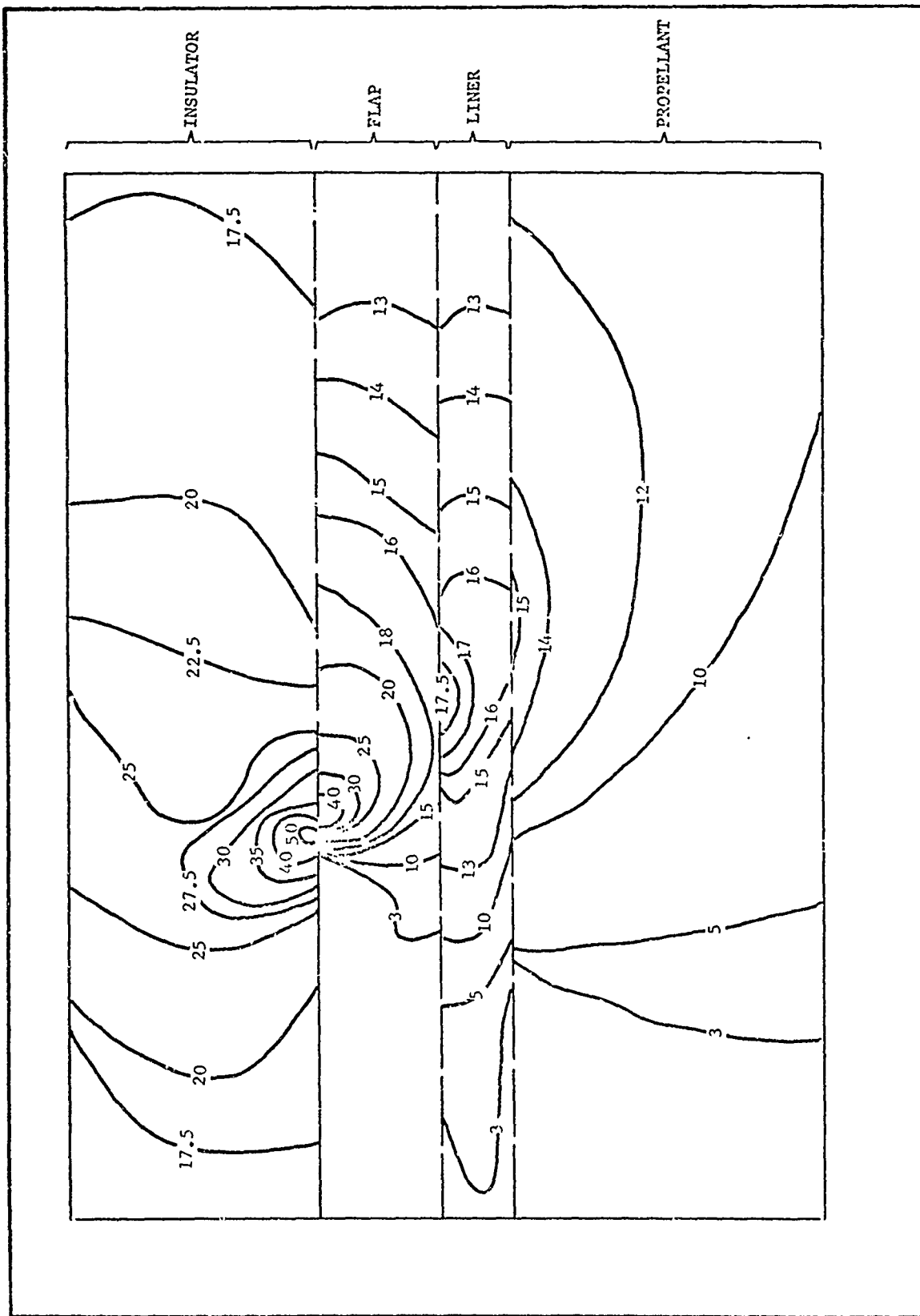


Figure 16. Lines of Constant Maximum Principal Stress $\left(\frac{\sigma_{\max}}{E\delta}\right)$ in the Vicinity of the Flap Termination for a Cylinder with $L/D = 1.0$ and $W/b = 0.8$ ($E_{\text{flap}} = 200$ psi, $E_{\text{liner}} = 100$ psi) Under Thermal Shrinkage Loading

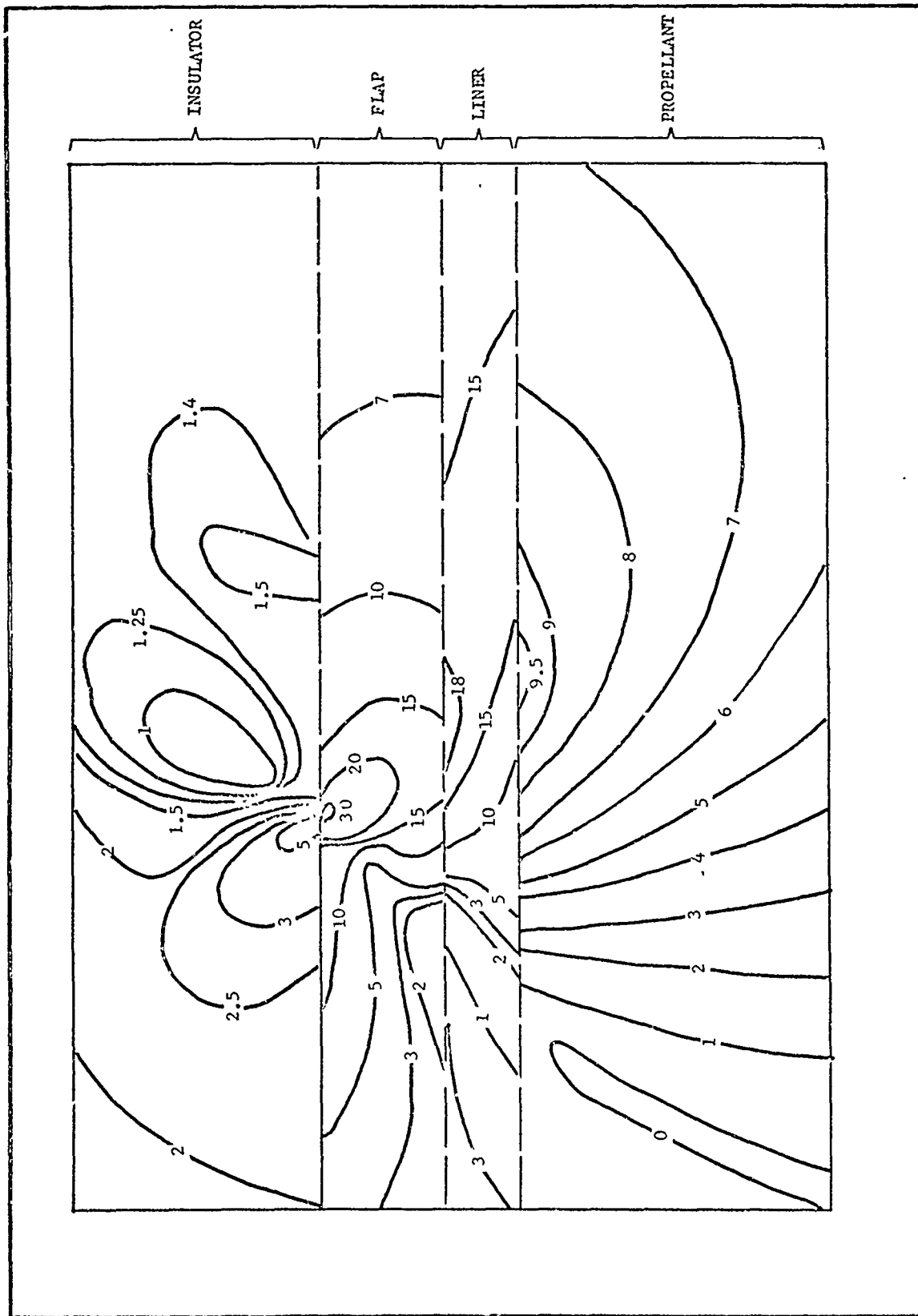


Figure 17. Lines of Constant Maximum Principal Strain $\left(\frac{\epsilon_{\max}}{8}\right)$ in the Vicinity of the Flap Termination for a Cylinder with $L/D = 1.0$ and $W/b = 0.8$ ($E_{\text{flap}} = 200 \text{ psi}$, $E_{\text{liner}} = 100 \text{ psi}$) Under Thermal Shrinkage Loading

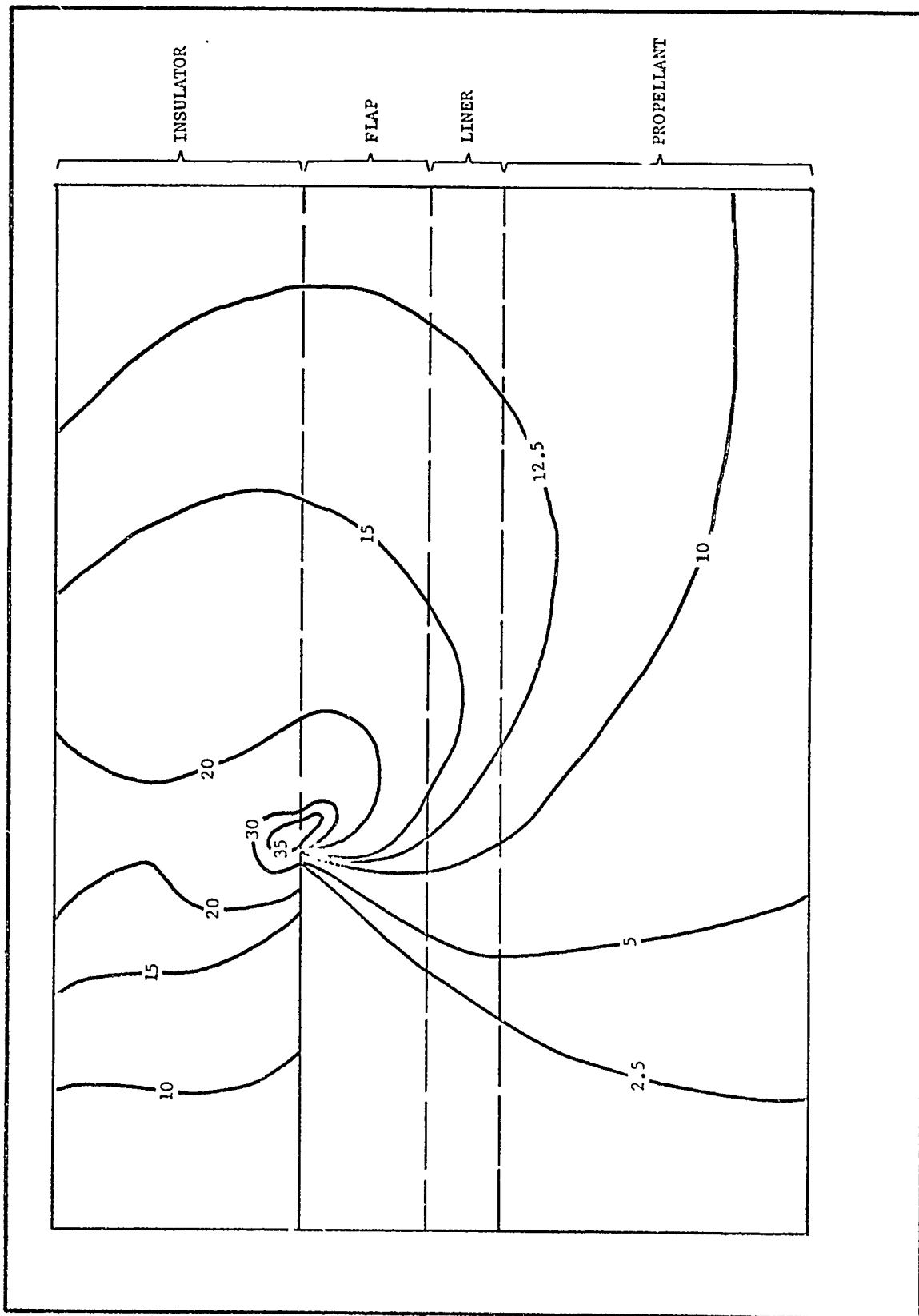


Figure 18. Lines of Constant Maximum Principal Stress $\left(\frac{\sigma_{\max}}{E\delta}\right)$ in the Vicinity of the Flap Termination for a Cylinder with $L/D = 1.0$ and $W/b = 0.8$
 $(E_{\text{flap}} = E_{\text{insulator}} = E_{\text{liner}} = 200 \text{ psi})$ Under Thermal Shrinkage Loading

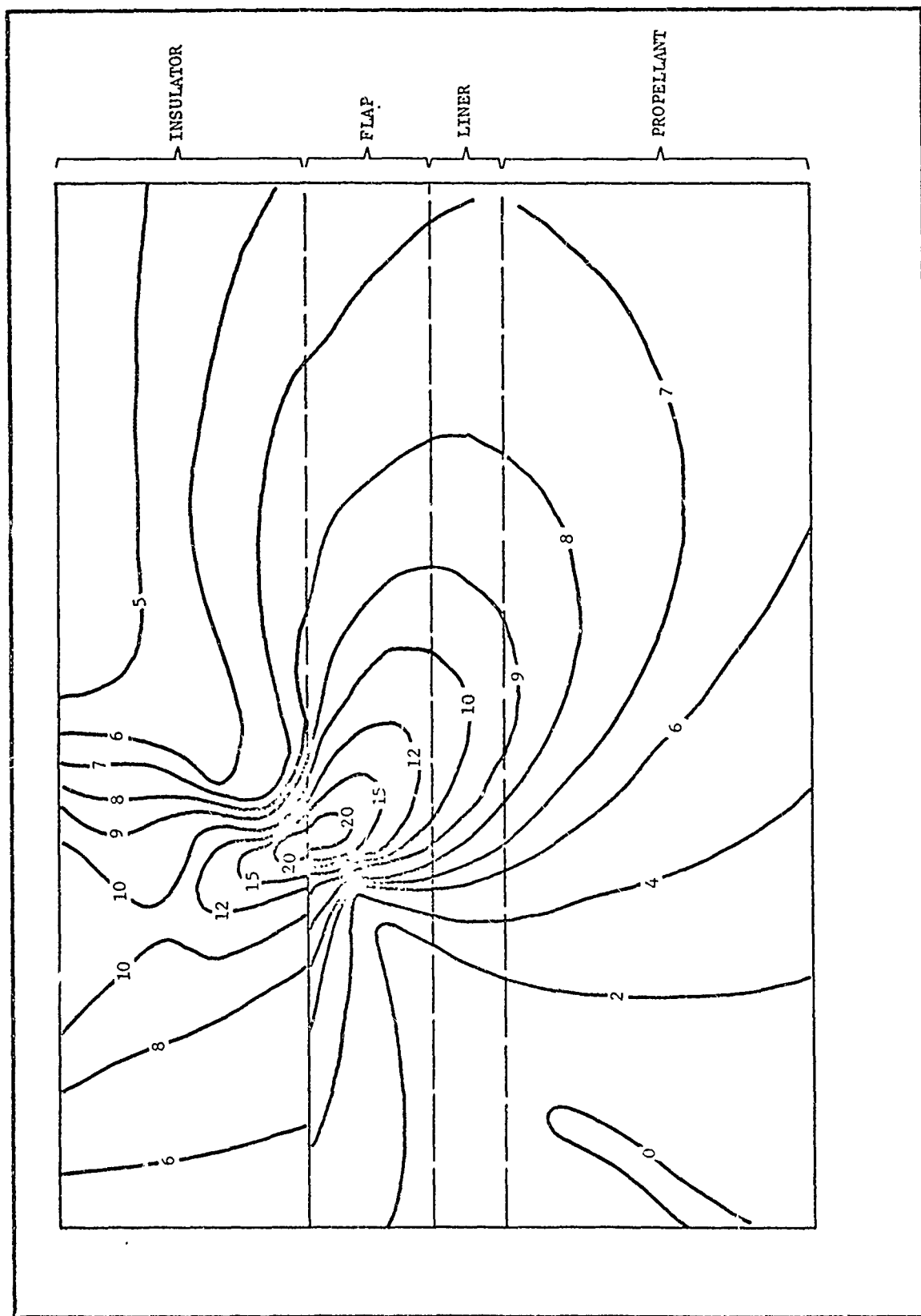


Figure 19. Lines of Constant Maximum Principal Strain $\left(\frac{\epsilon_{\max}}{8}\right)$ in the Vicinity of the Flap Termination for a Cylinder with $L/D = 1.0$ and $W/b = 0.8$
 $(E_{\text{flap}} = E_{\text{insulator}} = E_{\text{liner}} = 200 \text{ psi})$ Under Thermal Shrinkage Loading

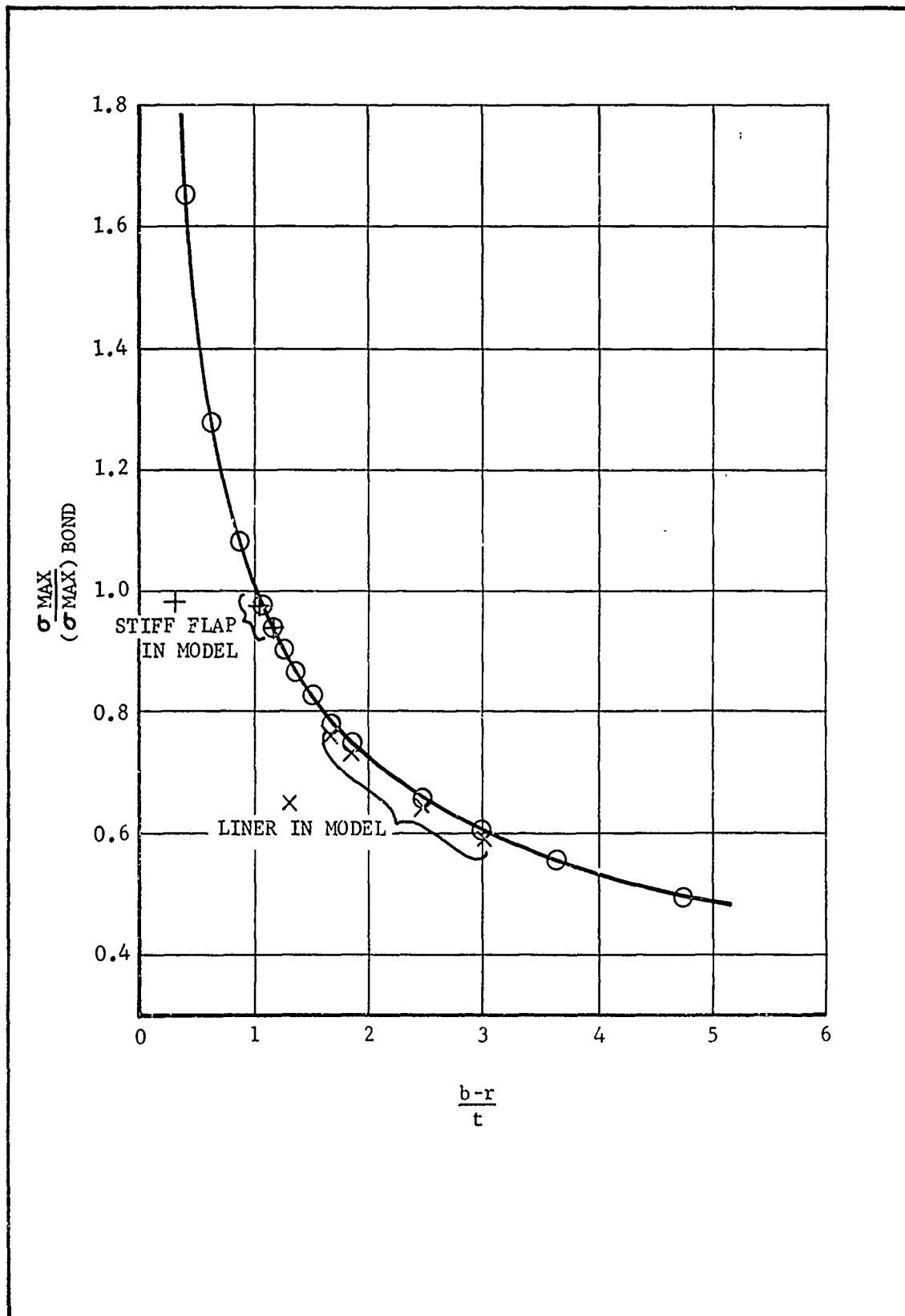


Figure 20. Ratio of the Maximum Principal Stress in the Flap, Liner, and Propellant to that at the Flap-Liner Interface in the Vicinity of the Flap Termination for a Cylinder with $L/D = 1.0$ and $W/b = 0.8$ Under Thermal Shrinkage Loading

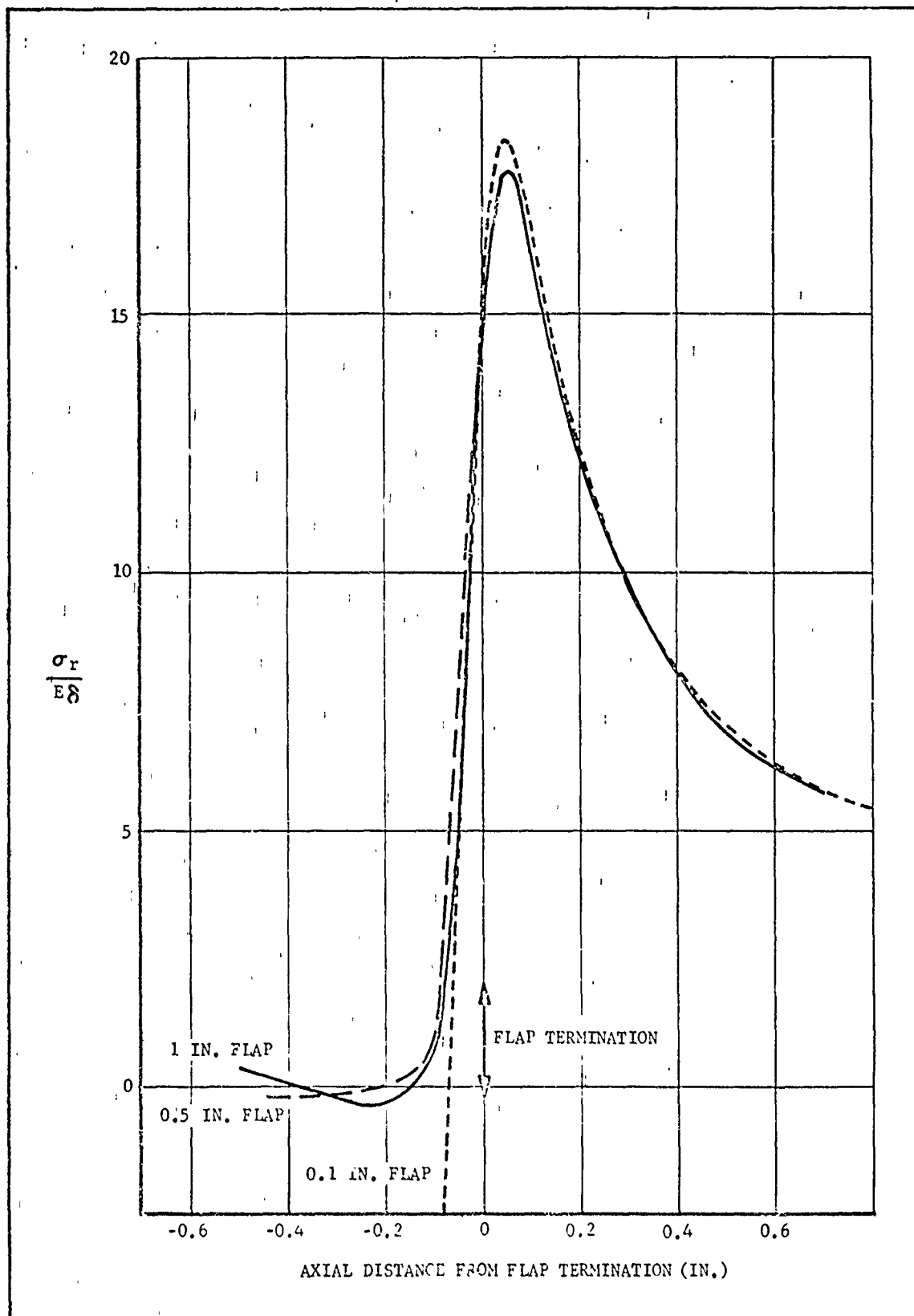


Figure 21. Radial Stress in the Case Bond Liner for a Cylinder with $L/D = 1.0$ and $W/b = 0.8$ and a Variable Flap Length Under Thermal Shrinkage Loading

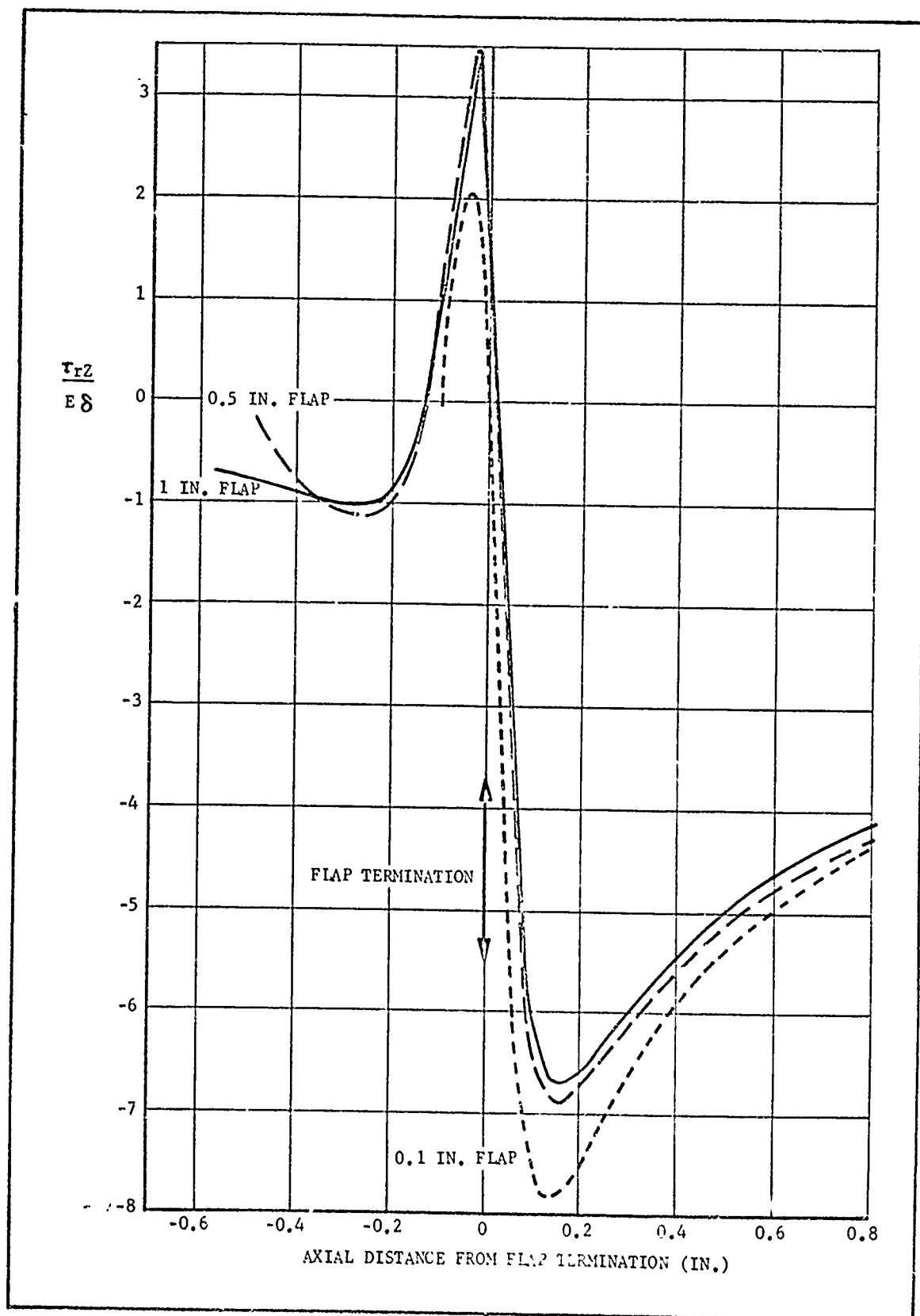


Figure 22. Shear Stress in the Case Bond Liner for a Cylinder with $L/D = 1.0$ and $W/b = 0.8$ and a Variable Flap Length Under Thermal Shrinkage Loading

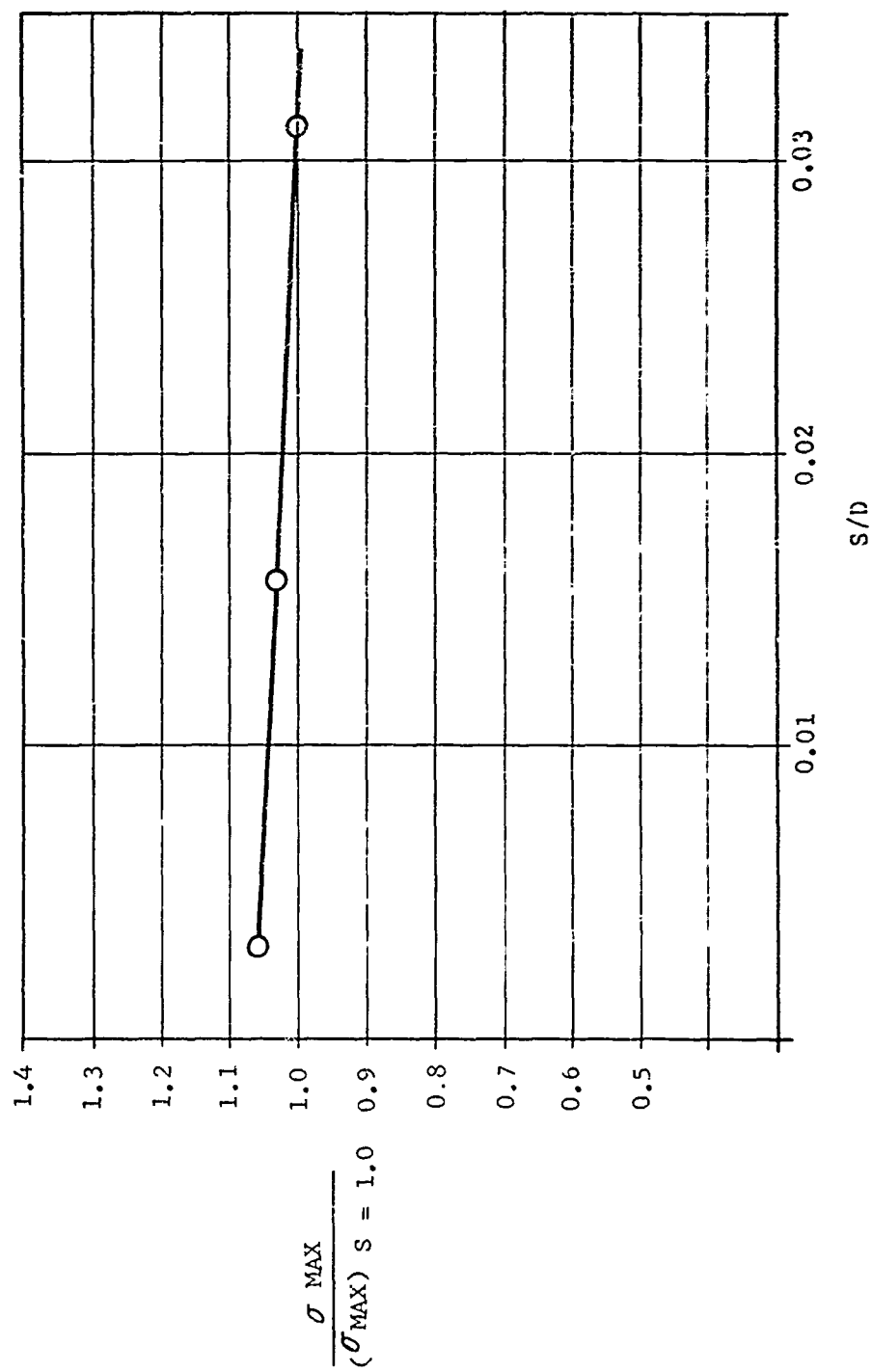


Figure 23. Maximum Principal Stress Adjacent to the Flap Termination for Flap Lengths of 0.1 and 0.5 In. Relative to that for a Flap Length of 1.0 In.

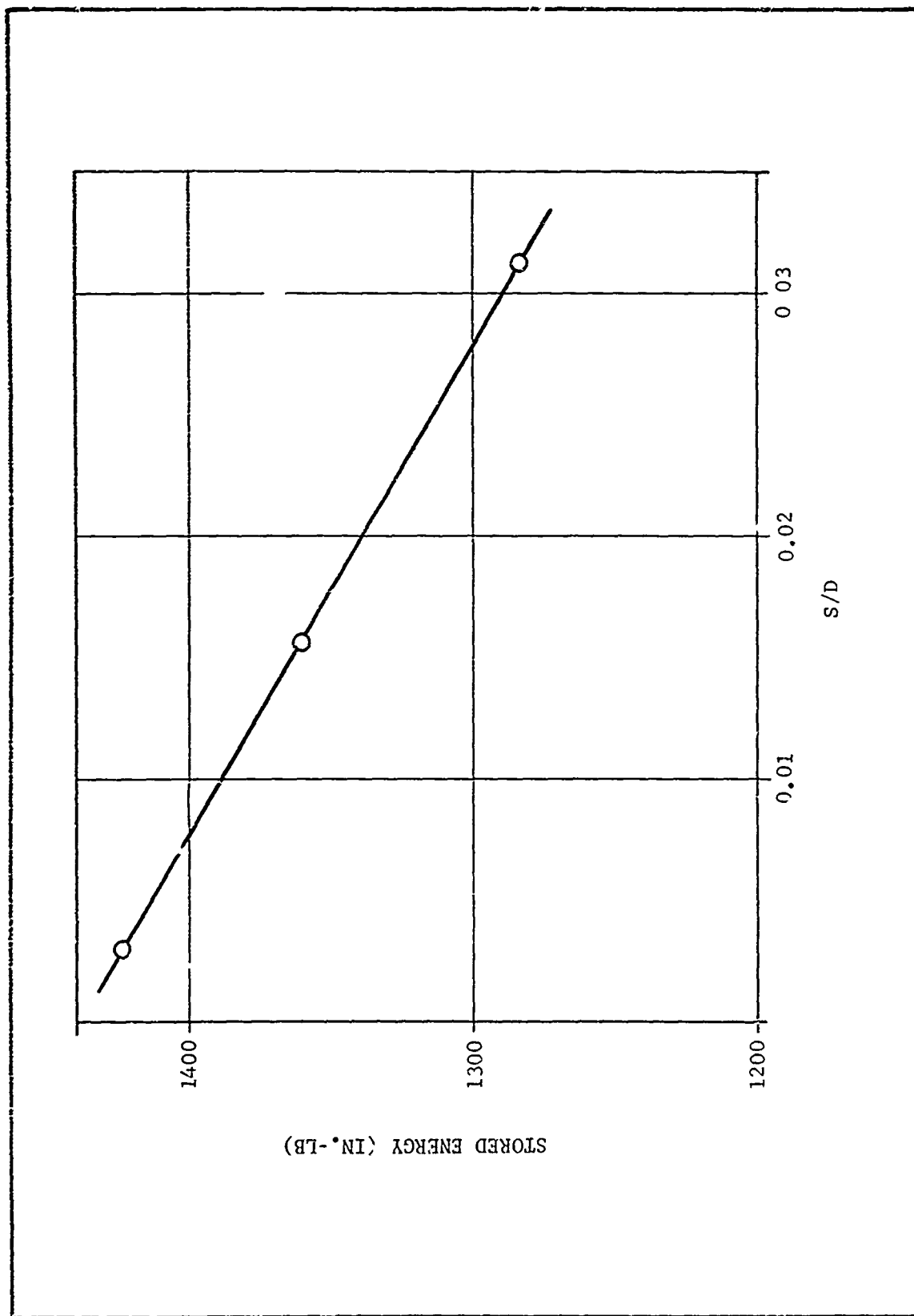


Figure 24. Strain Energy in Cylinder under Thermal Shrinkage Loading, with $L/D = 1.0$ and $W/b = 0.8$, as a Function of Flap Length

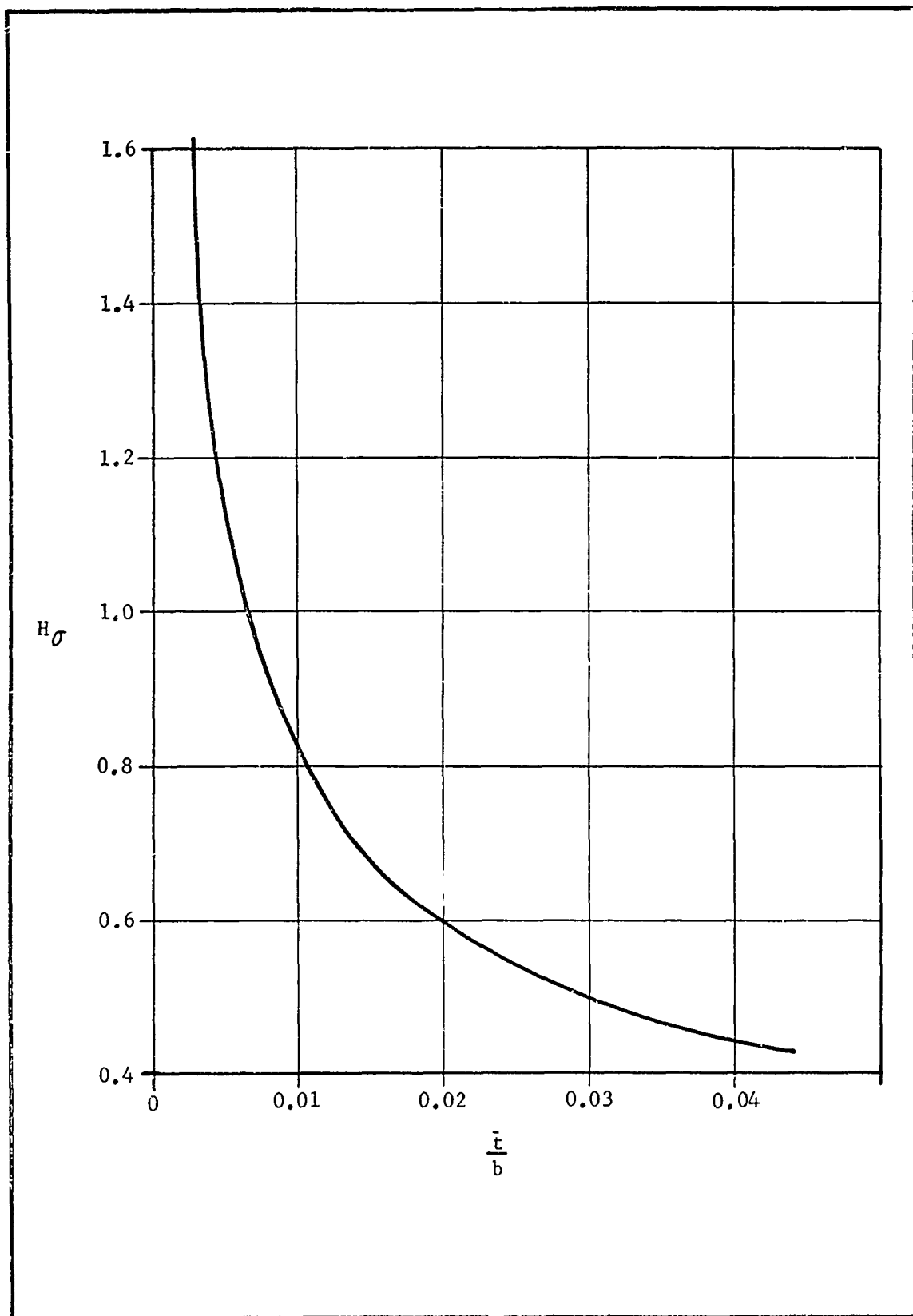


Figure 25. Gradient in Maximum Principal Stress as a Function of Normalized Radial Distance from Flap-Insulator Bond Discontinuity for Cylinder with $L/D = 1.0$ and $W/b = 0.8$

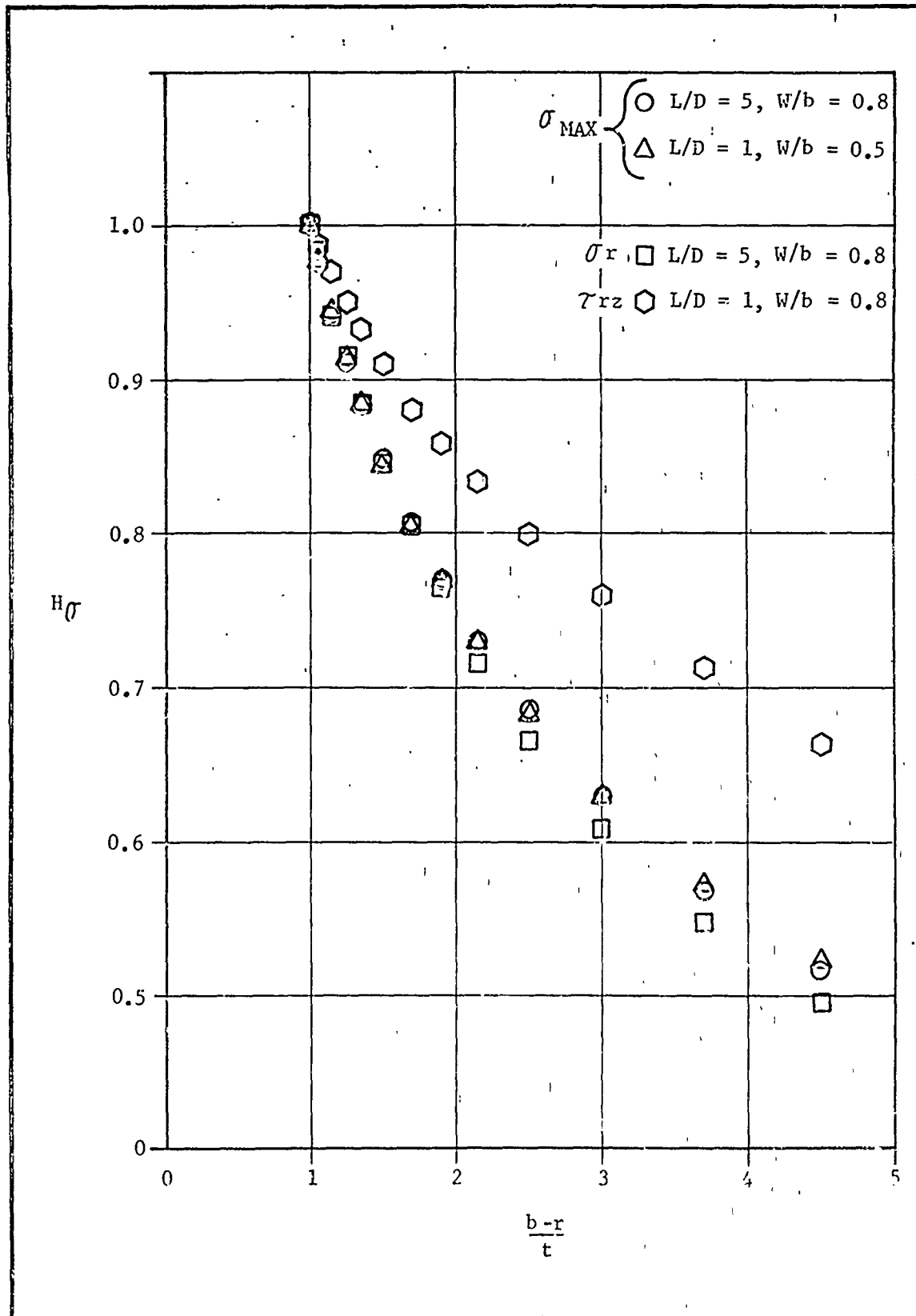


Figure 26. Stress Gradient as a Function of Radial Distance from Flap-Insulator Bond Discontinuity

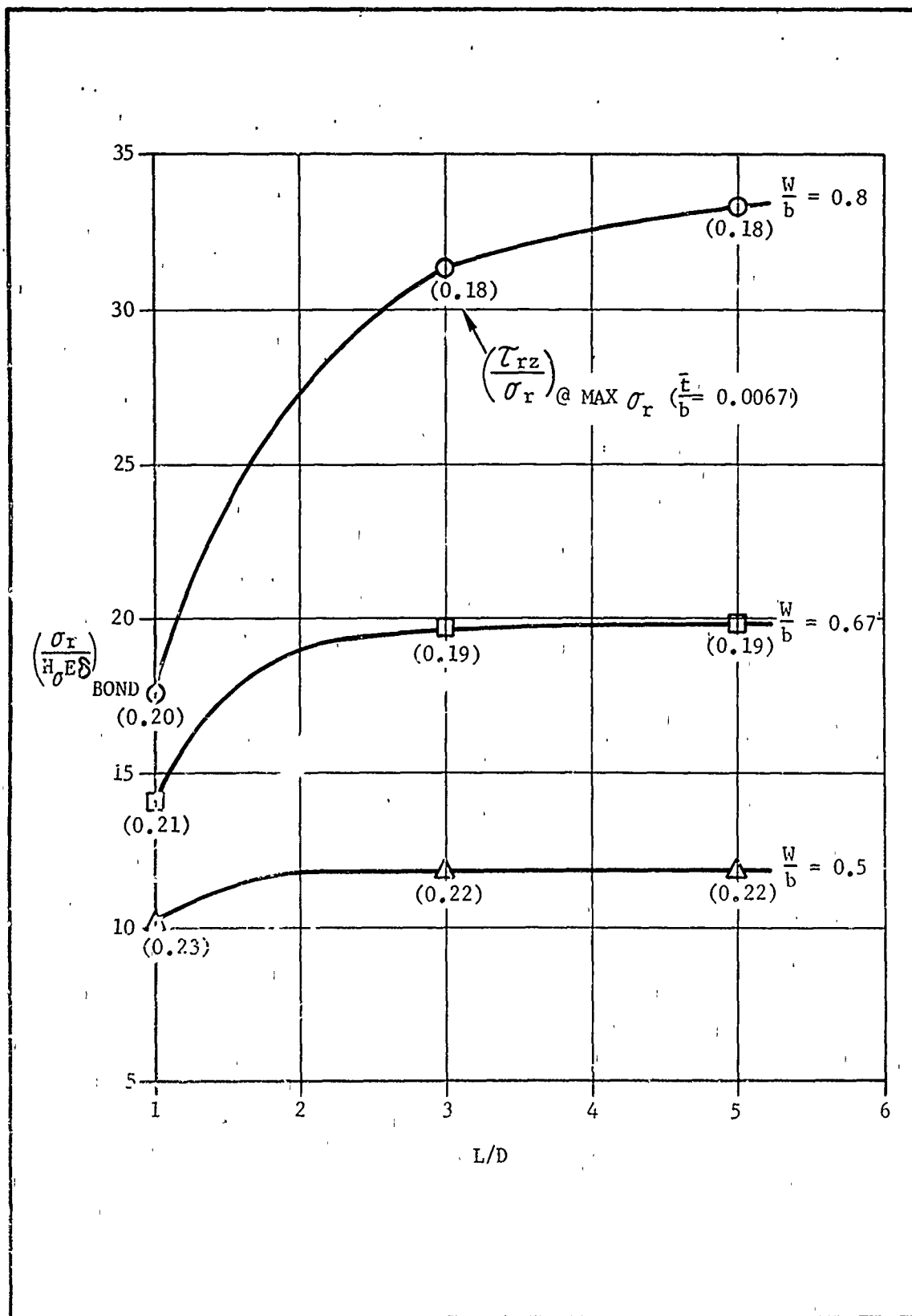


Figure 27. Peak Radial Stress Adjacent to Flap Termination for Cylinder Under Thermal Shrinkage Loading

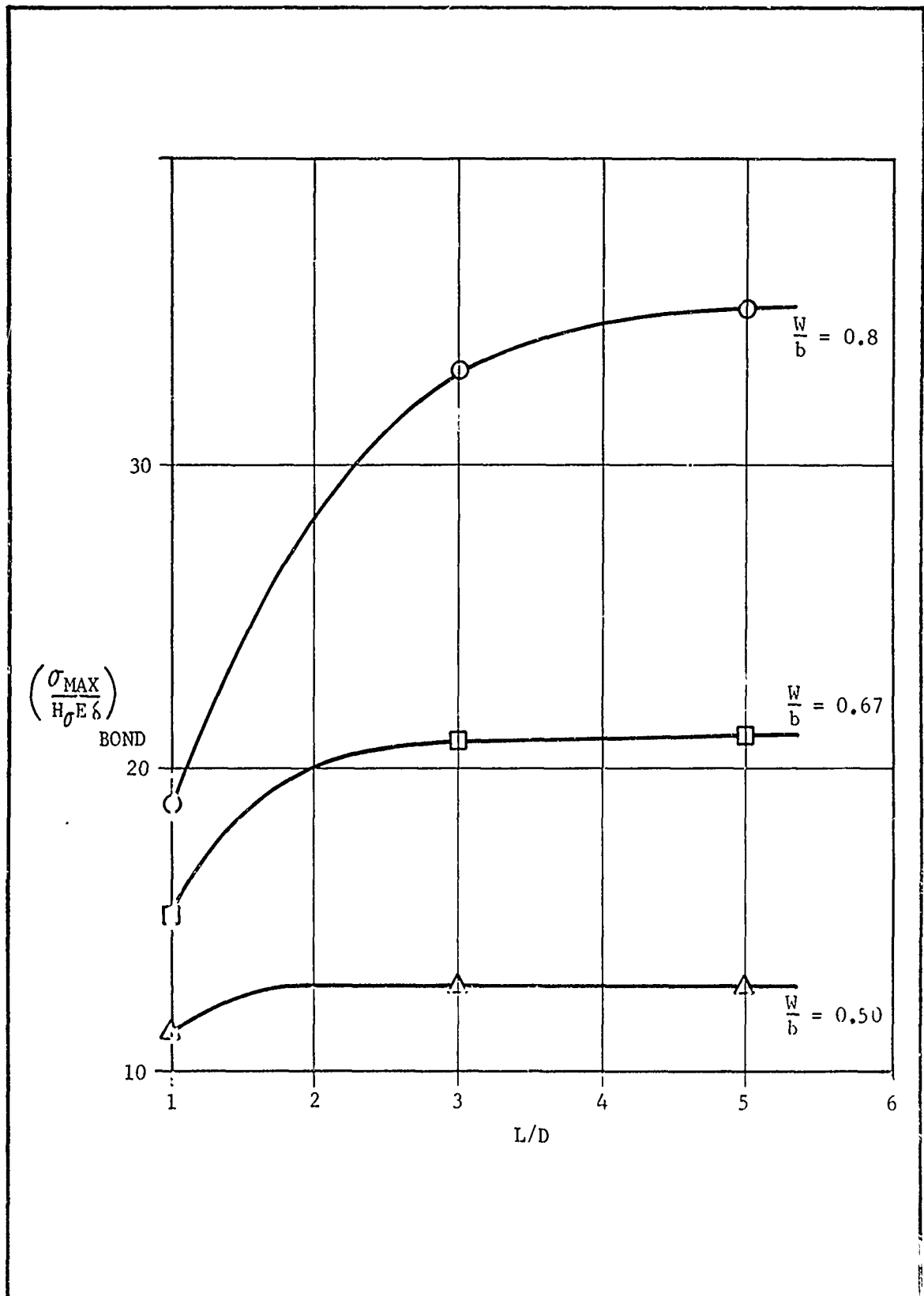


Figure 28. Peak Maximum Principal Stress Adjacent to Flap Termination for Cylinder Under Thermal Shrinkage Loading

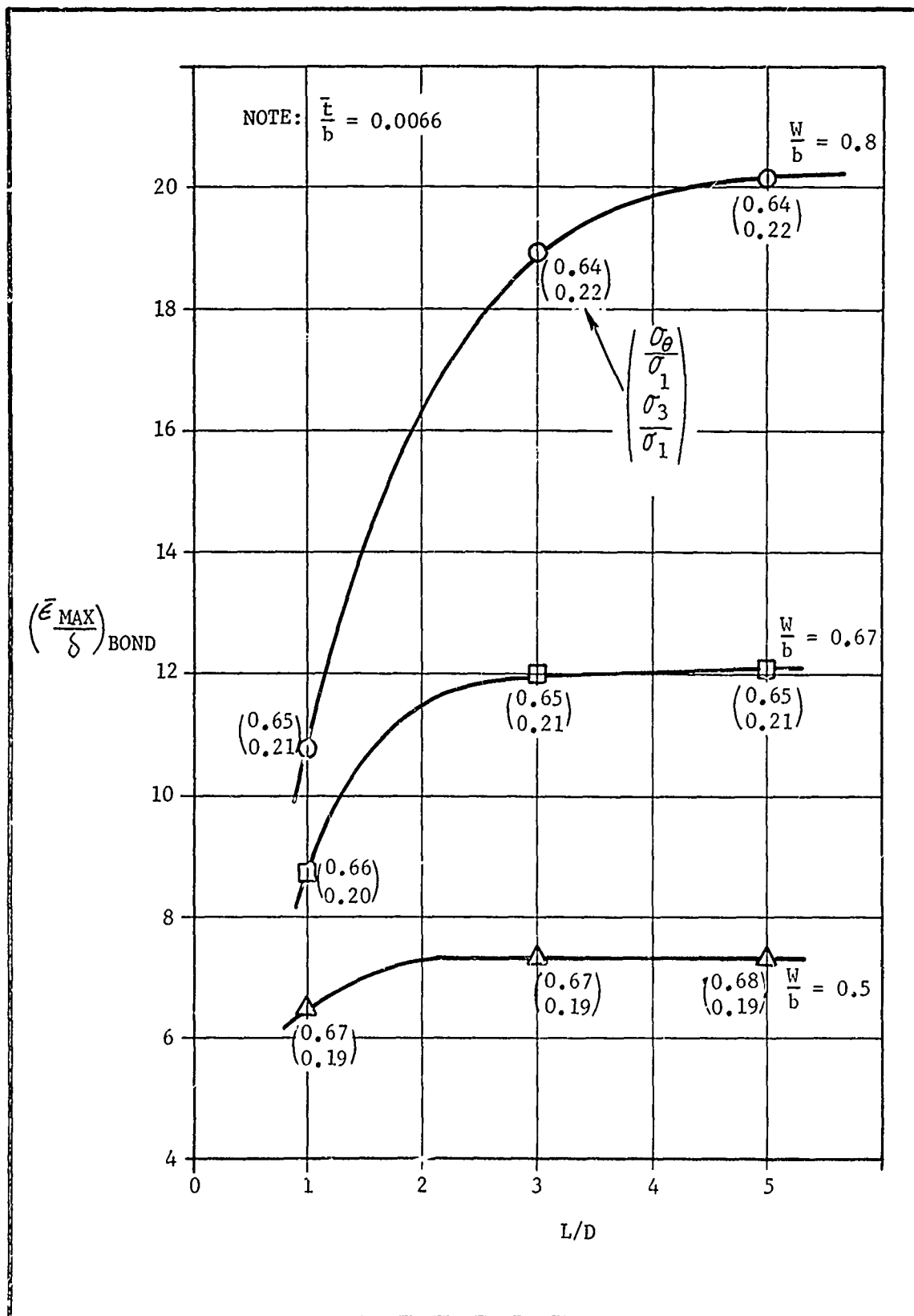


Figure 29. Peak Maximum Principal Strain in Propellant Adjacent to Flap Termination for Cylinder Under Thermal Shrinkage Loading

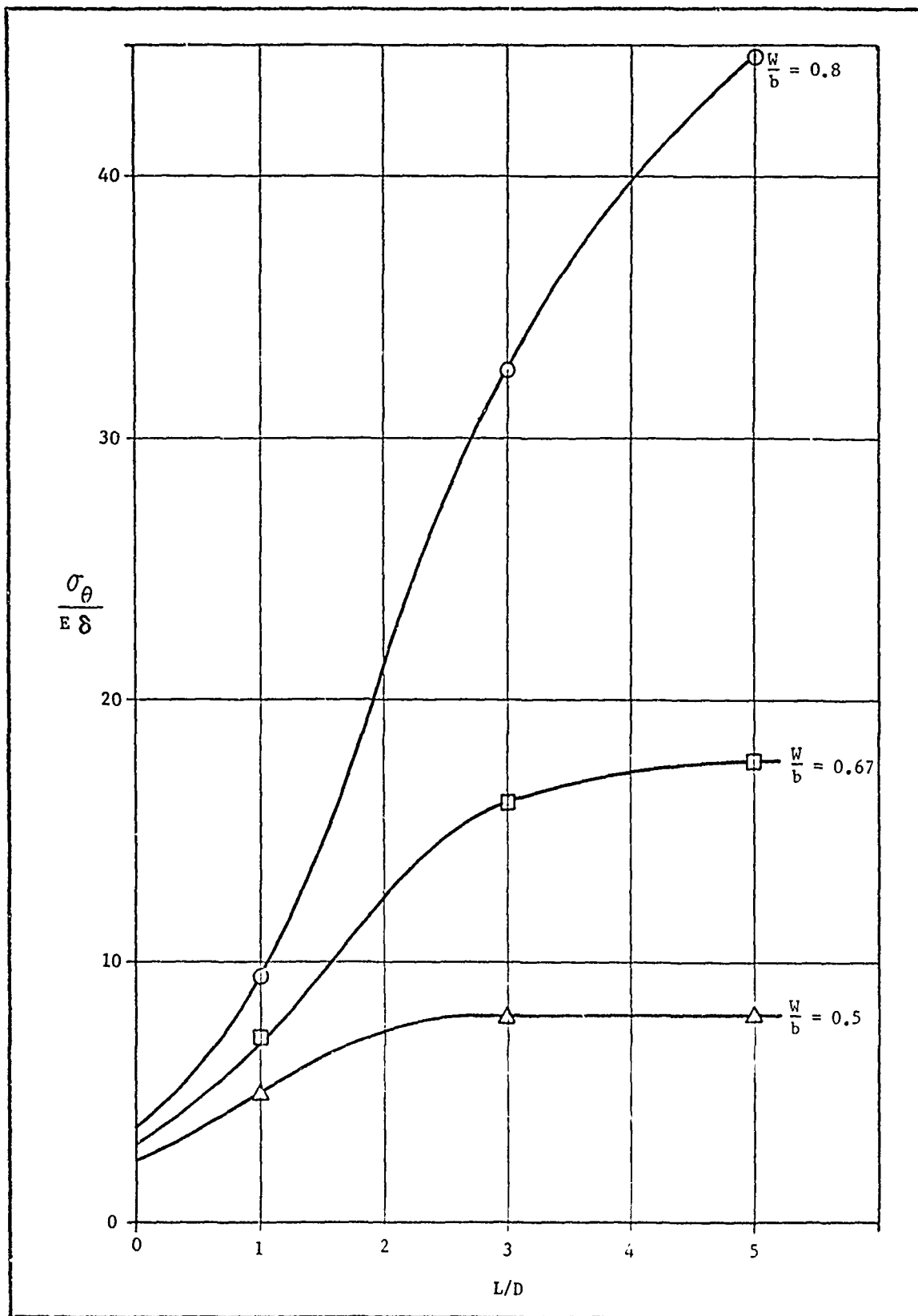


Figure 30. Peak Center Port Hoop Stress for Cylinder Under Thermal Shrinkage Loading

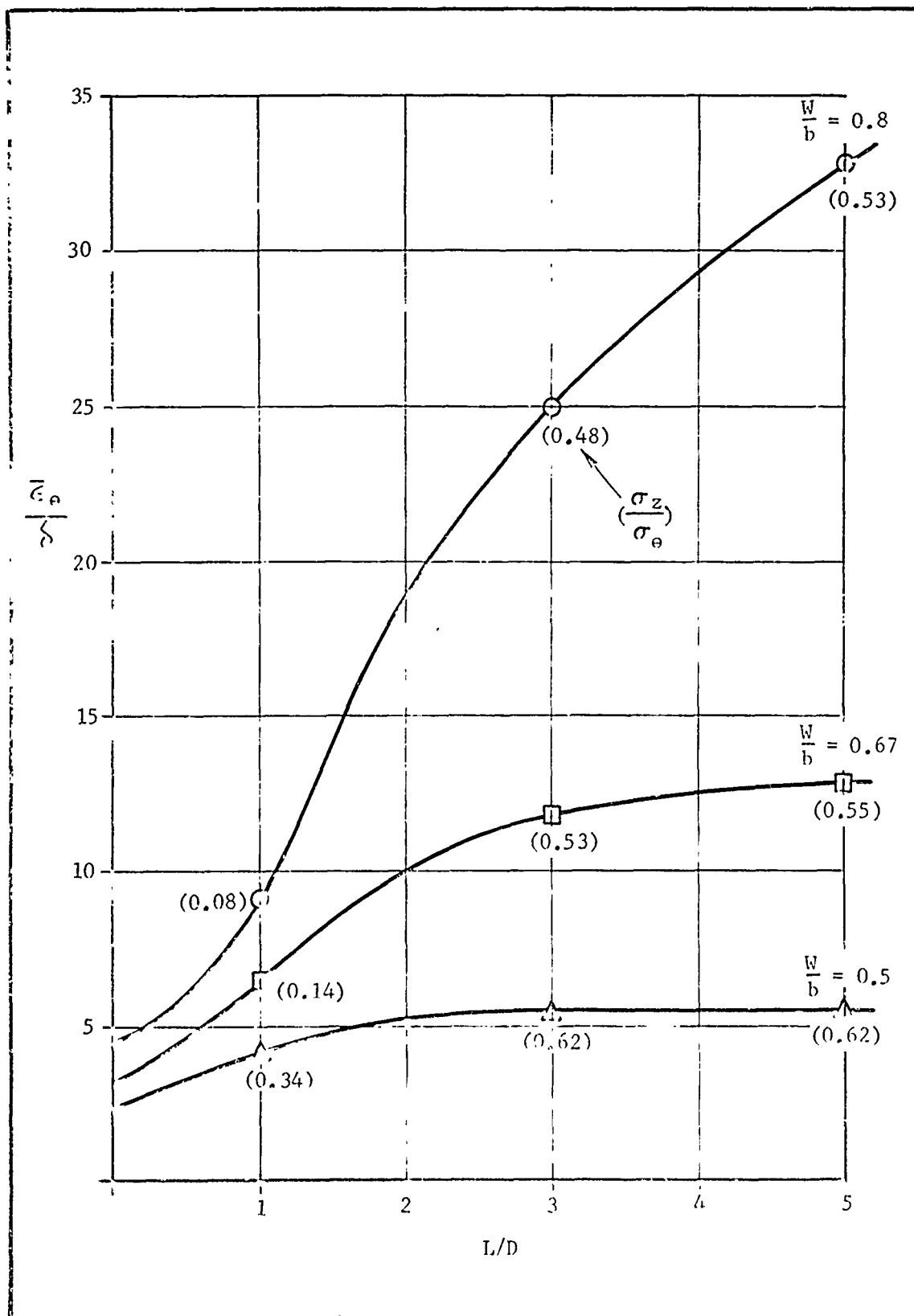


Figure 31. Peak Center Port Hoop Strain for Cylinder Under Thermal Shrinkage Loading

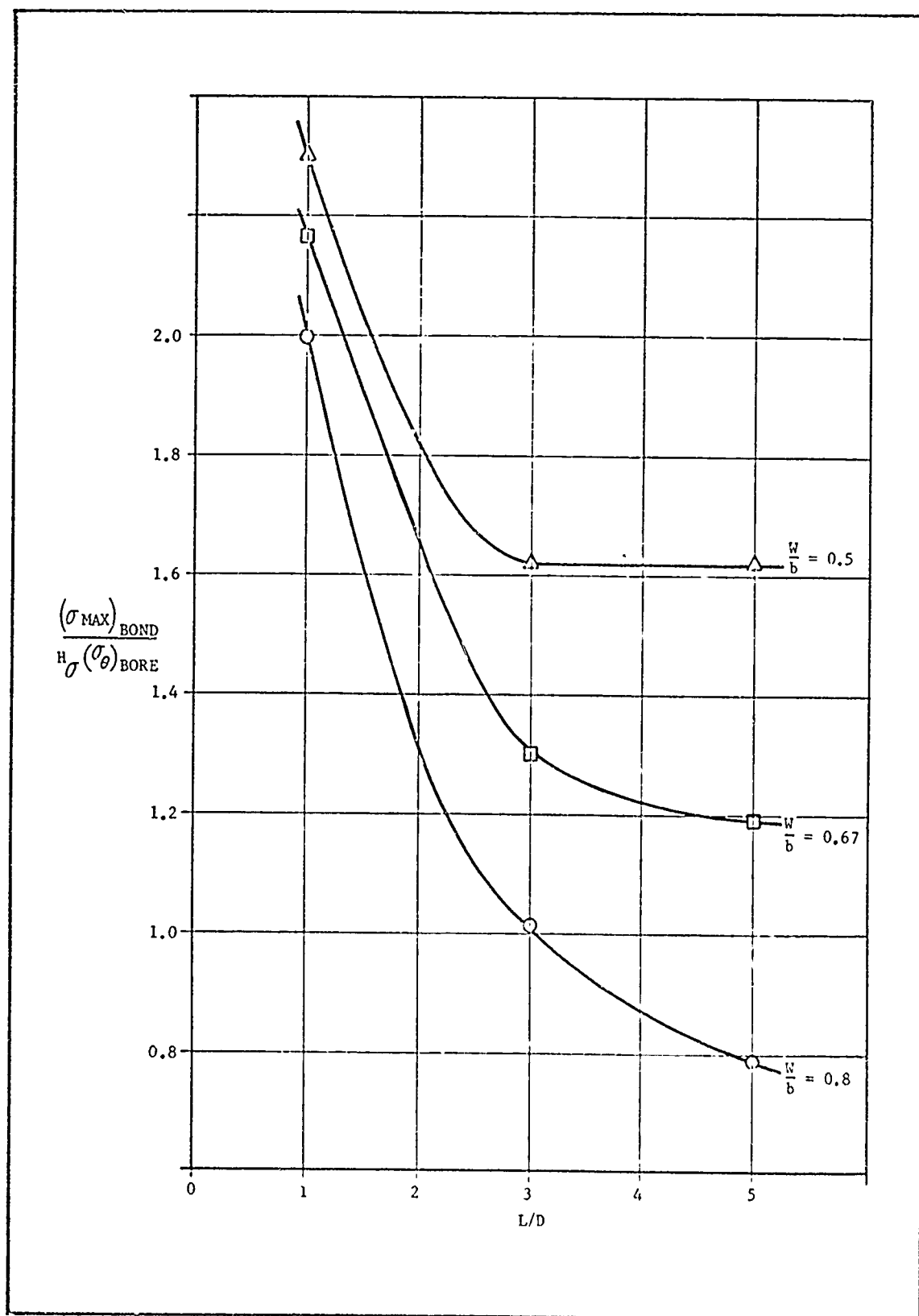


Figure 32. Ratio of Peak Maximum Principal Propellant Stress Near Flap Termination to Maximum Center Port Hoop Stress for Cylinder under Thermal Shrinkage Loading

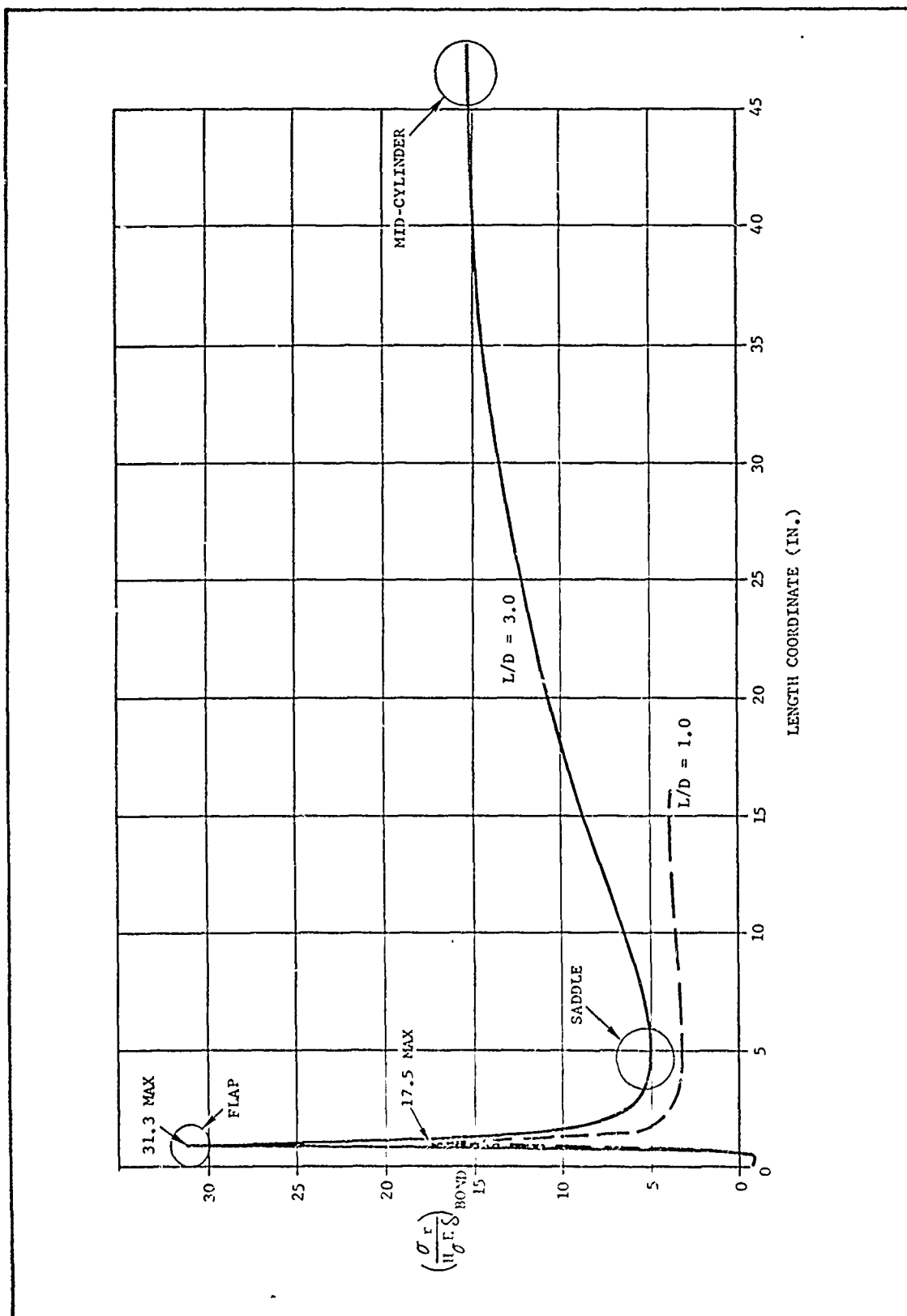


Figure 33. Case Bond Line Stress in Radial Direction for Cylinder with $L/D = 1.0$ and 3.0 , $W/b = 0.8$, Under Thermal Shrinkage Loading

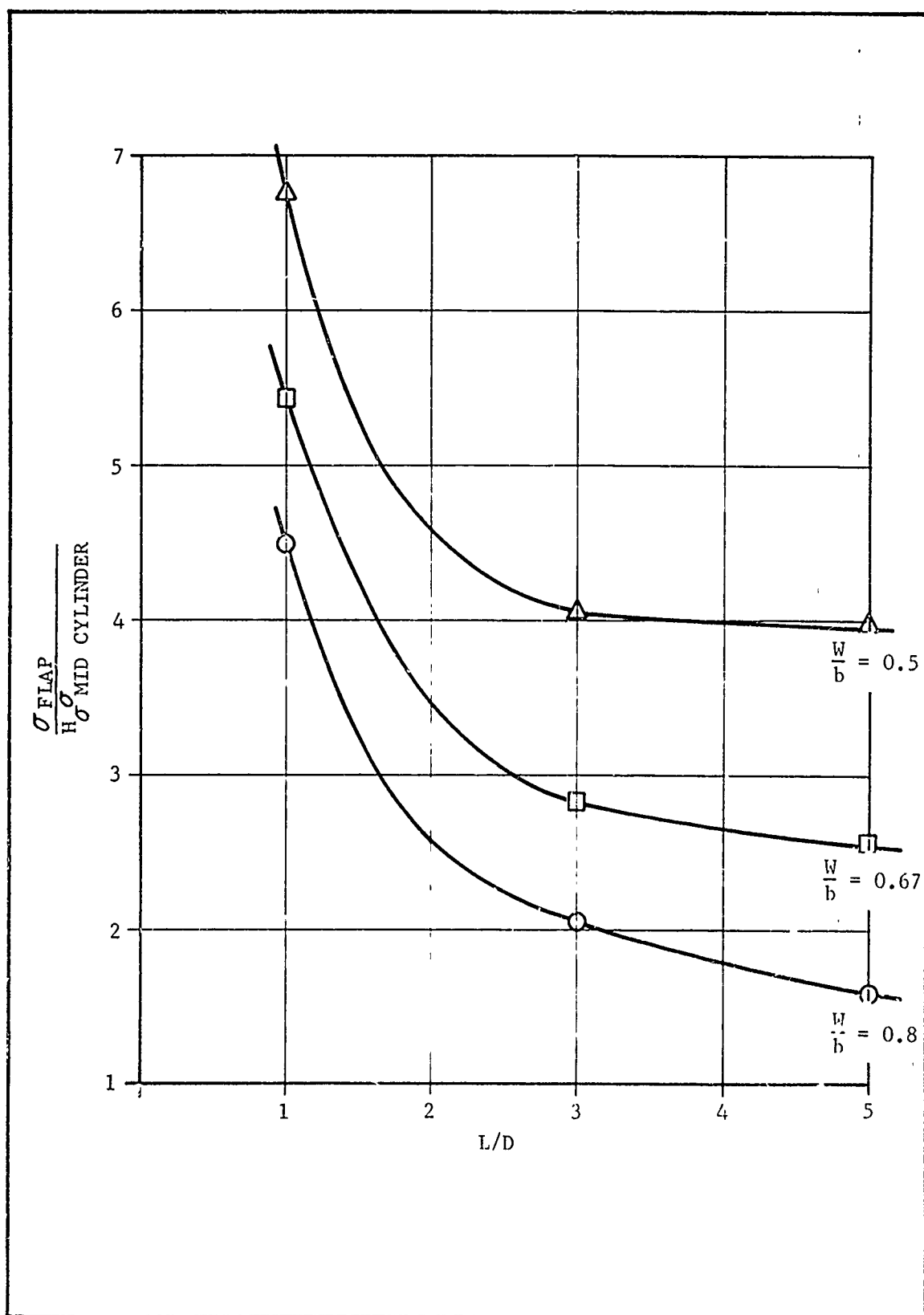


Figure 34. Ratio of the Peak Radial Liner Stress Near Flap Termination to Mid-Cylinder Value for Cylinder Under Thermal Shrinkage Loading

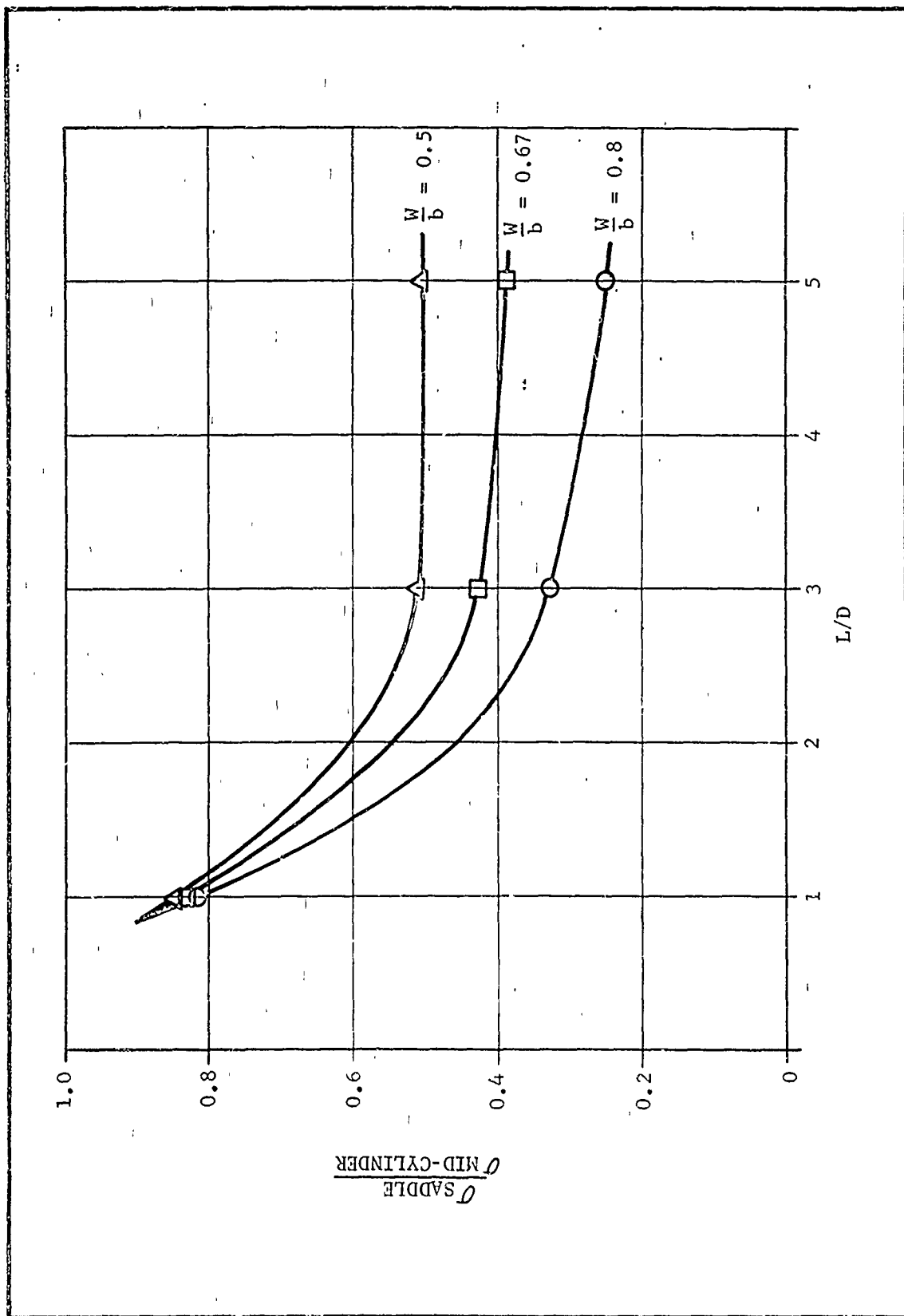


Figure 35. Ratio of Radial Liner Stress in Saddle to Mid-Cylinder Value for Cylinder Under Thermal Shrinkage Loading

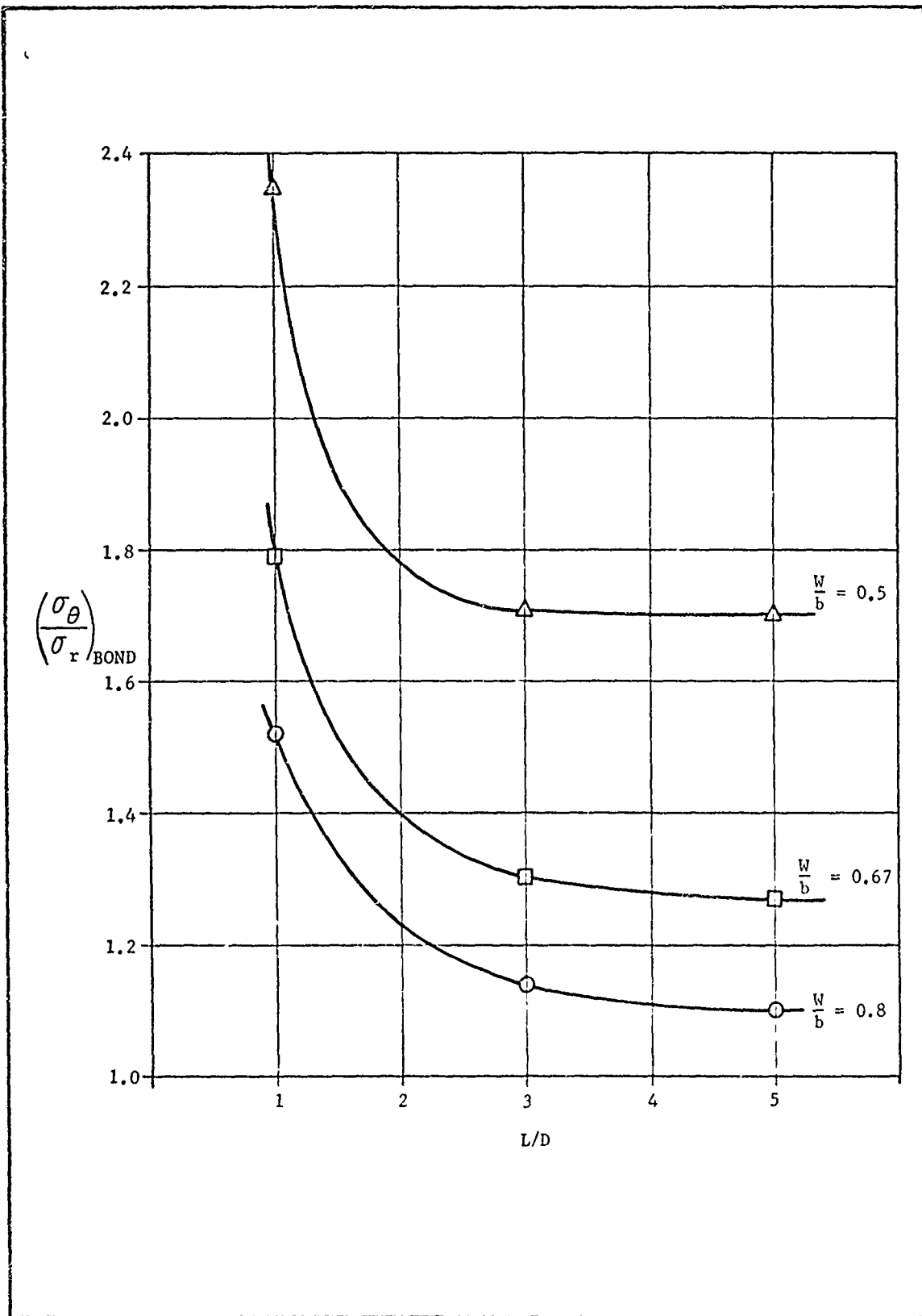


Figure 36. Ratio of Liner Hoop to Radial Stress at Mid-Axial Position in Cylinder Under Thermal Shrinkage Loading

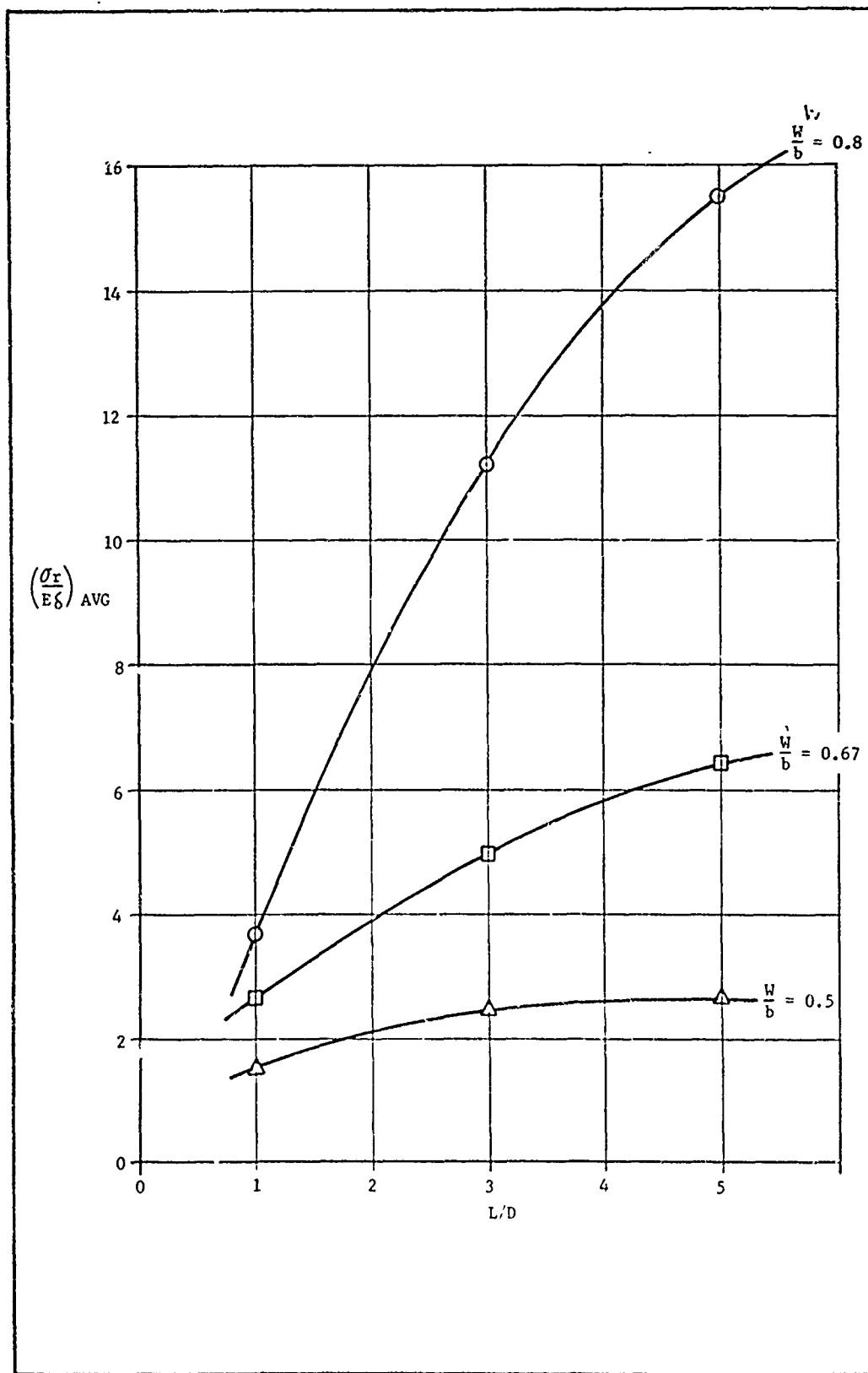


Figure 37. Average Case Bond Radial Stress in Cylinder Under Thermal Shrinkage Loading

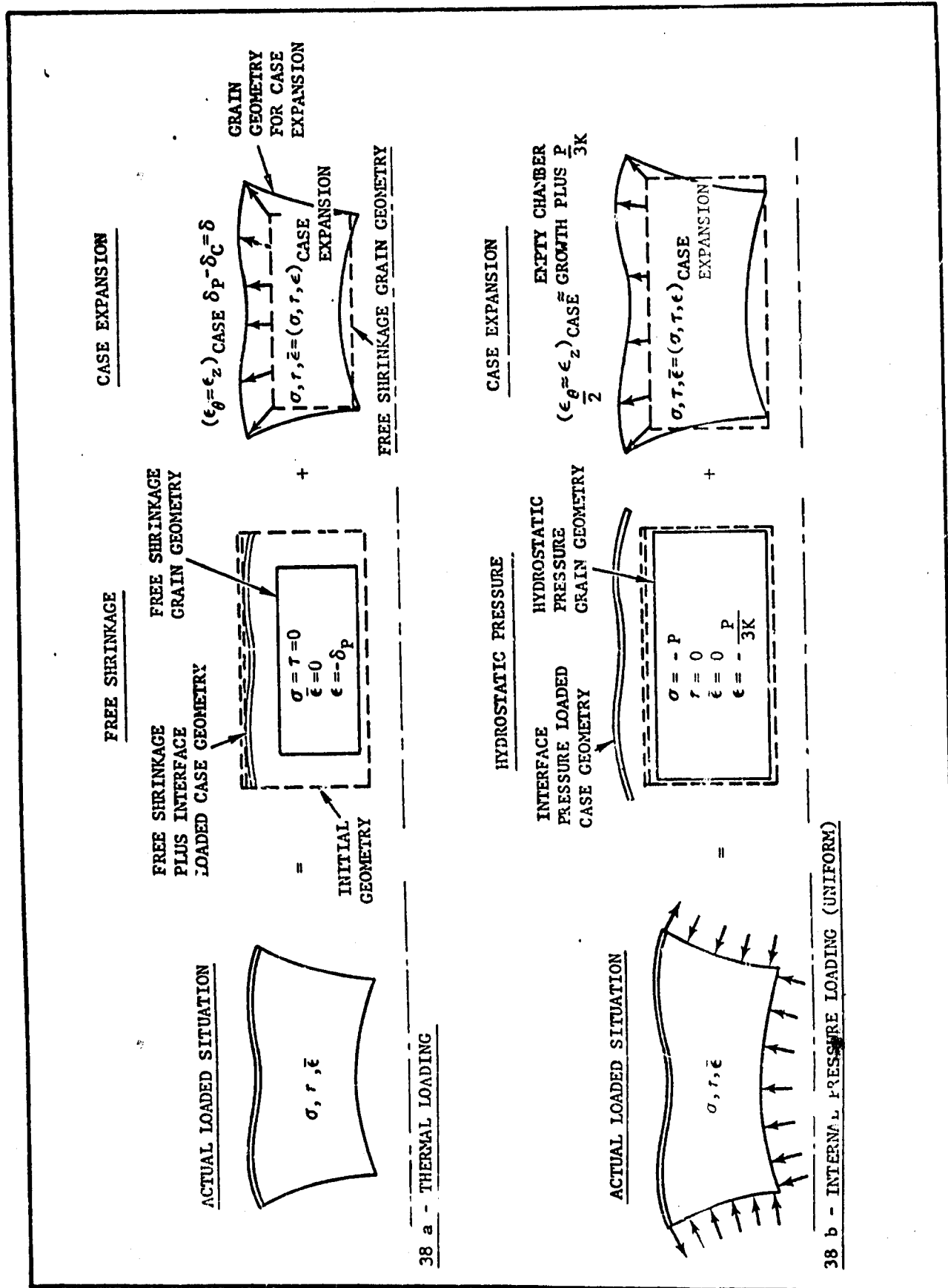


Figure 38. Correspondence of Stresses and Strains Resulting from Thermal Shrinkage and Internal Pressurization of Two-Layered Cylinders

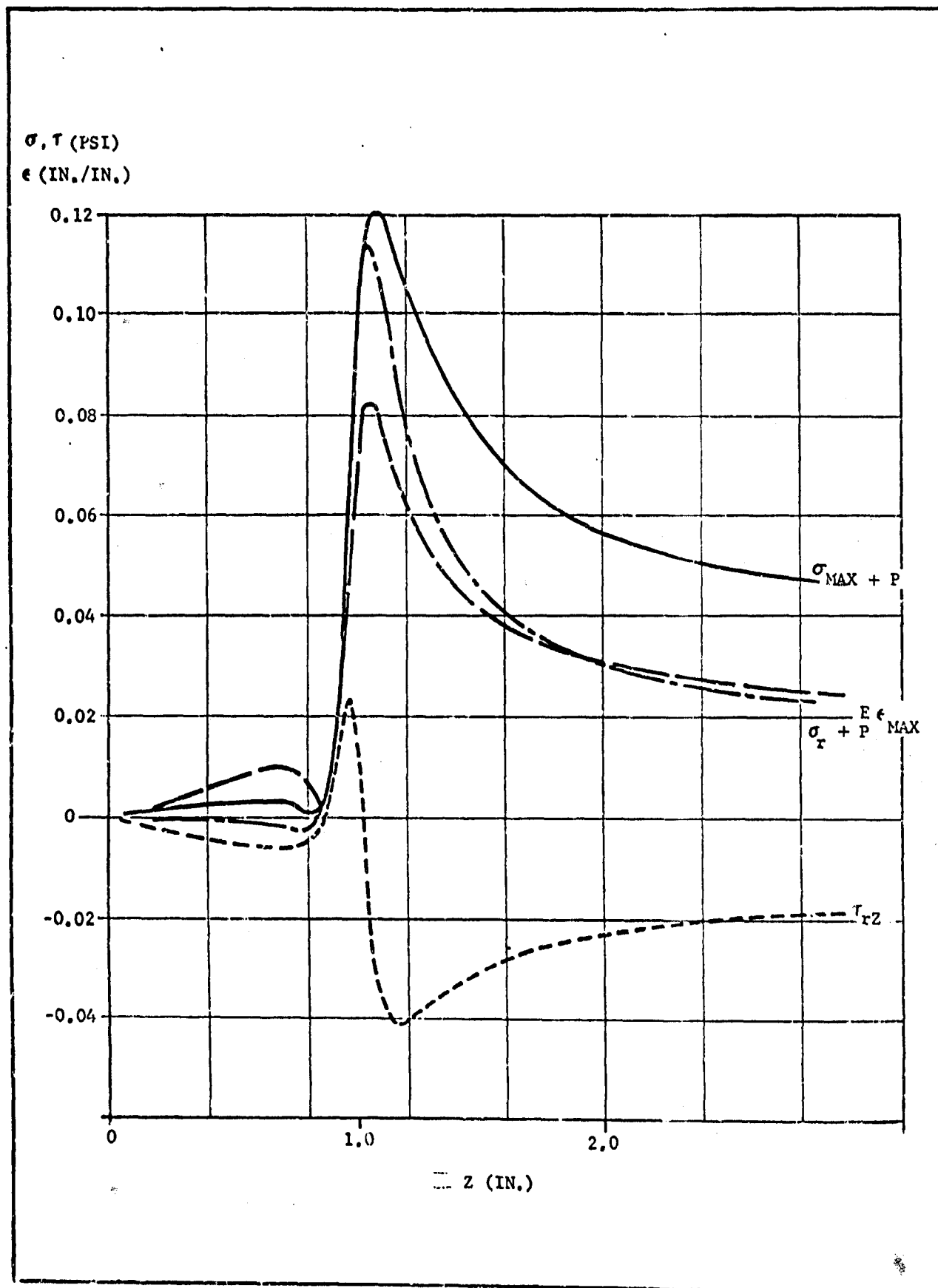


Figure 39. Case Bond Liner Stresses Near the Flap Termination for a Cylinder with $L/D = 1.0$ and $W/b = 0.8$ Under 1.0 psi Internal Pressure Loading

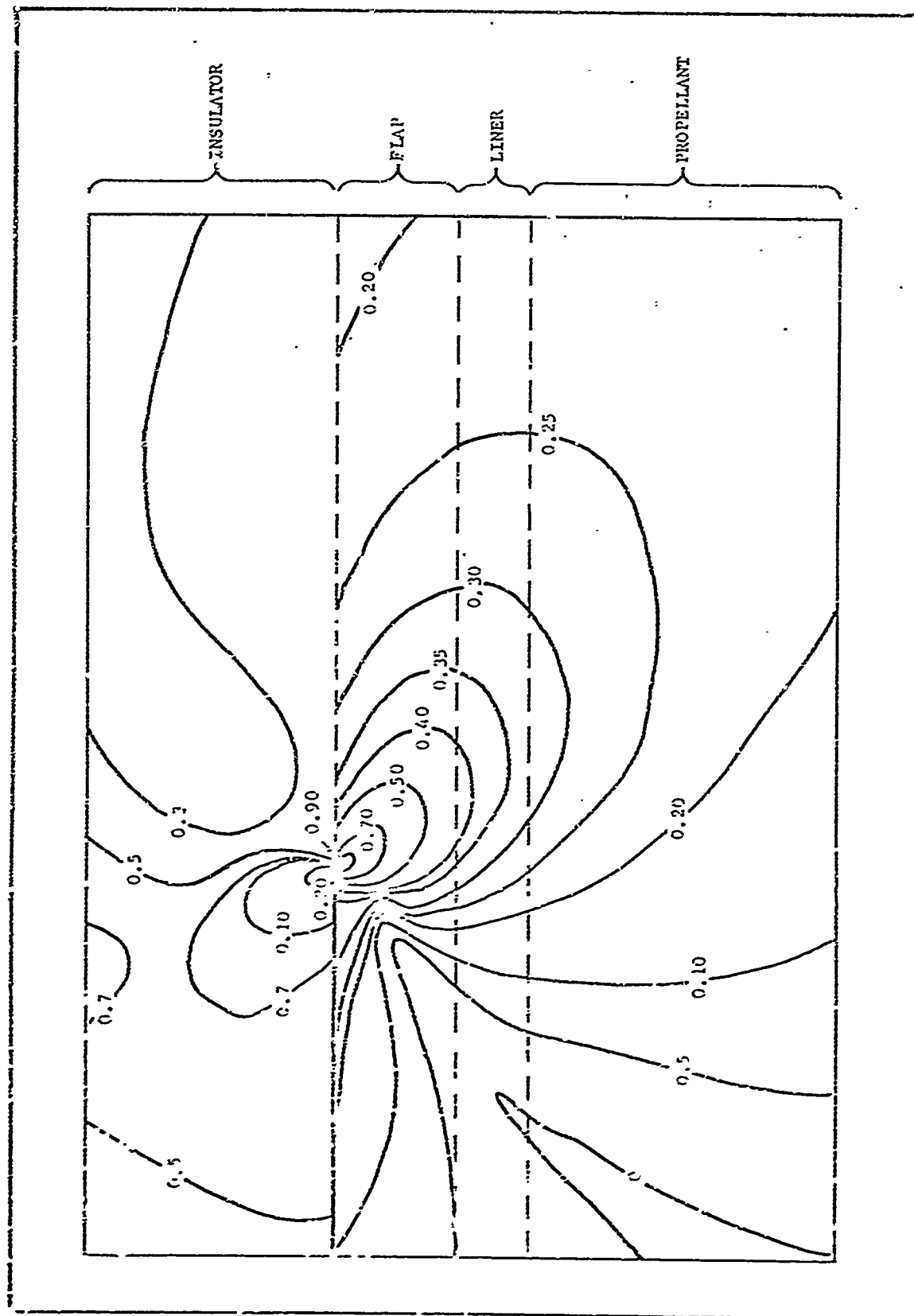


Figure 40. Lines of Constant Maximum Principal Strain (ϵ_{max}) in the Vicinity of the Flap Termination for a Cylinder with $L/D = 1.0$ and $W/b = 0.8$ Subjected to 1000 psi Internal Pressure Loading

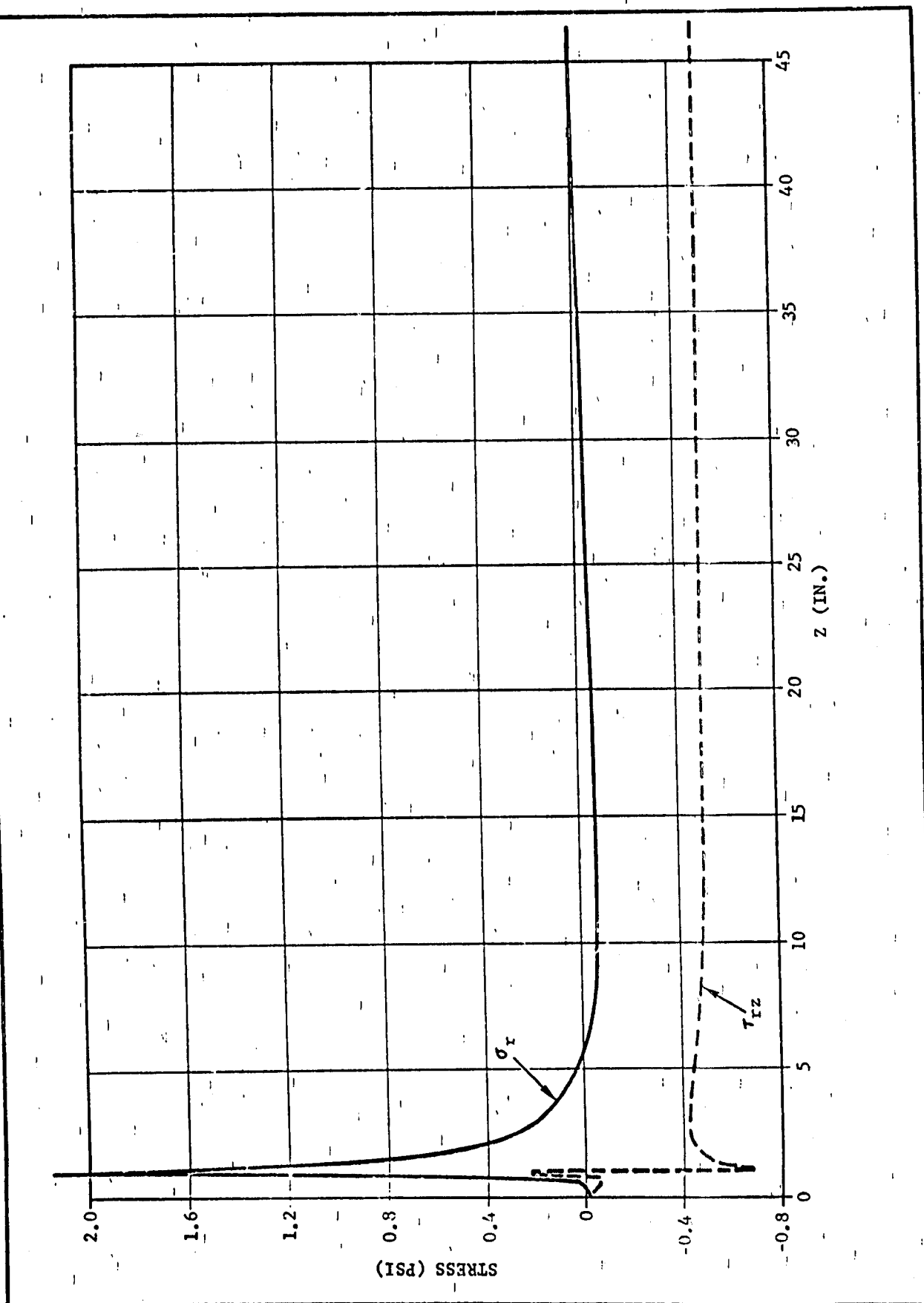


Figure 41. Case Bond Liner Stresses for a 32-Inch Diameter Cylinder with $L/D = 3.0$ and $w/b = 0.8$ Under 1 g Axial Acceleration Loading ($\rho_w = 0.064 \text{ lb/in.}^3$)

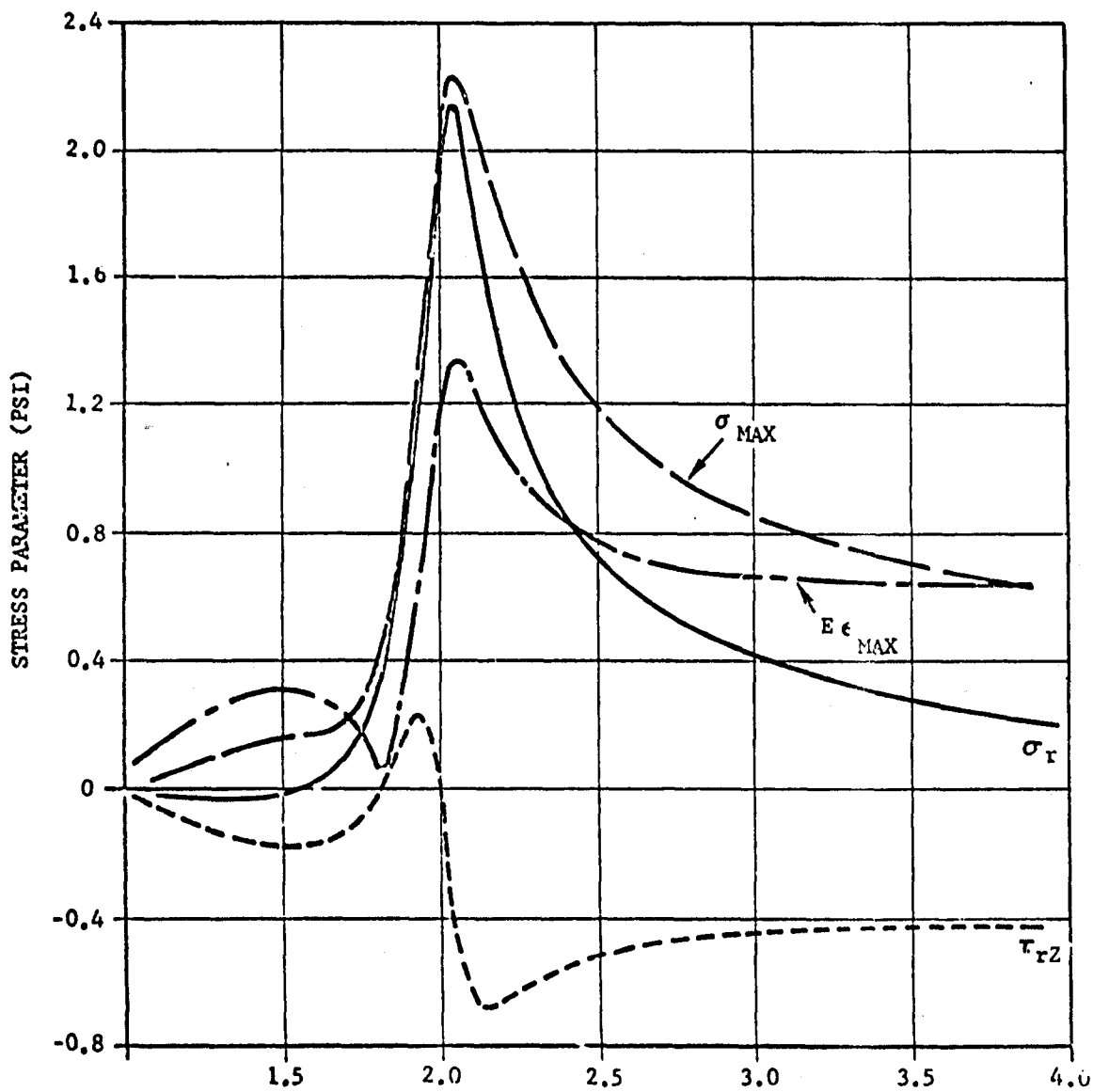


Figure 42. Case Bond Liner Stresses Adjacent to Flap Termination in a 32-Inch Diameter Cylinder with $L/D = 3.0$ and $W/b = 0.8$ Under 1 g Axial Acceleration Loading ($P_W = 0.064 \text{ lb/in.}^3$)

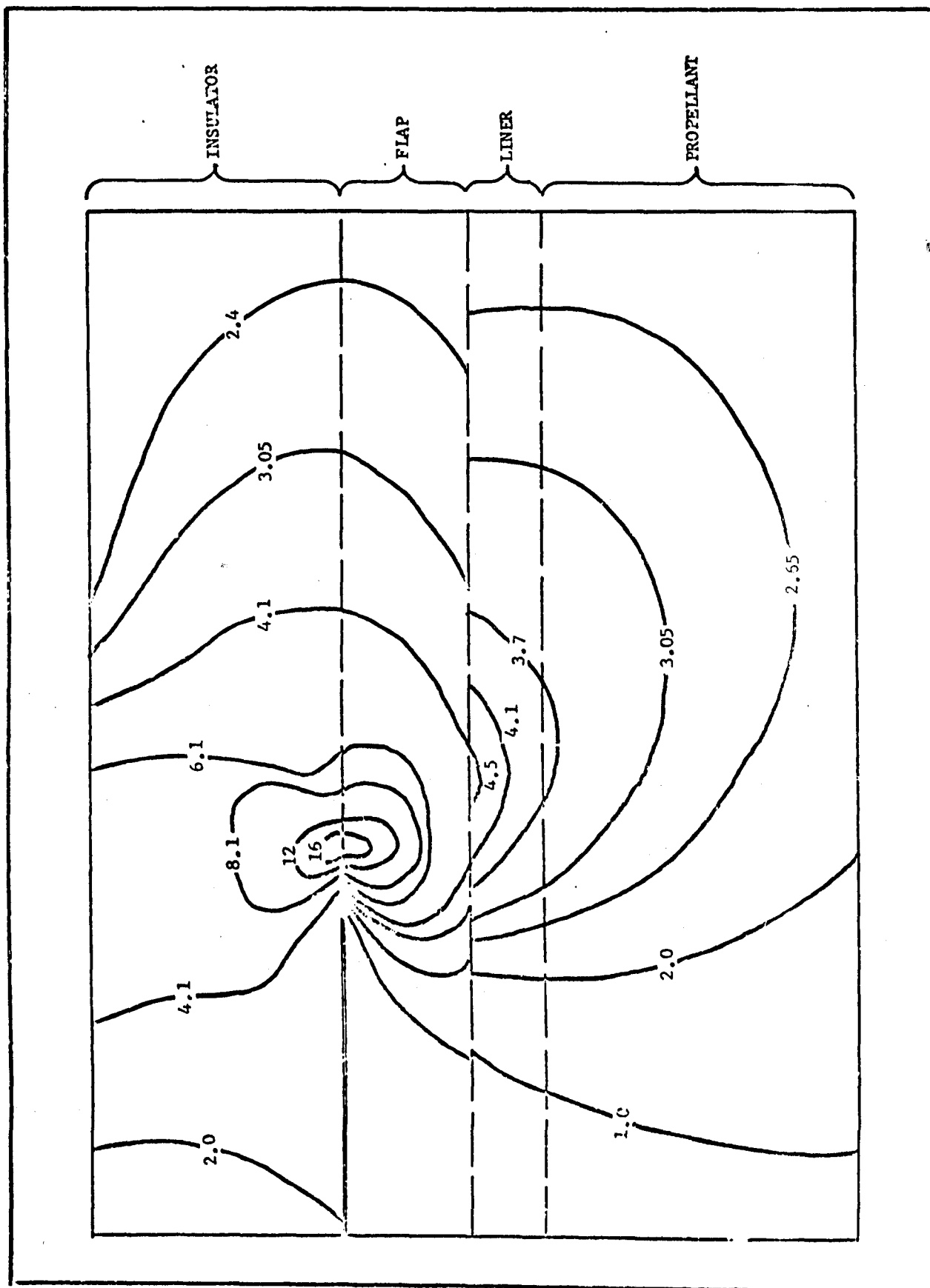


Figure 43. Lines of Constant Maximum Principal Strain $\left(\frac{\sigma_{\max}}{\tau_{\text{avg}}} \right)$ in the Vicinity of the Flap

Termination for a Cylinder with $L/D = 3.0$ and $W/b = 0.8$ Under Axial Acceleration Loading

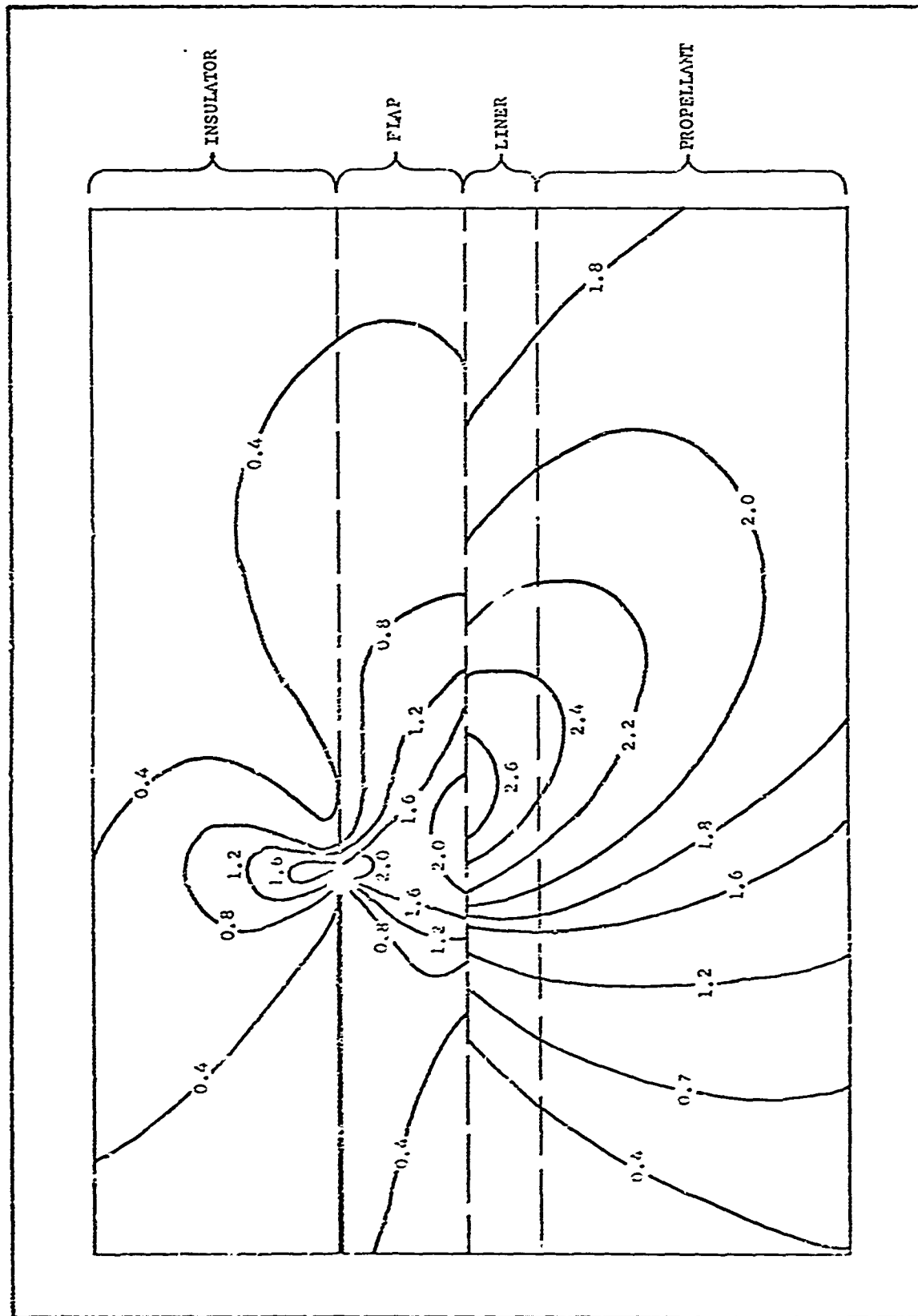


Figure 4. Lines of Constant Maximum Principal Strain $\left(\frac{E \epsilon_{\max}}{\tau_{\text{avg}}} \right)$ in the Vicinity of the Flap Termination for a Cylinder with $L/D = 3.0$ and $W/b = 0.8$ Under Axial Acceleration Loading

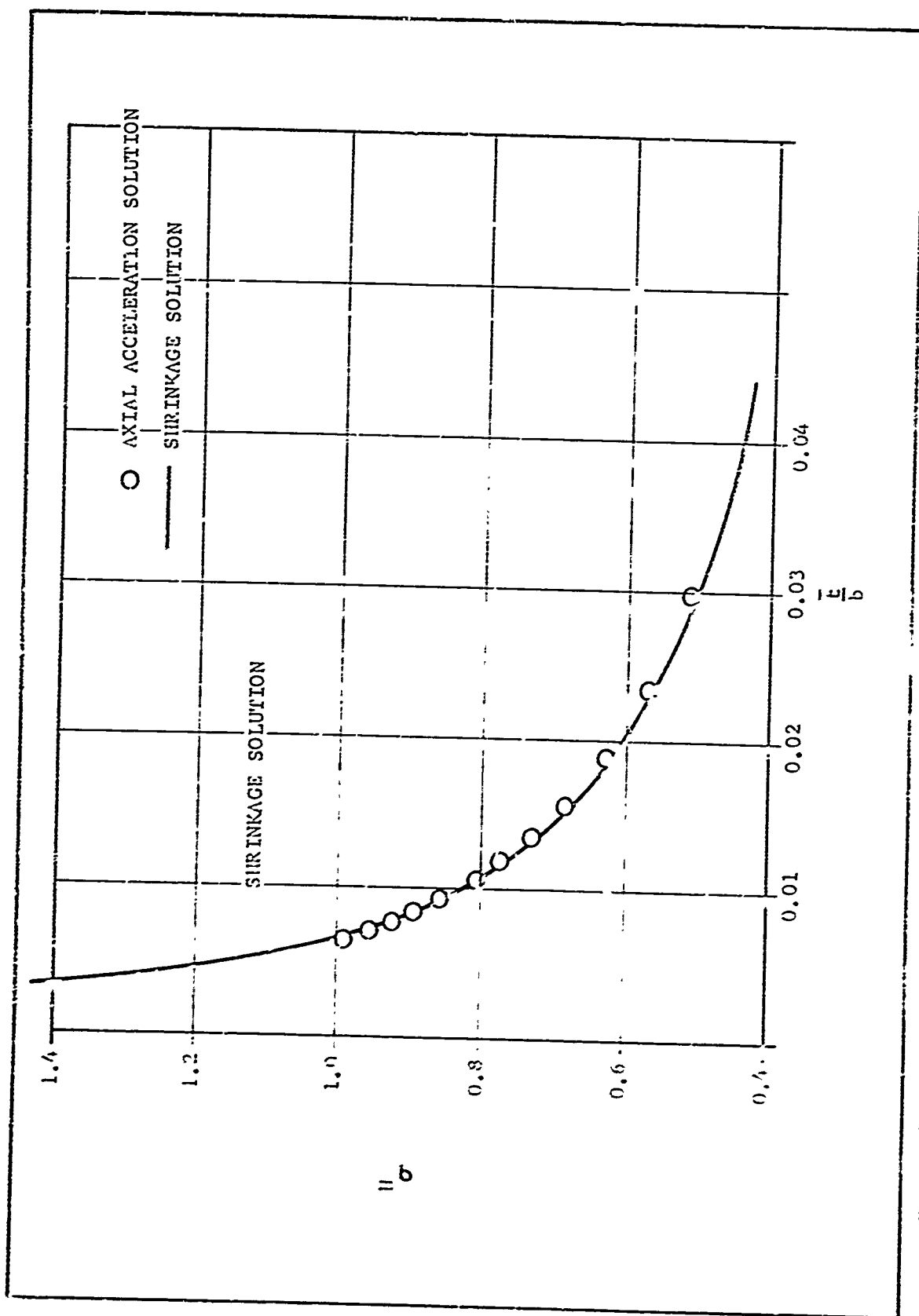


Figure 35. Comparison of Gradient in Maximum Principal Stress as a Function of Normalized Radial Distance from Flap-Tumbulator Bond Discontinuity for Cylinders Under Thermal Shrinkage and Axial Acceleration

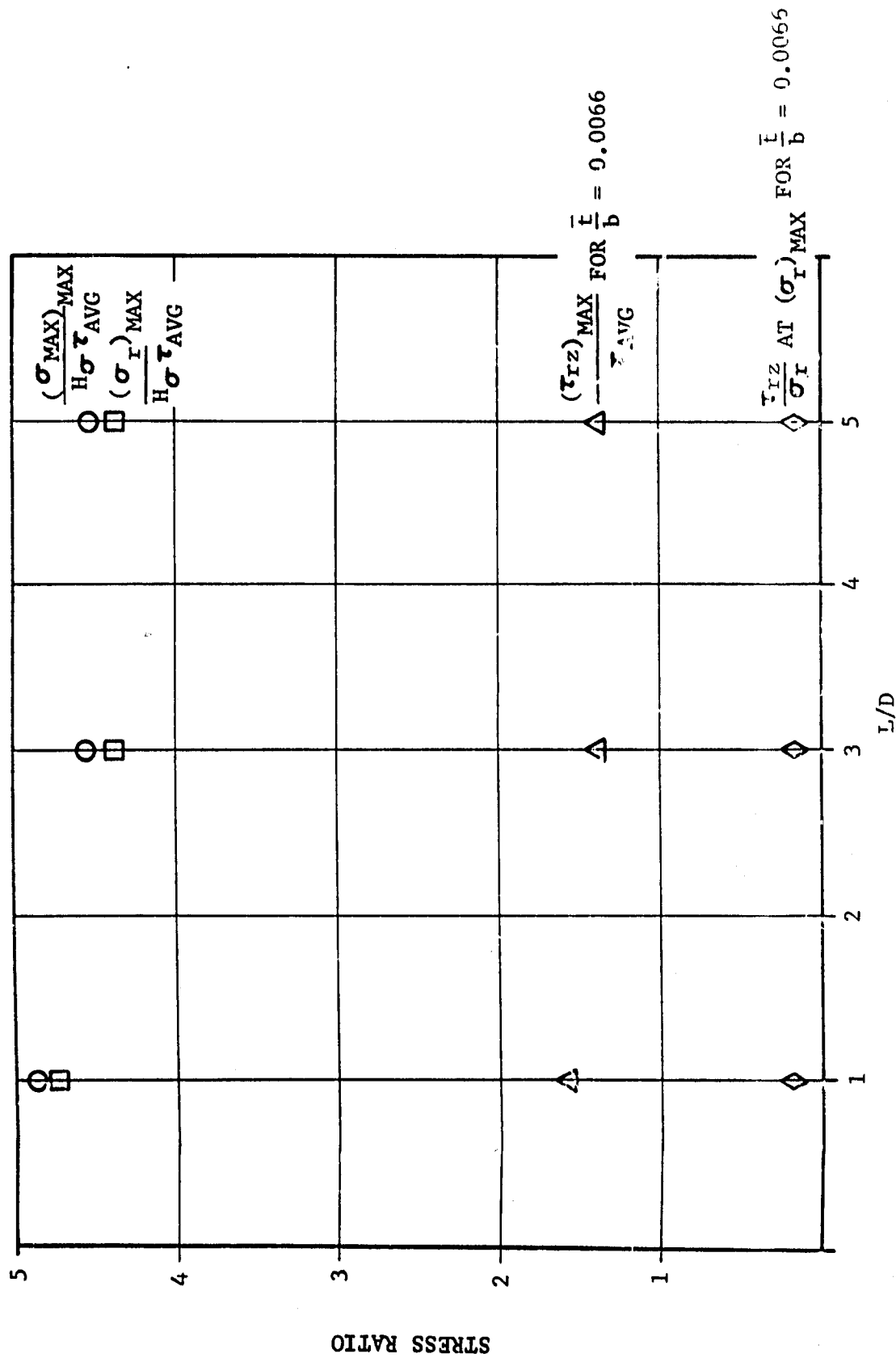


Figure 47. Normalized Case Bond Liner Stresses Adjacent to Flap Termination for Cylinder with $W/b = 0.8$ Subjected to Axial Acceleration Loading